Benchmarking Kinetic Calculations of Resistive Wall Mode Stability

J.W. Berkery,[1] Y.Q. Liu,[2] Z.R. Wang,[3] N.C. Logan,[3] S.A. Sabbagh,[1] J.-K. Park,[3] J. Manickam,[3] I.T. Chapman,[2] and R. Betti[4]

[1)] *Department of Applied Physics and Applied Mathematics, Columbia University, New York, New York 10027*

[2)] *Euratom/CCFE Fusion Association, Culham Science Centre, Abingdon, OX14 3DB, UK*

[3)] *Princeton Plasma Physics Laboratory, Princeton University, Princeton, New Jersey 08543*

[4)] *Laboratory for Laser Energetics, University of Rochester, Rochester, New York 14623*

(Dated: 14 January 2014)

Reliable, validated calculations of resistive wall mode (RWM) stability, including kinetic effects, are critical for ITER, which can not tolerate disruptions caused by those modes. Benchmarking the calculations of the `MARS-K`, `MISK`, and `PENT` codes for two Solov'ev analytical equilibria and a projected ITER equilibrium has demonstrated good agreement between the codes. The precession drift, bounce, and transit frequencies of particles, which can each cause a stabilizing resonance with the mode, are consistently evaluated between the codes, and are used in the frequency resonance energy integral. Numerical energy integral calculations are consistent between codes as well as with analytical limits. The marginally stable eigenfunctions, perturbed Lagrangians, and fluid growth rates are all consistent as well. The most important kinetic effect at low rotation is the resonance between the mode rotation and the trapped thermal particle's precession drift, and `MARS-K`, `MISK`, and `PENT` show good agreement in this term. The different ways the rational surface contribution was treated historically in the codes is identified as a source of disagreement in the bounce and transit resonance terms at higher plasma rotation. In the Solov'ev case with rational surfaces, the surfaces were integrated over (`MARS-K` treatment) and differences in the eigenfunction quantities at rational surfaces cause differences in the results. In the ITER equilibrium, singular Alfvén resonance contributions at the rational surfaces must be removed from the calculations (`MISK` treatment) to obtain reasonable results, and subsequently good agreement between the codes is found. Calculations from all of the codes support the present understanding that RWM stability can be increased by kinetic effects at low rotation through precession drift resonance and at high rotation by bounce and transit resonances, while intermediate rotation can remain susceptible to instability. The applicability of benchmarked kinetic stability calculations to experimental results is demonstrated by the prediction of `MISK` calculations (computing the contribution of rationals analytically) of near marginal growth rates for experimental marginal stability points from the National Spherical Torus Experiment (NSTX).

I. INTRODUCTION

Tokamak fusion plasmas generate energy most efficiently when the ratio of plasma stored energy to magnetic confining field energy is high. This ratio can be characterized by the quantity beta-normal: β_N. When a plasma reaches high β_N, an MHD kink-ballooning mode of instability can begin to grow. This can lead to a disruption of the plasma current and a loss of confinement on the relatively short Alfvén time scale. However, the growth rate of this mode can be slowed quite considerably by the presence of a close-fitting wall around the plasma. This forces the magnetic perturbations penetrate the wall in order to grow, and the time scale for that penetration is much longer than the Alfvén time scale. When the mode is converted to the more slowly growing mode in this way, it is called the resistive wall mode (RWM)[1].

Originally it was thought that the presence of a resistive wall could slow down the kink-ballooning mode, but that the RWM itself could not be stabilized. Experiments soon found, however, that tokamaks could be stably operated above the no-wall limit, $\beta_N^{no-wall}$[2,3]. It was then postulated theoretically that the RWM can be stabilized by a combination of plasma rotational inertia and an energy dissipation mechanism[4–6]. Simple models proved to be insufficient to explain experimental results[3,7–9], however, and recently theoretical investigation has turned to the kinetic effects on plasma stability[10–32]. There are two general approaches to calculating stability of the RWM by determining $\omega = \omega_r + i\gamma$, the complex mode frequency, where ω_r is the real mode rotation frequency, and γ is the growth rate. The first approach is to write a self-consistent set of equations for ω in terms of known quantities and then to solve the system. This approach has the advantage of self-consistency between the calculation of the mode frequency ω and the mode displacement $\boldsymbol{\xi}_\perp$.

A different approach is to change the force balance equation into an equation in terms of changes of kinetic and potential energies (δW), and then to write a dispersion relation for the complex mode frequency ω in terms of these δW terms[33,34]. This approach has been called an "energy principle"[35]- the principle being that if any small displacement, $\boldsymbol{\xi}_\perp$, from the equilibrium can be found that causes the potential energy to decrease, the kinetic energy to increase,

and the displacement to grow exponentially in time, then that equilibrium is unstable. Specifically applicable to the RWM is the so-called "low-frequency" energy principle[33,34,36–38], which requires the inclusion of the particle drift frequencies, as these can not be considered to be much lower than the mode frequency.

The approach of solving for the δW terms has the advantage of clarity in distinguishing the various stabilizing and destabilizing effects. In practice, however, one must generally assume a fixed $\boldsymbol{\xi}_\perp$, unchanged by kinetic effects. This approach is therefore called the "perturbative" approach. In this work we will concentrate on the change of potential energy that arises from the perturbed kinetic pressure of thermal particles. The RWM dispersion relation can be written[10,11,14]:

$$(\gamma + i\omega_r)\tau_w = -\frac{\delta W_\infty + \delta W_K}{\delta W_b + \delta W_K}. \tag{1}$$

Here τ_w is the current decay time in the resistive wall, δW_∞ is the sum of the plasma fluid and vacuum perturbed potential energies when the wall is placed at infinity, and δW_b is the sum of the plasma fluid and vacuum δWs when the wall is placed at a specific location b. These two contributions to the energy principle have been theoretically developed for years[39], and computer codes have been written to solve for them, such as `PEST`[40] and `DCON`[41]. The kinetic term, δW_K is given by

$$\delta W_K = -\frac{1}{2}\sum_j \int \boldsymbol{\xi}_\perp^* \cdot \left[\boldsymbol{\nabla}\cdot\tilde{\mathbb{P}}_K\right] d\mathbf{V}. \tag{2}$$

In the fluid approach the perturbed pressure is given in terms of macroscopic quantities. In the kinetic approach the components of the pressure tensor $\tilde{\mathbb{P}}_K$, $\tilde{p}_\perp$ and $\tilde{p}_\parallel$, are defined by taking moments of the perturbed distribution function $\tilde{f}$.

The goal of this work is to benchmark the calculations of kinetic effects on resistive wall mode stability between three codes, `MARS-K`, `MISK`, and `PENT`. This work builds off of, and greatly expands upon, a previous effort briefly described below in subsection I A. By group consensus it was decided to compare code calculations for two analytical equilibria, one a simple, near-circular shape with no $n = 1$ rational surfaces, and one a shaped equilibria with two $n = 1$ rational surfaces, as well as an ITER case. In each case the focus was on the calculation of rotational resonances of thermal particles, so collisions were ignored and energetic particles were not included. Though obviously important, it is beyond the scope of this work to fully compare stability calculations to present experimental results, though `MISK` calculations have been compared to both National Spherical Torus Experiment[42] (NSTX)[19–22,24,43,44] and DIII-D[26] experimental results and some comparisons between the benchmarked `MISK` calculations and NSTX results are also presented here. Benchmarked and validated calculations of RWM stability are important to confidently project the stability of future devices such as ITER, which can not tolerate disruptions.

The paper is organized as follows. First, the `MARS-K`, `MISK`, and `PENT` codes are briefly described in Sec. II. In Sec. III the equilibrium configurations that are tested are described. In Sec. IV various important frequencies of the plasma are compared, which are then used in Sec. V in the energy integral of the frequency resonance fraction. The three different eigenfunctions used are described in Sec. VI, and are then used in Sec. VII in calculating the perturbed Lagrangian. The results of the resistive wall mode stability analysis are presented, starting in Sec. VIII with the fluid δW terms, in Sec. IX with the kinetic δW term, and in Sec. X with the RWM growth rate and rotation frequency. Finally, the benchmarked calculations of the `MISK` code are briefly compared to NSTX experiments in Sec. XI.

A. Previous Benchmarking Results

In 2008, the `MARS-K` and `MISHKA+HAGIS` codes were benchmarked in Ref. [14], Sec. III-C. The equilibrium used in that exercise was the same analytical Solov'ev 1 equilibrium that will be described here later, but there were two differences in the profiles used: both density and ω_E were held constant with Ψ in Ref. [14]. The results of that study, with `MISK` results added, are included here. Figure 1 shows a comparison between `MISK` and `MARS-K` of real and imaginary δW_K for $l = 0$ trapped thermal ions and electrons.

Note that this figure appears flipped between ions and electrons with respect to the data presented in Fig. 4 of Ref. [14]. This is due to the assumption of oppositely directed ω_E than before (positive in this case as opposed to negative in the previous case, due to the x-axis definition of $n\omega_E$ with $n = -1$), which serves to flip the ion and electron contributions under the assumptions held here (see subsection V A 2).

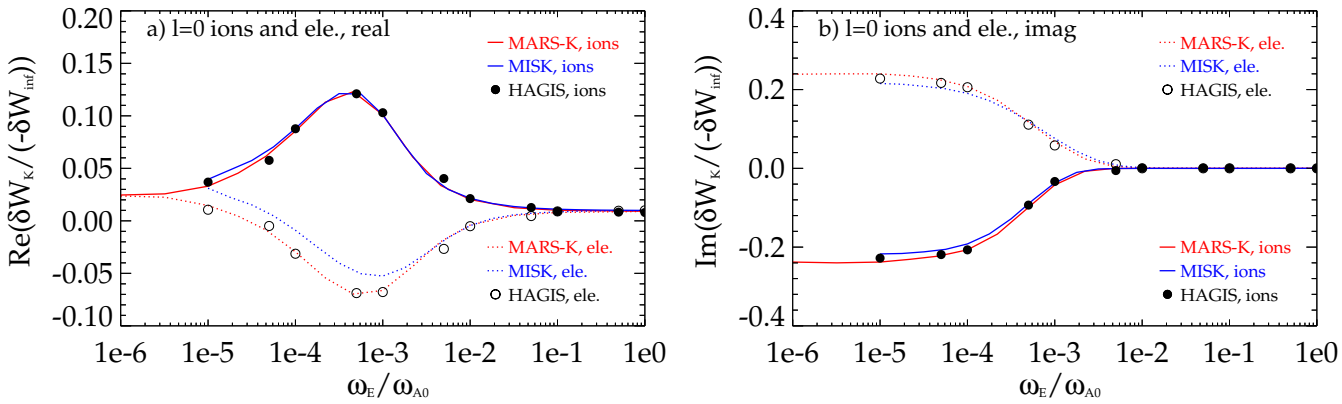

FIG. 1. a) Real and b) imaginary δW_K for $l = 0$ trapped thermal ions and electrons for the Solov'ev 1 case with flat density and ω_E profiles, as calculated by `MARS-K`, `MISK`, and `MISHKA+HAGIS`.

II. CODES

Various codes have been developed that can incorporate kinetic effects in stability calculations. In addition to the three described here, one prominent example is the combination of the `MISHKA`[45] and `HAGIS`[46] codes.

A. MARS-K

`MARS-K` (Magnetohydrodynamic Resistive Spectrum - Kinetic code) is a toroidal MHD-kinetic hybrid stability code[14,47] that solves the eigenvalue problem derived from the linearized single-fluid ideal/resistive MHD equations with toroidal flow, self-consistently including the drift kinetic effects in full toroidal geometry. The approach allows the kinetic effects associated with the thermal or energetic particles to consistently modify the mode eigenfunction, which could significantly influence the mode stability and structure in certain circumstances[31]. The code simulates a plasma surrounded by a pure vacuum region, includes a set of radially separated, toroidally complete resistive walls and a set of magnetic coils located in the vacuum region. With these features, `MARS-K` has been successfully applied to physical study and support of experiments on various subjects such as MHD instabilities (e.g. resistive wall mode and tearing mode), and plasma response to external fields (e.g. resonant filed amplification and resonant magnetic perturbation).

B. MISK

The `MISK`, or Modification to Ideal Stability by Kinetic effects, code[11] calculates the change in potential energy of the plasma due to kinetic effects, δW_K. Along with the fluid δW terms calculated using a marginally stable eigenfunction with the `PEST` code[40], the dispersion relation or energy principle including kinetic effects is used to predict the growth rate of the resistive wall mode. This approach assumes that kinetic effects do not change the eigenfunction, and that the mode growth rate and frequency are small, so their nonlinear inclusion is unimportant. Cases which are above the ideal no-wall limit, and therefore would be unstable without kinetic effects, are examined. `MISK` has been used extensively (see Refs. [12, 19–24, 26, 43, and 44]), and good agreement between the theory and experimental trends have been found.

C. PENT

The Ideal Perturbed Equilibrium Code[48] (`IPEC`) has been successfully applied to study the basic feature of plasma responses to small 3D fields in tokamaks. The code utilizes the Euler-Lagrange equation in `DCON` to solve the ideal force balance and couples solutions to the external 3D field. Recently calculations of neoclassical toroidal viscosity (NTV), based on the combined NTV formula without large-aspect-ratio approximation, have been implemented in a new Perturbed Equilibrium Nonambipolar Transport (`PENT`) code[49], which is meant to interface with `IPEC`. Because

the NTV torque is mathematically equivalent to the imaginary part of the kinetic δW[50], PENT calculates an identical energy integral to MISK and MARS-K[51], and therefore can be used in this benchmarking study.

III. EQUILIBRIA

Three equilibria were agreed upon for this benchmarking exercise: an analytical equilibrium with nearly circular surfaces and no rational surfaces, an analytical equilibrium with shaped surfaces and two rationals, and finally a projected ITER equilibrium.

A. Solov'ev Equilibrium

The Solov'ev equilibrium[52,53] is an analytical equilibrium solution to the Grad-Shafranov equation for the polodial current function $F = RB_t$ (with R the major radius and B_t the toroidal magnetic field), and the pressure profile $P(\psi)$, where ψ is the magnetic flux coordinate. In MARS-K, the Solov'ev equilibrium is written[14]:

$$F(\psi) = 1. \tag{3}$$

$$\frac{\mu_0}{B_0^2} P(\psi) = -\frac{1+\kappa^2}{\kappa R_0^3 q_0}\psi. \tag{4}$$

$$\psi = \frac{\kappa}{2R_0^3 q_0}\left[\frac{R^2 Z^2}{\kappa^2} + \frac{1}{4}\left(R^2 - R_0^2\right)^2 - \epsilon_a^2 R_0^4\right]. \tag{5}$$

This ψ ranges from a negative value at the axis ($-\psi_0$) to zero at the edge. A normalized flux can be written $\psi_n = \psi/\psi_0 + 1$, which goes from 0 on axis to 1 at the edge. In addition to B_0, the magnetic field on axis, and R_0, the major radius of the plasma axis, three quantities must be specified: the elongation κ, the safety factor on axis q_0, and the inverse aspect ratio $\epsilon_a = a/R_0$, where a is the plasma minor radius. The plasma boundary is specified in (R, Z) coordinates by:

$$R_b = R_0\left(1 + 2\epsilon_a \cos\theta\right)^{\frac{1}{2}}, \tag{6}$$

$$Z_b = \frac{R_0 \epsilon_a \kappa \sin\theta}{\left(1 + 2\epsilon_a \cos\theta\right)^{\frac{1}{2}}}. \tag{7}$$

MISK uses the PEST code[40] to provide the eigenfunction and fluid δW terms. The Solov'ev equilibrium can be explicitly input into PEST[a], and it is written:

$$F(\Psi) = 1. \tag{8}$$

$$\frac{\mu_0}{B_0^2} P(\Psi) = p_0 - \frac{\Psi}{2\pi}\sqrt{\frac{2c_1 p_0(1+c_3^2)}{\Psi_{lim}}}. \tag{9}$$

$$\Psi = c_1\left[Z^2\left(R^2 - c_2\right) + \frac{c_3^2}{4}\left(R^2 - R_0^2\right)^2\right]. \tag{10}$$

[a] To use the analytical Solov'ev equilibrium in PEST, one sets `&glotcl lanal=.true.`, in both `mapin` and `modin`. Then one specifies the above quantities in `mapin` where c_1, c_2, and c_3 are listed under `&kerdat` as `c1`, `c2`, and `c3`, p_0 is listed under `&prof` as `p0`, Ψ_{lim} is listed under `&magax` as `psilim`, and R_0 is listed under `&size` as `r`. Also, α_p must be set in `modin` under `&cprofl` as `alphap`.

Here the PEST Ψ goes from 0 at the axis to a positive value, Ψ_{lim}, at the edge, and is related to the MARS-K ψ by:

$$\psi = (\Psi - \Psi_{lim})/2\pi. \tag{11}$$

The specifications are:

$$c_1 = \frac{1}{2\kappa R_0^3 q_0} 2\pi \tag{12}$$

$$c_2 = 0 \tag{13}$$

$$c_3 = \kappa \tag{14}$$

$$\Psi_{lim} = \frac{\epsilon_a^2 R_0 \kappa}{2q_0} 2\pi \tag{15}$$

$$p_0 = \frac{1+\kappa^2}{2} \frac{\epsilon_a^2}{R_0^2 q_0^2} \tag{16}$$

$$\alpha_p = \sqrt{\frac{2c_1 p_0 (1+c_3^2)}{\Psi_{\rm lim}}} = \frac{1+\kappa^2}{\kappa q_0 R_0^3}. \tag{17}$$

Note that for the Solov'ev cases, the q profile can be analytically determined from[54]:

$$q = q_0 \frac{2}{\pi} \frac{\sqrt{1+2\epsilon_r}}{1-4\epsilon_r^2} E(k), \tag{18}$$

where E is the complete elliptic integral of the second kind, $k \equiv \sqrt{4\epsilon_r/(1+2\epsilon_r)}$, and $\varepsilon_r = r/R_0$ (with $r = R - R_0$).

1. Solov'ev case 1

The equilibrium designated "Solov'ev 1" was used in Ref. [14], and is near-circular (Fig. 2a), with no rational surfaces (Fig. 3a). It is specified by the parameters $\kappa = 1$, $q_0 = 1.2$, and $\epsilon_a = 0.2$, and has a $q_{\rm edge} = 1.41371$. For the Solov'ev 1 case, the bounce harmonics from $l = -15$ to $+18$ are used.

2. Solov'ev case 3

The equilibrium designated "Solov'ev 3" was also used in Ref. [14]. This equilibrium is shaped (Fig. 2b), and contains the $q = 2$ and 3 rational surfaces within the plasma (Fig. 3b). It is specified by the parameters $\kappa = 1.6$, $q_0 = 1.9$, and $\epsilon_a = 0.33$, and has a $q_{\rm edge} = 3.263$. For the Solov'ev 3 case, the bounce harmonics from $l = -24$ to $+38$ are used.

Note that due to geometrical convention in the MARS-K code, both Solov'ev eigenfunctions will be considered to have $n = -1$ toroidal mode numbers.

B. ITER

The ITER equilibrium used is the same as is used in the International Tokamak Physics Activity (ITPA) working group 7 (WG-7), using the current design of the ITER target for 9 MA operation[55], with $\beta_N = 2.9$. It has $R_0 = 6.2$ m, $B_0 = 5.3$ T, the shape shown in Fig. 4 and the q profile shown in Fig. 5. For the ITER case, MARS-K used bounce harmonics from $l = -48$ to $l = +78$, while MISK used $l = -4$ to $+4$. Larger bounce harmonics contribute diminishingly to the kinetic effects and it was found that $|l| > 4$ was negligible in the MISK calculation. Also, the MISK and MARS-K calculations both avoided a region of $\Delta q = \pm 0.1$ around each rational surface to eliminate unreasonably high calculated stabilizing effects from the rational surfaces, as will be discussed in section IX C.

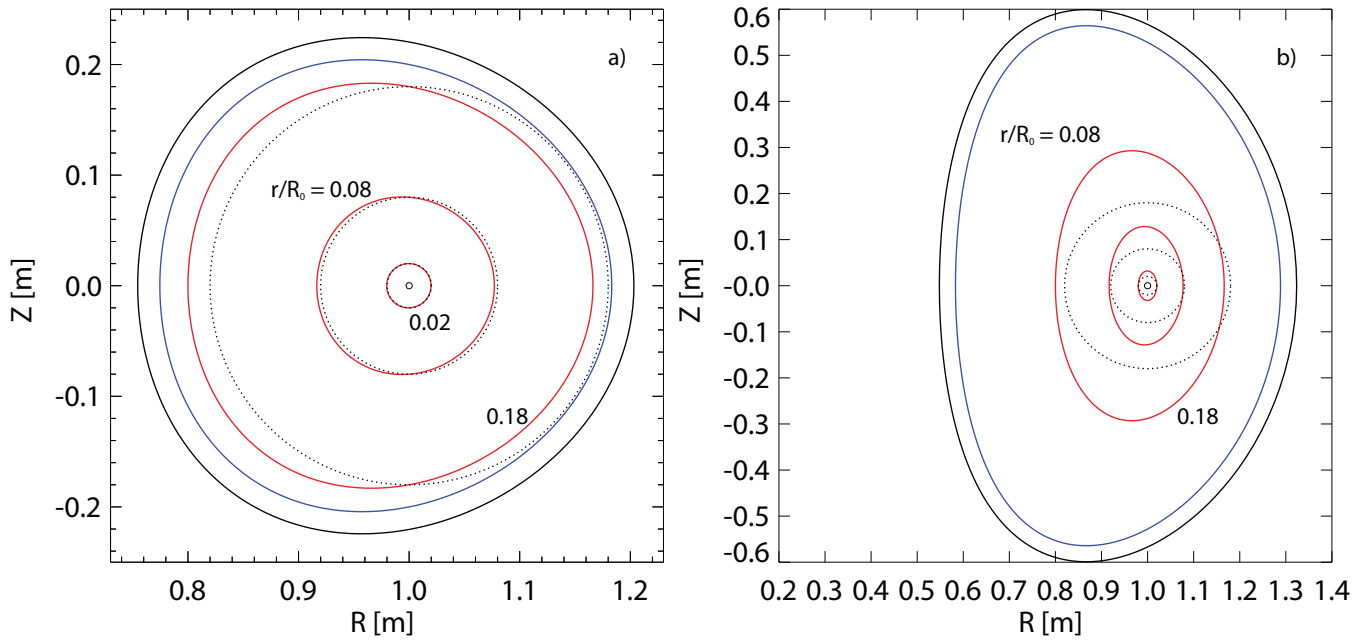

FIG. 2. a) The Solov'ev 1 equilibrium and b) the Solov'ev 3 equilibrium, showing flux surfaces at the edge (blue) and $r/R_0 = 0.02$, 0.08, and 0.18 (red). These last three are compared to their equivalent circles (dashed). Finally, conformal walls having $r_w/a = 1.15$ for Solov'ev 1 and $r_w/a = 1.10$ for Solov'ev 3 are shown in black (see section VIII).

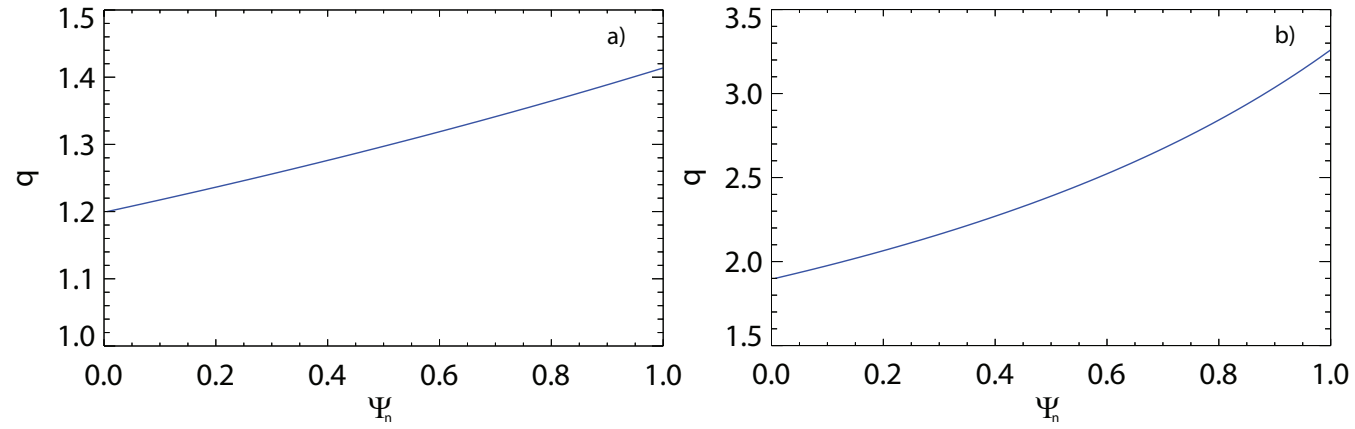

FIG. 3. a) The Solov'ev 1 equilibrium and b) Solov'ev 3 equilibrium q profiles.

IV. FREQUENCY COMPARISONS

A. Density, Temperature, Pressure, and Rotation Frequency Profiles

We will assume for the Solov'ev cases that there are no energetic particles, only thermal ions and electrons, and that the ion and electron densities and temperatures are equal, $n_e = n_i$ and $T_e = T_i$. Also, for the purposes of determining P from Eqs. 4 or 9, we now set $R_0 = 1$m and $B_0 = 1$T. Then the pressure has the form $P = P_0(1 - \psi_n)$, with $P_0 = 2.210 \times 10^4$ Pa for Solov'ev 1, and $P_0 = 4.273 \times 10^4$ Pa for Solov'ev 3.

Finally we must specify the density profile $n(\Psi)$. For the Solov'ev cases, we use $n = n_0(1-0.7\Psi_n)$. Then the density on axis, n_0, is determined by specifying $(\omega_{ci}/\omega_A)_0$, where the Alfvén frequency on axis $\omega_{A0} = B_0/(R_0\sqrt{\mu_0 m_i n_{i0}})$ and the ion cyclotron frequency on axis $\omega_{ci0} = eB_0/m_i = 47.906 \times 10^6$ rad/s. For the comparisons here, we will use $(\omega_{ci}/\omega_A)_0 = 121$, to be consistent with Ref. [14], even though this results in the values of $\omega_{A0} = 395.914$ krad/s and the unrealistically high density $n_0 = 1.518 \times 10^{21}$ m^{-3}.

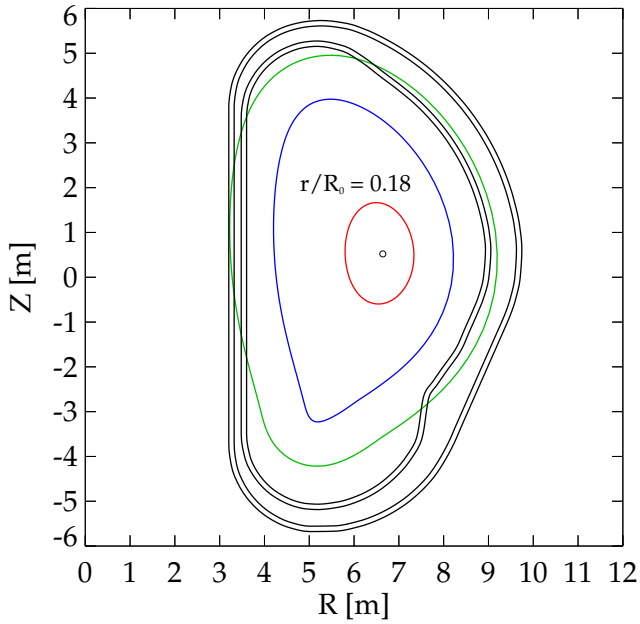

FIG. 4. The ITER equilibrium, showing a flux surface at the edge (blue) and $r/R_0 = 0.18$ (red). Also shown are the ITER double wall (black), and a conformal wall with $r_w/a = 1.5$ (green).

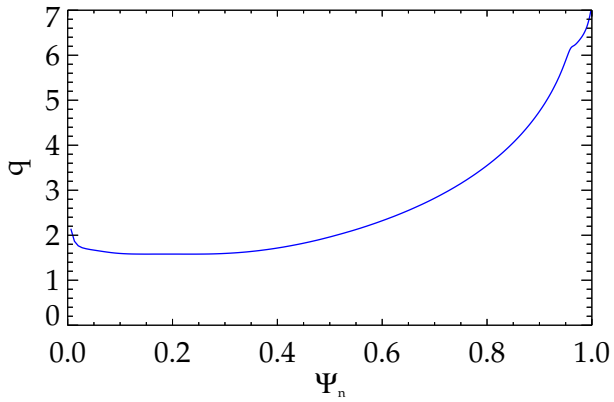

FIG. 5. The ITER equilibrium q profile.

The temperature profile is then determined from $T = P/(2n)$. For the Solov'ev cases this means $T = (P_0/2n_0)(1 - \Psi_n)/(1 - 0.7\Psi_n)$.

For the Solov'ev cases we will use the $E \times B$ frequency profile $\omega_E = \omega_{E0}\,(1 - \Psi_n)$, and a range of constant values of ω_{E0}. For the moment, we will assume $\omega_E/\omega_{A0} = 1 \times 10^{-2}$ or $\omega_{E0} = 3.959$ krad/s as a nominal value. Throughout this document results are presented as functions of ω_{E0}/ω_{A0} and also as single values. When not explicitly specified, the value of ω_{E0}/ω_{A0} should be assumed to be 1×10^{-2}. The toroidal rotation frequency, ω_ϕ can then be found by a radial force balance so that $\omega_\phi = \omega_E + \omega^i_{*N} + \omega^i_{*T}$, where ω^i_{*N} and ω^i_{*T} are defined in the next subsection. Poloidal rotation is assumed to be negligible.

For the ITER case instead of using analytically prescribed functions for the pressure, density, temperature, and rotation, we will use profiles determined for the WG-7 ITER equilibrium, which represents an ITER steady-state scenario. Additionally, the ITER case will have three separate species, each with their own pressure: deuterium ions, electrons, and alpha particles (tritium is not considered). The following are given, as profiles of Ψ: $n_\alpha/(n_e + n_i)$, n_e, T_e, T_i, $P_\alpha/(P_e + P_i)$, and ω_ϕ. The ion density is taken to be equal to the electron density, ie. quasineutrality is not enforced. The ion and electron pressures are determined from $P_e = n_e T_e$, and $P_i = n_i T_i$, which then determines P_α

as well, although alpha particles are not actually used in this study. The nominal value of ω_{E0}/ω_{A0} calculated from these parameters is 1.62×10^{-2} for the ITER case.

Figure 6 shows the profiles of density, pressure, and temperature, normalized to the axis values, which are given in Table I. Figure 6 also shows profiles of rotation and the diamagnetic frequencies, ω_{*N} and ω_{*T}. These are also normalized to the axis values, found in Table II, along with the consistent ω_{E0} values.

B. Diamagnetic Frequencies

The density and temperature gradient components of the diamagnetic frequency are defined in [rad/s] as:

$$\omega^j_{*N} = -\frac{T_j}{Z_j e n_j}\frac{dn_j}{d\Psi}, \tag{19}$$

$$\omega^j_{*T} = -\frac{1}{Z_j e}\frac{dT_j}{d\Psi}. \tag{20}$$

For the Solov'ev equilibria these can be written analytically as:

$$\omega^i_{*N} = -\omega^e_{*N} = \frac{0.7T_0/e}{\Psi_a}\left(\frac{1-\Psi_n}{(1-0.7\Psi_n)^2}\right), \tag{21}$$

$$\omega^i_{*T} = -\omega^e_{*T} = \frac{0.3T_0/e}{\Psi_a}\left(\frac{1}{(1-0.7\Psi_n)^2}\right), \tag{22}$$

where $\Psi_a = -\psi_0 = \Psi_{\rm lim}/2\pi$ from Eq. 15.

C. Collision Frequency

Although in general collisionality can impact kinetic stability calculations, and there are various ways of expressing collisionality[22], for the comparisons here, all collision frequencies are taken to be zero. This decision was taken to avoid the complication of the effect of collisionality and to allow focus on the computation and comparison of other physics aspects in the codes.

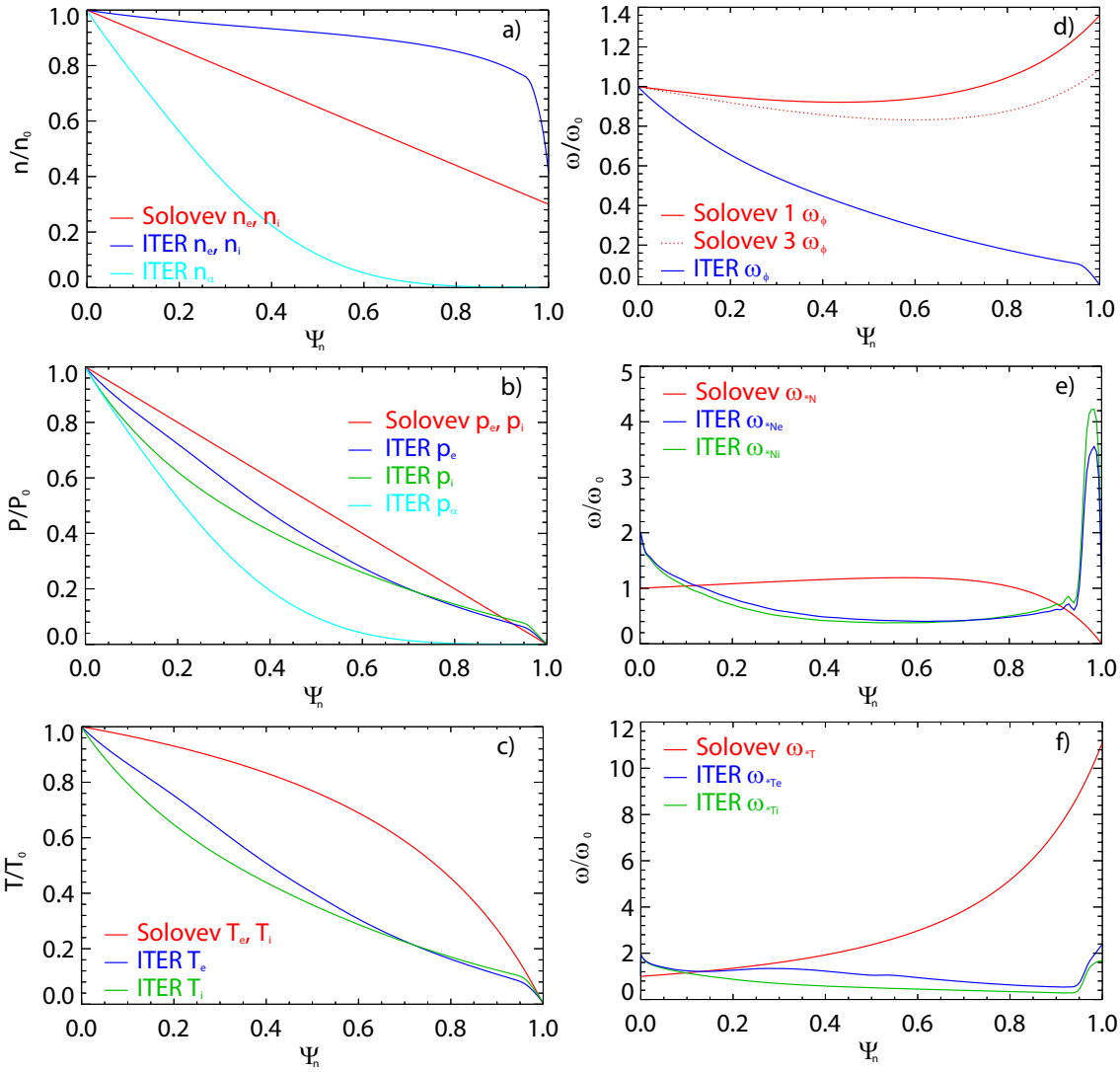

FIG. 6. Normalized profiles of a) density, b) pressure, c) temperature, d) rotation, e) ω_{*N}, and f) ω_{*T}.

	$n_{i0}[10^{19}\mathrm{m}^{-3}]$	$n_{e0}[10^{19}\mathrm{m}^{-3}]$	$n_{\alpha 0}[10^{19}\mathrm{m}^{-3}]$	p_{i0} [kPa]	p_{e0} [kPa]	$p_{\alpha 0}$ [kPa]	T_{i0} [keV]	T_{e0} [keV]
Solov'ev 1	151.795		0	11.052		0	0.045	
Solov'ev 3				21.365			0.088	
ITER	7.220		0.167	362.306	396.200	156.739	31.320	34.250

TABLE I. Density, pressure, and temperature values on axis for each of the cases.

	$\omega_{\phi 0}$	ω_{E0}	ω_{*Ne0}	ω_{*Ni0}	ω_{*Te0}	ω_{*Ti0}
Solov'ev 1	6.675	3.959*	1.902		0.820	
Solov'ev 3	5.858		1.339		0.578	
ITER	37.34*	25.13	-0.968	0.880	6.032	11.34

TABLE II. Rotation frequency, ω_E, ω_{*N}, and ω_{*T} values on axis for each of the cases, all in krad/s. *nominal values.

D. Bounce Frequency

Figure 7a shows the normalized, dimensionless ion bounce frequencies calculated by `MARS-K`, `MISK`, and `PENT` compared to the large aspect ratio approximation, using the Solov'ev 1 equilibrium at the $\epsilon_r = 0.08$, $\psi_n = 0.160$ surface vs. Λ. Figure 8a shows the normalized ion bounce frequencies calculated by `MARS-K`, `MISK`, and `PENT` compared to the large aspect ratio approximation, using the Solov'ev 3 equilibrium at the $\epsilon_r = 0.33$, $\psi_n = 1$ surface (the plasma boundary) vs. Λ.

Figure 9a shows the normalized ion bounce frequencies calculated by `MARS-K`, `MISK`, and `PENT`, using the ITER equilibrium at the $\epsilon_r = 0.322$, $\psi_n = 0.982$ surface (very close to the plasma boundary) vs. Λ.

Figure 10a shows the normalized ion bounce frequencies calculated by `MARS-K`, `MISK`, and `PENT` at maximum Λ compared to the deeply trapped particle limit, using the Solov'ev 1 equilibrium and the Solov'ev 3 equilibrium vs. ϵ_r.

Below we will describe the large aspect ratio and deeply trapped limit formulae for the bounce frequency to which the calculations have been compared. However, the bounce frequency used in each code is calculated without these approximations.

1. Large Aspect Ratio Formula

In the large aspect ratio limit, the particle bounce frequency can be written[13,56]:

$$\frac{\omega_b}{\sqrt{2\varepsilon/m_i}} = \frac{\sqrt{2\epsilon_r\Lambda}}{4qR_0}\frac{\pi}{K(k)} \quad \text{(trapped)}, \tag{23}$$

$$\frac{\omega_b}{\sqrt{2\varepsilon/m_i}} = \frac{\sqrt{1-\Lambda+\epsilon_r\Lambda}}{2qR_0}\frac{\pi}{K(1/k)} \quad \text{(circulating)}. \tag{24}$$

where Λ is a pitch angle variable defined by $\Lambda = \mu B_0/\varepsilon$ with $\mu = mv_\perp^2/2B$ the magnetic moment and $\varepsilon = mv^2/2$ the kinetic energy of the particle (m and v are the mass and velocity of the particle), K is the complete elliptic integral of the first kind, and

$$k = \left[\frac{1-\Lambda+\epsilon_r\Lambda}{2\epsilon_r\Lambda}\right]^{\frac{1}{2}}. \tag{25}$$

2. Deeply Trapped Particle Formula

In the limit of deeply trapped particles, one can show that for the Solov'ev equilibrium the bounce frequency can be written[54]:

$$\frac{\omega_b}{\sqrt{2\varepsilon/m_i}} = \frac{1}{q_0}\left(\frac{F^2}{1+2\epsilon_r} + \frac{\kappa^2\epsilon_r^2}{q_0^2}\right)^{-1}\left[\frac{F^2\epsilon_r}{2\left(1+2\epsilon_r\right)} + \frac{\kappa^2\epsilon_r^3}{q_0^2} + \frac{\left(1-\kappa^2\right)\epsilon_r^2}{2q_0^2}\left(1+2\epsilon_r\right)\right]^{\frac{1}{2}} \tag{26}$$

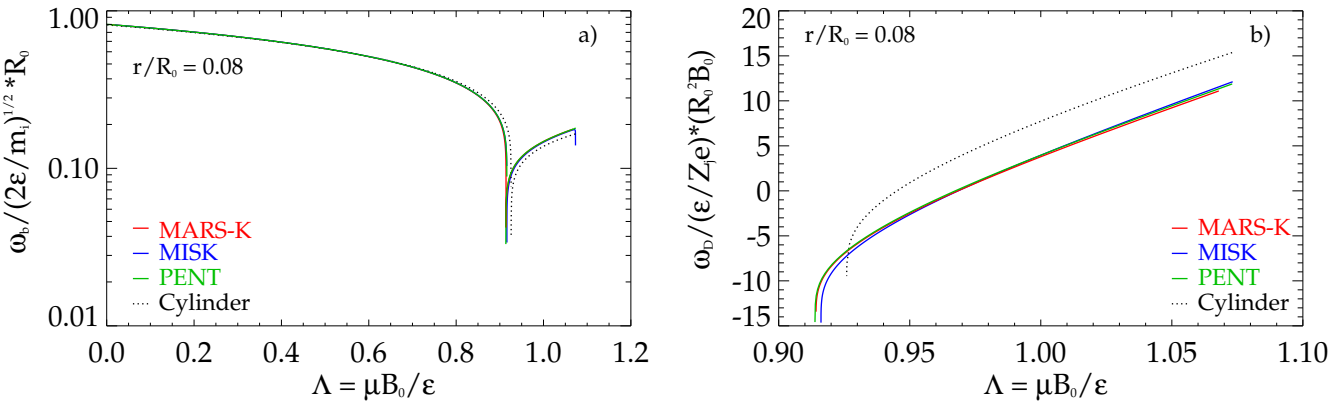

FIG. 7. a) Ion bounce frequency and b) ion precession drift frequency calculated by `MISK`, `MARS-K`, and `PENT` compared to the large aspect ratio approximation for the $\epsilon_r = 0.08$ surface of the Solov'ev 1 case, vs. Λ. The left branch of a) is for circulating ions and the right branch is for trapped ions. Plot b) can be directly compared to the same one produced by `MARS-K` in Ref. [14], Fig. 1(b).

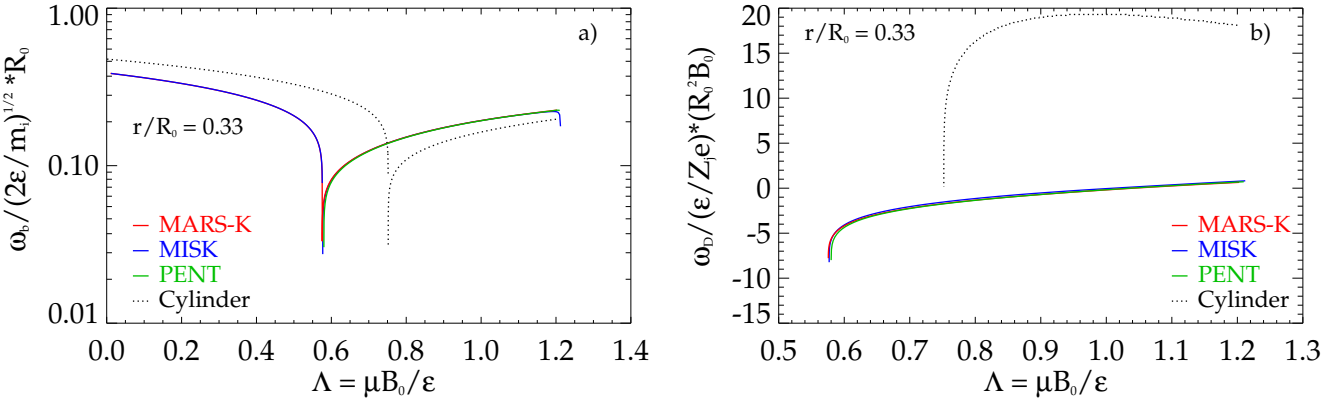

FIG. 8. a) Ion bounce frequency and b) ion precession drift frequency calculated by `MISK`, `MARS-K`, and `PENT` compared to the large aspect ratio approximation at the outer surface of the Solov'ev 3 case, vs. Λ. The left branch of a) is for circulating ions and the right branch is for trapped ions.

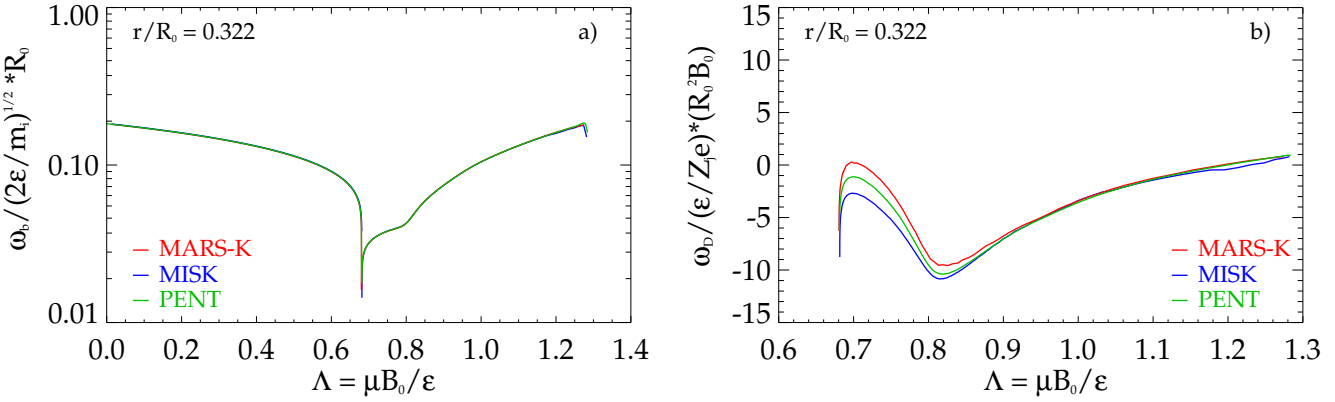

FIG. 9. a) Ion bounce frequency and b) ion precession drift frequency calculated by `MISK`, `MARS-K`, and `PENT` at the $\epsilon_r = 0.322$ surface (very close to the outer surface) of the ITER case, vs. Λ. The left branch of a) is for circulating ions and the right branch is for trapped ions.

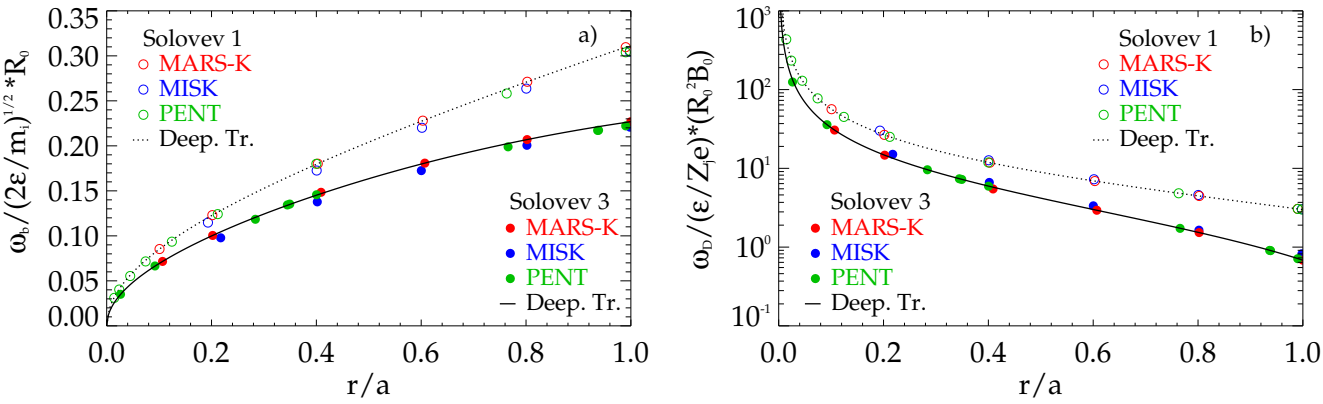

FIG. 10. a) Ion bounce frequency and b) ion precession drift frequency calculated by MISK, MARS-K, and PENT at maximum Λ compared to the deeply trapped particle limit for the Solov'ev 1 and 3 cases, vs. ϵ_r.

E. Magnetic Precession Drift Frequency

Figure 7b shows the normalized ion precession drift frequencies calculated by MARS-K, MISK, and PENT compared to the large aspect ratio approximation, using the Solov'ev 1 equilibrium at the $\epsilon_r = 0.08$, $\psi_n = 0.160$ surface, vs. Λ. A more sophisticated analytic approach to calculate the precession drift frequency for arbitrarily shaped toroidal plasmas, by doing a higher order expansion of the toroidal equilibrium in terms of toroidicity, elongation, triangularity, etc... was also compared to this case and was quite close to the MARS-K result[57].

Figure 8b shows the normalized ion precession drift frequencies calculated by MARS-K, MISK, and PENT compared to the large aspect ratio approximation, using the Solov'ev 3 equilibrium at the $\epsilon_r = 0.33$, $\psi_n = 1$ surface (the plasma boundary), vs. Λ.

Figure 9b shows the normalized ion precession drift frequencies calculated by MARS-K, MISK, and PENT, using the ITER equilibrium at the $\epsilon_r = 0.322$, $\psi_n = 0.982$ surface (very close to the plasma boundary) vs. Λ.

Figure 10b shows the normalized ion precession drift frequencies calculated by MARS-K, MISK, and PENT at maximum Λ compared to the deeply trapped particle limit, using the Solov'ev 1 equilibrium and the Solov'ev 3 equilibrium vs. ϵ_r.

Below we first will describe the large aspect ratio and deeply trapped limit formulae for the precession drift frequency to which the calculations have been compared. Then the general formula used in the codes is described.

1. Large Aspect Ratio Formula

The large aspect ratio precession drift frequency for trapped particles[13,14]:

$$\frac{\omega_D}{\varepsilon/(Z_j e)} = \frac{2q\Lambda}{R_0^2 \epsilon_r B_0}\left[(2s+1)\frac{E(k)}{K(k)} + 2s\left(k^2-1\right) - \frac{1}{2}\right], \tag{27}$$

where $s = (r/q)(dq/dr)$ is the magnetic shear and E is the complete elliptic integral of the second kind.

We can also write this expression in a way that separates it into a "main" term and a "q shear" term:

$$\frac{\omega_D}{\varepsilon/(Z_j e)} = \frac{2q\Lambda}{R_0^2 \epsilon_r B_0}\left[\frac{E(k)}{K(k)} - \frac{1}{2}\right] + \frac{2q\Lambda}{R_0^2 \epsilon_r B_0}\left[2s\left(\frac{E(k)}{K(k)} + k^2 - 1\right)\right]. \tag{28}$$

2. Deeply Trapped Particle Formula

In the limit of deeply trapped particles, one can show that for the Solov'ev equilibrium the precession drift frequency can be written[54]:

$$\frac{\omega_D}{\varepsilon/(Z_j e)} = \frac{q_0}{R_0 \kappa \epsilon_r} \left(\frac{F^2}{1+2\epsilon_r} + \frac{\kappa^2 \epsilon_r^2}{q_0^2} \right)^{-1} \left[\frac{F^2}{(1+2\epsilon_r)^2} - \frac{\kappa^2 \epsilon_r}{q_0^2} \right] \tag{29}$$

3. General Formula

The general formula for the bounce-averaged magnetic precession drift frequency comes from Ref. [58], and is given by:

$$\omega_D = \frac{1}{Z_j e} \frac{\partial J/\partial \Psi}{\partial J/\partial \varepsilon}, \tag{30}$$

where

$$J = \int m_j v_\parallel d\boldsymbol{\ell}, \tag{31}$$

is the equilibrium longitudinal invariant of the particle parallel motion ($\boldsymbol{\ell}$ is the particle trajectory). This equation for ω_D is broken into two parts. Using a definition of the bounce time, $\tau = \partial J/\partial \varepsilon$,[58] we have:

$$\omega_D = \frac{\varepsilon}{Z_j e} \frac{1}{\tau} \frac{2}{v^2} \frac{\partial}{\partial \Psi} \left(\int v_\parallel d\boldsymbol{\ell} \right) \tag{32}$$

$$= \frac{\varepsilon}{Z_j e} \frac{1}{\tau} \frac{2}{v^2} \left[\int \frac{\partial v_\parallel}{\partial \Psi} d\boldsymbol{\ell} + \int v_\parallel \frac{\partial d\boldsymbol{\ell}}{\partial \Psi} \right] \tag{33}$$

$$= \frac{\varepsilon}{Z_j e} \frac{1}{\tau} \int \frac{d\boldsymbol{\ell}}{v_\parallel} \left[\frac{1}{v^2} \frac{\partial v_\parallel^2}{\partial \Psi} \right] + \frac{\varepsilon}{Z_j e} \frac{1}{\tau} \int \frac{2 v_\parallel}{v^2} \frac{\partial}{\partial \Psi} \left(\frac{d\boldsymbol{\ell}}{d\theta} \right) d\theta \tag{34}$$

Let us now define[58]

$$g = \frac{B_\theta^2}{B} \frac{d\boldsymbol{\ell}}{d\theta}. \tag{35}$$

Then

$$\omega_D = \frac{\varepsilon}{Z_j e} \frac{1}{\tau} \int \frac{d\boldsymbol{\ell}}{v_\parallel} \left[\frac{1}{\varepsilon} \frac{\partial}{\partial \Psi} (\varepsilon - \mu B) \right] + \frac{\varepsilon}{Z_j e} \frac{1}{\tau} \int \frac{2 v_\parallel}{v^2} \frac{\partial}{\partial \Psi} \left(\frac{gB}{B_\theta^2} \right) d\theta \tag{36}$$

$$= -\frac{\varepsilon}{Z_j e} \frac{1}{\tau} \int \frac{d\boldsymbol{\ell}}{v_\parallel} \left[\frac{\mu}{\varepsilon} \frac{\partial B}{\partial \Psi} \right] + \frac{\varepsilon}{Z_j e} \frac{1}{\tau} \int \frac{2 v_\parallel}{v^2} \frac{gB}{B_\theta^2} \left(\frac{1}{g} \frac{\partial g}{\partial \Psi} + \frac{B_\theta^2}{B} \frac{\partial}{\partial \Psi} \left(\frac{B}{B_\theta^2} \right) \right) d\theta \tag{37}$$

$$= -\frac{\varepsilon}{Z_j e} \frac{1}{\tau} \int \frac{d\boldsymbol{\ell}}{v_\parallel} \left[\frac{\Lambda}{B_0} \frac{\partial B}{\partial \Psi} \right] + \frac{\varepsilon}{Z_j e} \frac{1}{\tau} \int d\boldsymbol{\ell} \frac{2 v_\parallel}{v^2} \left[\frac{B_\theta^2}{B} \frac{\partial}{\partial \Psi} \left(\frac{B}{B_\theta^2} \right) - \frac{1}{B_\theta^2} \left(\mu_0 \frac{\partial p}{\partial \Psi} + \frac{F}{R^2} \frac{\partial F}{\partial \Psi} \right) \right], \tag{38}$$

where we have used[58]

$$\frac{1}{g} \frac{\partial g}{\partial \Psi} = -\frac{1}{B_\theta^2} \left(\mu_0 \frac{\partial p}{\partial \Psi} + \frac{F}{R^2} \frac{\partial F}{\partial \Psi} \right). \tag{39}$$

Equation 38 is the form for ω_D used in `MARS-K`. The first term is called D_μ and the second term is D_B. An equivalent expression is used in `MISK`.

Note that at the turning points $v_\parallel \to 0$ causes a singularity in Eq. 38, but this singularity is integrable.

V. ENERGY INTEGRAL OF THE FREQUENCY RESONANCE FRACTION

A major part of the kinetic calculation is the energy integration of the frequency resonance fraction:

$$I_\varepsilon(\Psi,\Lambda,l)=\frac{1}{2}\sum_{\sigma=\pm1}\int_0^\infty \frac{n\left(\omega_{*N}+\left(\hat{\varepsilon}-\frac{3}{2}\right)\omega_{*T}\right)+n\omega_E-\omega_r-i\gamma}{n\omega_D+\sigma\left(l+\alpha nq\right)\omega_b-i\nu_{\text{eff}}+n\omega_E-\omega_r-i\gamma}\hat{\varepsilon}^{\frac{5}{2}}e^{-\hat{\varepsilon}}d\hat{\varepsilon}. \tag{40}$$

where $\hat{\varepsilon}=\varepsilon/T$, and $\alpha=0$ for trapped particles or $\alpha=1$ for circulating particles, σ is the sign of $v_\parallel$, and the factor of $\frac{1}{2}$ is added for convenience (for example, so that for trapped particles, the factor of 2 that results from the summation over σ is canceled). Here l is the bounce harmonic and n is the toroidal mode number (not the density), and it will be taken as $n=-1$ for the comparisons presented here, to be consistent with the MARS-K geometrical convention. The energy integral can be evaluated based only upon the frequencies already described, for both ions and electrons. Nominally, $\nu_{\text{eff}}=0$ as specified in subsection IV C, and we will take $\omega_r=0$ and $\gamma=0$. Note that when collisionality is zero, having a small imaginary component (via γ) in the denominator is beneficial to avoid singularities in the integration[24]. Since we are taking $\nu_{\text{eff}}=0$ and $\gamma=0$, there are poles on the real energy axis, which must be accounted for (see next subsection).

If we choose a particular Ψ surface, then ω_{*N}, ω_{*T}, and ω_E are constants defined by Figs. 6d-f and Table II. The precession drift and bounce frequencies are functions of both Λ and $\hat{\varepsilon}$ still, as indicated in Figs. 7, 8, and 9.

A. Analytical Solutions

One major historical difference between MISK and MARS-K is that MISK performed the energy integration numerically, whereas MARS-K performed it analytically[13]. Analytical solutions are possible only under certain constraints. For example, ν_{eff} must not have energy dependence and when $l\neq0$ one must assume $\omega_D=0$ ($\omega_D\ll\omega_b$). Since this is the approach taken in MARS-K and in MISK's analytical mode, we have used this assumption in PENT and in MISK's numerical mode for the purposes of this benchmarking. MARS-K, however, has recently implemented numerical integration, and can now treat energy-dependent collisionality. Therefore both MISK and MARS-K now have the capability to perform the energy integral either analytically or numerically. Although they were not used in that way in the present comparisons, in general each code can have energy-dependent collisionality and both precession and bounce frequencies simultaneously.

1. CGL Limit

In the Chew-Goldberger-Low (CGL) limit, $|\omega_E-\omega|\to\infty$ and therefore

$$I_\varepsilon(\Psi,\Lambda,l)\to I_\varepsilon^{CGL}=\int_0^\infty\hat{\varepsilon}^{\frac{5}{2}}e^{-\hat{\varepsilon}}d\hat{\varepsilon}=\frac{15\sqrt{\pi}}{8}. \tag{41}$$

In this limit δW_K is purely real, and independent of the mode-particle resonances. This allows a good check on the perturbed Lagrangian part of the problem.

2. ν_{eff} = constant (no energy dependence), and $l=0$ for trapped particles

This is the case for trapped particles without energy-dependent collisions, with only the precession drift and no bounce frequency,

$$I_\varepsilon=\int_0^\infty\frac{\Omega_*^a+\Omega_n+\hat{\varepsilon}\Omega_*^b}{\hat{\varepsilon}+\Omega_n}\hat{\varepsilon}^{\frac{5}{2}}e^{-\hat{\varepsilon}}d\hat{\varepsilon}, \tag{42}$$

where $\Omega_n=(n\omega_E-\omega-i\nu_{\text{eff}})/(n\overline{\omega_D})$, $\Omega_*^a=(n\omega_{*N}-\frac{3}{2}n\omega_{*T}+i\nu_{\text{eff}})/(n\overline{\omega_D})$, $\Omega_*^b=\omega_{*T}/\overline{\omega_D}$, and $\omega_D=\overline{\omega_D}\hat{\varepsilon}$ (ie. $\overline{\omega_D}$ is the non-energy dependent portion of ω_D). Note that when $\omega=0$ and $\nu_{\text{eff}}=0$, each Ω is independent of n in this case and so I_ε for $l=0$ trapped particles will not change whether $n=1$ or -1. The solution to the above expression is given in Ref. [13], Eq. 30:

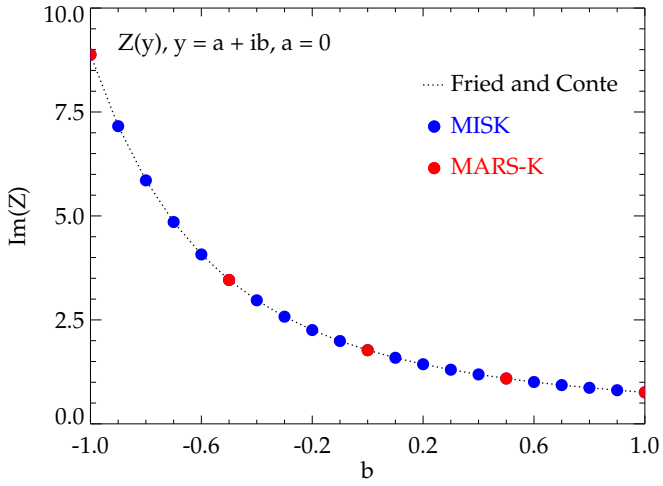

FIG. 11. A comparison of the calculation from `MARS-K` and `MISK` of the imaginary part of the plasma dispersion function, $Z(y)$, for purely imaginary y, to the curves given in Ref. [59].

$$I_\varepsilon = \frac{15\sqrt{\pi}}{8}\Omega_*^b + 2\sqrt{\pi}\left(\Omega_n + \Omega_*^a - \Omega_n\Omega_*^b\right)\left[\frac{3}{8} - \frac{1}{4}\Omega_n + \frac{1}{2}\Omega_n^2 + i\frac{1}{2}\Omega_n^{\frac{5}{2}} Z\left(i\Omega_n^{\frac{1}{2}}\right)\right]. \tag{43}$$

Without considering collisions, the only difference at this point between ions and electrons (with $n_i = n_e$ and $T_i = T_e$) are the signs of ω_D, ω_{*N}, and ω_{*T}. Therefore Ω_*^a and Ω_*^b are the same, while Ω_n has the opposite sign for ions and electrons. One can now easily see that changing the sign of $n\omega_E$ serves to effectively flip the identity of ions and electrons, as mentioned in section I A.

Here Z is the plasma dispersion function (Refs. [59], [13], and [60] (section 10.6)), given by:

$$Z(y) = \frac{1}{\sqrt{\pi}}\int_{-\infty}^{\infty}\frac{e^{-u^2}}{u-y}du. \tag{44}$$

In our case $y = i\Omega_n^{\frac{1}{2}}$. If we consider the collisionless case, Ω_n is real, so y is purely imaginary, which makes $Re(Z) = 0$ [59]. A comparison of the imaginary part of the plasma dispersion function calculation is shown in Fig. 11.

Note that the resonance condition of Eq. 42 is $\hat{\varepsilon} = -Re(\Omega_n)$. Therefore this solution is valid and there are no poles on the real, positive energy axis as long as $Re(\Omega_n) > 0$ or $Im(\Omega_n) \neq 0$, ie. there exists some finite damping, $\gamma + \nu_{\text{eff}} \neq 0$. If there are poles along the path of integration, then their residues must be calculated. Equation 42 can be written as $\int f(z)dz$, where $z = \hat{\varepsilon}$, and the residue is given by

$$\text{Res}(f, z \to -\Omega_n) = \lim_{z\to-\Omega_n}\left(z + \Omega_n\right) f(z) = \left(\Omega_n + \Omega_*^a - \Omega_n\Omega_*^b\right)\left(-\Omega_n\right)^{\frac{5}{2}} e^{\Omega_n} \tag{45}$$

Finally, one must also be careful of the locations in (Ψ, Λ) space where there is a drift reversal (ω_D goes through zero). In this case, one can show that the analytical solution to Eq. 40 is:

$$I_\varepsilon = \frac{15\sqrt{\pi}}{8}\left[\frac{n\left(\omega_{*N} + 2\omega_{*T}\right) + n\omega_E - \omega_r - i\gamma}{-i\nu_{\text{eff}} + n\omega_E - \omega_r - i\gamma}\right], \tag{46}$$

or, equivalently,

$$I_\varepsilon = \frac{15\sqrt{\pi}}{8}\left[1 + \frac{\Omega_*^a}{\Omega_n}\right] + \frac{105\sqrt{\pi}}{16}\left[\frac{\Omega_*^b}{\Omega_n}\right]. \tag{47}$$

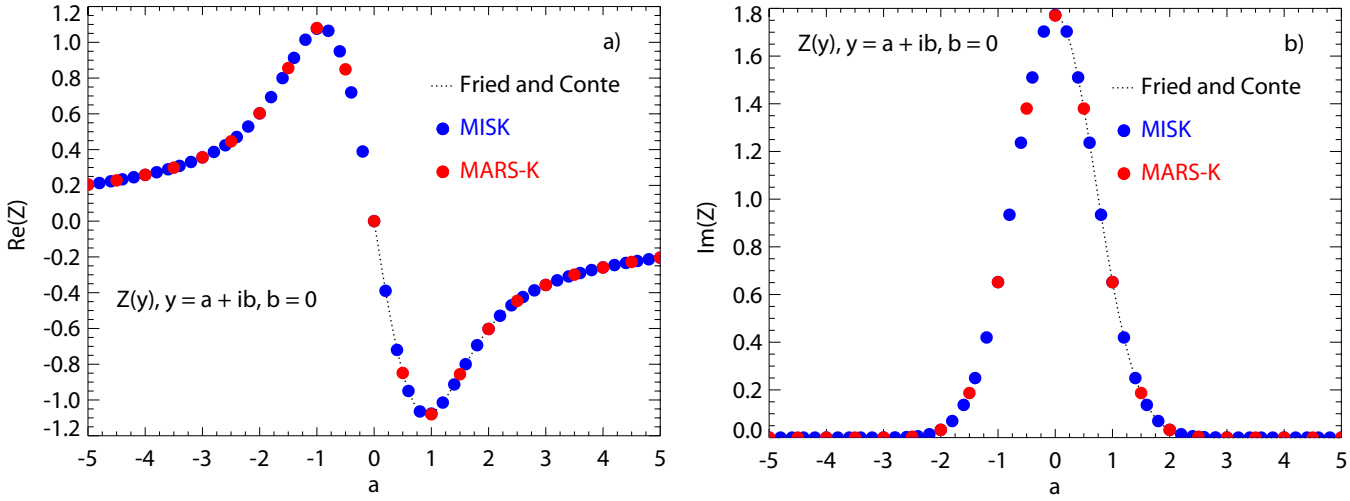

FIG. 12. A comparison of the calculation from `MARS-K` and `MISK` of the a) real and b) imaginary parts of the plasma dispersion function, $Z(y)$, for purely real y, to the curves given in Ref. [59].

3. ν_{eff} = constant (no energy dependence), $l \neq 0$ for trapped particles, and $|\omega_D| \ll |l\omega_b|$

This is the case again without energy-dependent collisions, for trapped particles with $l \neq 0$ where the precession drift frequency is neglected with respect to the bounce frequency. If we now define $\Omega_{n2} = (n\omega_E - \omega - i\nu_{\text{eff}})/(l\overline{\omega_b})$, $\Omega_*^{a2} = (n\omega_{*N} - \frac{3}{2}n\omega_{*T} + i\nu_{\text{eff}})/(l\overline{\omega_b})$, $\Omega_*^{b2} = n\omega_{*T}/l\overline{\omega_b}$, and $\omega_b = \overline{\omega_b}\hat{\varepsilon}^{\frac{1}{2}}$ (ie. $\overline{\omega_b}$ is the non-energy dependent portion of ω_b), then

$$I_\varepsilon = \int_0^\infty \frac{\Omega_*^{a2} + \Omega_{n2} + \hat{\varepsilon}\Omega_*^{b2}}{\frac{n\overline{\omega_D}}{l\overline{\omega_b}}\hat{\varepsilon} + \hat{\varepsilon}^{\frac{1}{2}} + \Omega_{n2}}\hat{\varepsilon}^{\frac{5}{2}}e^{-\hat{\varepsilon}}d\hat{\varepsilon}. \tag{48}$$

With $n\overline{\omega_D}/l\overline{\omega_b} \to 0$ this can be written

$$I_\varepsilon = -\frac{15\sqrt{\pi}}{8}\Omega_{n2}\Omega_*^{b2} + 2\left(\Omega_{n2} + \Omega_*^{a2} + \Omega_{n2}^2\Omega_*^{b2}\right)\left[-\sqrt{\pi}\Omega_{n2}\left(\frac{3}{8} + \frac{1}{4}\Omega_{n2}^2 + \frac{1}{2}\Omega_{n2}^4\right) - \frac{\sqrt{\pi}}{2}\Omega_{n2}^6 Z\left(\Omega_{n2}\right)\right.$$
$$\left. + \left(1 + \frac{1}{2}\Omega_{n2}^2 + \frac{1}{2}\Omega_{n2}^4\right) + \Omega_{n2}^6 e^{-\Omega_{n2}^2}\left(\int_0^1 \frac{e^{-|\Omega_{n2}|^2t^2} - e^{\Omega_{n2}^2t^2}}{t}dt + \int_0^1 \frac{e^{-|\Omega_{n2}|^2/t^2}}{t}dt - i(\angle\Omega_{n2} - \frac{\pi}{2})\right)\right] + 6\Omega_*^{b2}. \tag{49}$$

The second line above is odd with respect to Ω, and therefore odd in n as well (for $\omega = 0$ and $\nu_{\text{eff}} = 0$). Therefore the second line will change sign when n changes from 1 to -1. However, since the calculation of δW_K involves a summation over all l (positive and negative), this will not affect the final answer.

Note that in the collisionless case Ω_*^{a2} and Ω_{n2} are purely real (as well as Ω_*^{b2}), and the terms where imaginary I_ε comes from can be gathered together as:

$$Y(\Omega_{n2}) = -\frac{\sqrt{\pi}}{2}\Omega_{n2}Z\left(\Omega_{n2}\right) + \Omega_{n2}e^{-\Omega_{n2}^2}\left(\int_0^1 \frac{e^{-|\Omega_{n2}|^2t^2} - e^{\Omega_{n2}^2t^2}}{t}dt + \int_0^1 \frac{e^{-|\Omega_{n2}|^2/t^2}}{t}dt - i(\angle\Omega_{n2} - \frac{\pi}{2})\right). \tag{50}$$

Plots of $Z(y)$ and $Y(y)$ for real y are included in Figs. 12 and 13. Collisions will not be included in this work, however damping from finite γ will be explored briefly in section IX B. In that case imaginary I_ε comes from all terms, but it is important to show that the calculation of $Z(y)$ and $Y(y)$ are correct for complex y. One must be cautious about the $\angle\Omega_{n2}$ term in the above equation, as it can change the sign of the imaginary part of Y. Figures 14 and 15 show these comparisons.

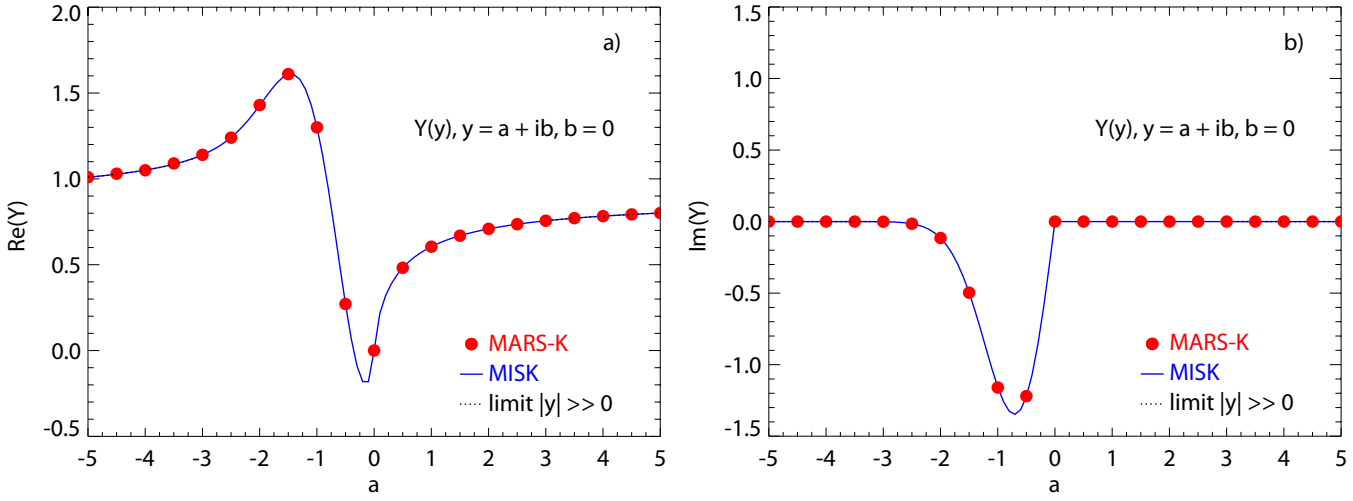

FIG. 13. A comparison of the calculation of the a) real and b) imaginary parts of $Y(y)$, for purely real y, between `MARS-K` and `MISK`.

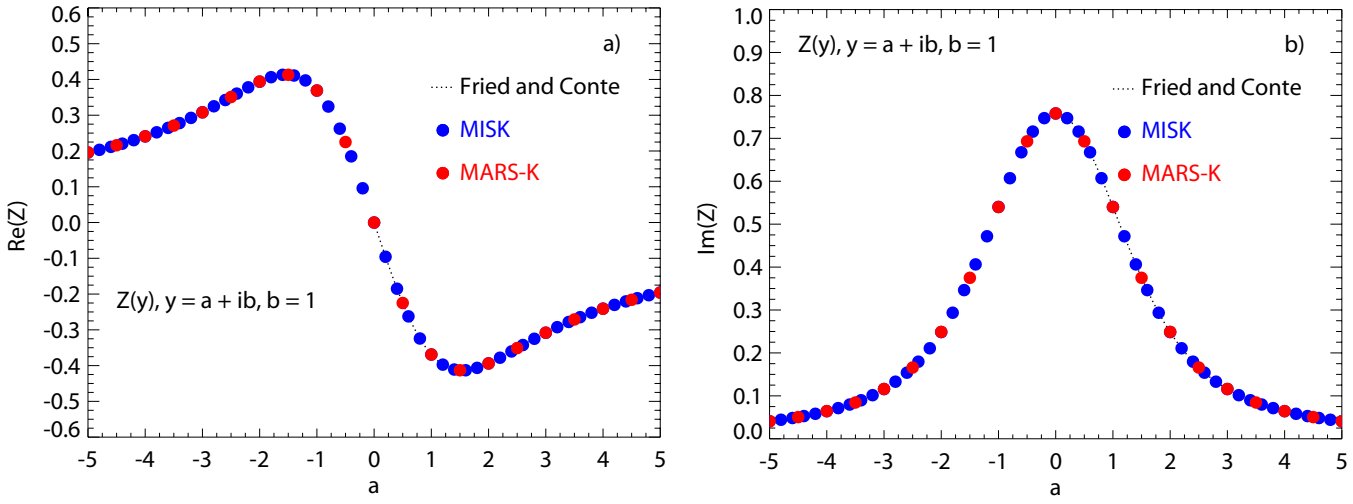

FIG. 14. A comparison of the calculations from `MARS-K` and `MISK` of the a) real and b) imaginary parts of the plasma dispersion function, $Z(y)$, for complex y, to the curves given in Ref. [59].

4. ν_{eff} = constant (no energy dependence), for circulating particles, and $|\omega_D| \ll |\sigma(nq+l)\omega_t|$

Note that Eq. 49 can also be used for circulating particles, with $l\overline{\omega_b} \to \sigma(nq+l)\overline{\omega_t}$, where ω_t indicates the transit frequency. The inclusion of σ (the sign of $v_\parallel$) actually means that the terms that are odd in Ω in Eq. 49 will cancel out when the summation over positive and negative σ are taken. Therefore, for circulating particles, a simplified expression can be used in which only the first line of Eq. 49 is used:

$$I_\varepsilon = -\frac{15\sqrt{\pi}}{8}\Omega_{n2}\Omega_*^{b2} + 2\left(\Omega_{n2} + \Omega_*^{a2} + \Omega_{n2}^2\Omega_*^{b2}\right)\left[-\sqrt{\pi}\Omega_{n2}\left(\frac{3}{8} + \frac{1}{4}\Omega_{n2}^2 + \frac{1}{2}\Omega_{n2}^4\right) - \frac{\sqrt{\pi}}{2}\Omega_{n2}^6 Z\left(\Omega_{n2}\right)\right]. \quad (51)$$

This expression is once again even in n, and so it will not change whether n is positive or negative.

B. Energy Integral Comparison

Performing the energy integration, we can plot I_ε as a function of Λ. Figure 16 shows each l component of I_ε from -2 to 2 for trapped thermal ions in the Solov'ev 1 equilibrium at $r/R_0 = 0.08$ ($\Psi_n = 0.16$), the same surface

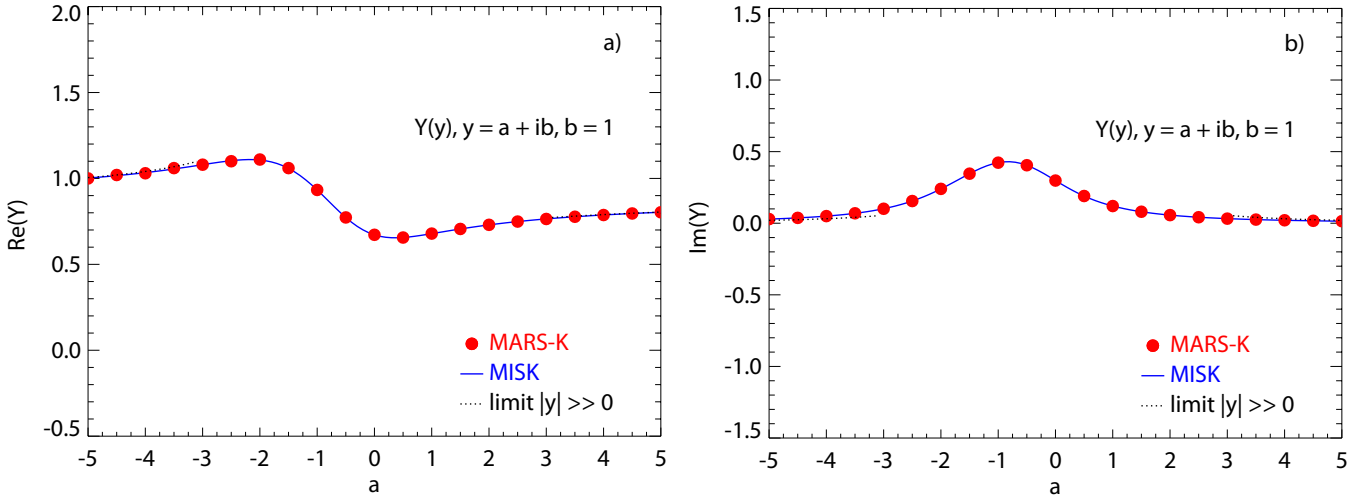

FIG. 15. A comparison of the calculation of the a) real and b) imaginary parts of $Y(y)$, for complex y, between `MARS-K` and `MISK`.

chosen in Fig. 7. Figures 17 and 18 show each l component of I_ε from -2 to 2 for trapped thermal ions in the Solov'ev 3 equilibrium at $r/R_0 = 0.252$ ($\Psi_n = 0.585, q = 2.5$), and the ITER equilibrium at $r/R_0 = 0.322$ ($\Psi_n = 0.982$), respectively. The traces are plotted as l/n so that they are equivalent for $n = -1$ or $n = 1$.

Figure 19 shows each l component of I_ε from -2 to 2 for circulating thermal ions in the Solov'ev 1 equilibrium at $r/R_0 = 0.08$ ($\Psi_n = 0.16$), while Fig. 20 shows the same at $\Psi_n = 0.64$.

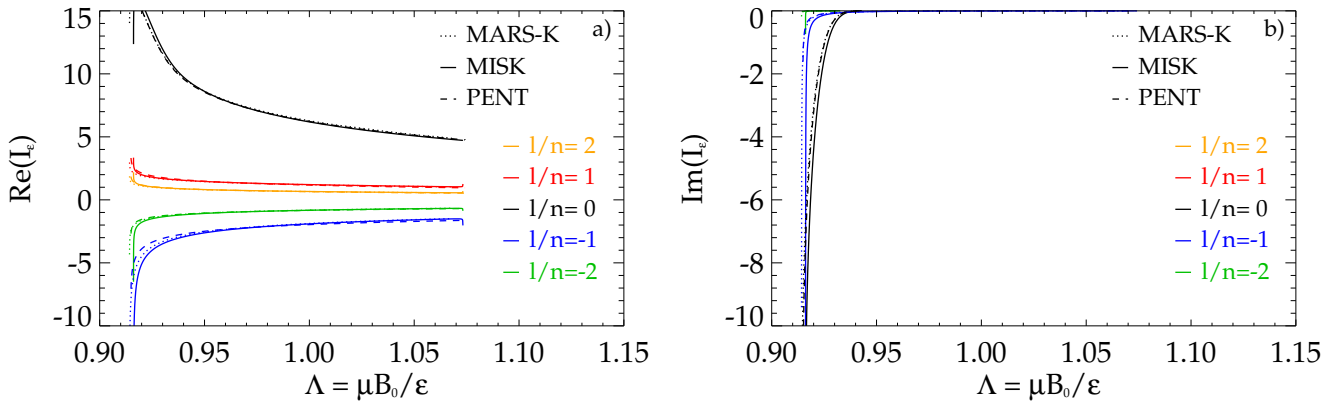

FIG. 16. a) Real and b) imaginary components of I_ε for each l/n from -2 to 2, vs. Λ for trapped thermal ions in the Solov'ev 1 equilibrium at $r/R_0 = 0.08$ ($\Psi_n = 0.16$), calculated by `MARS-K`, `MISK`, and `PENT`.

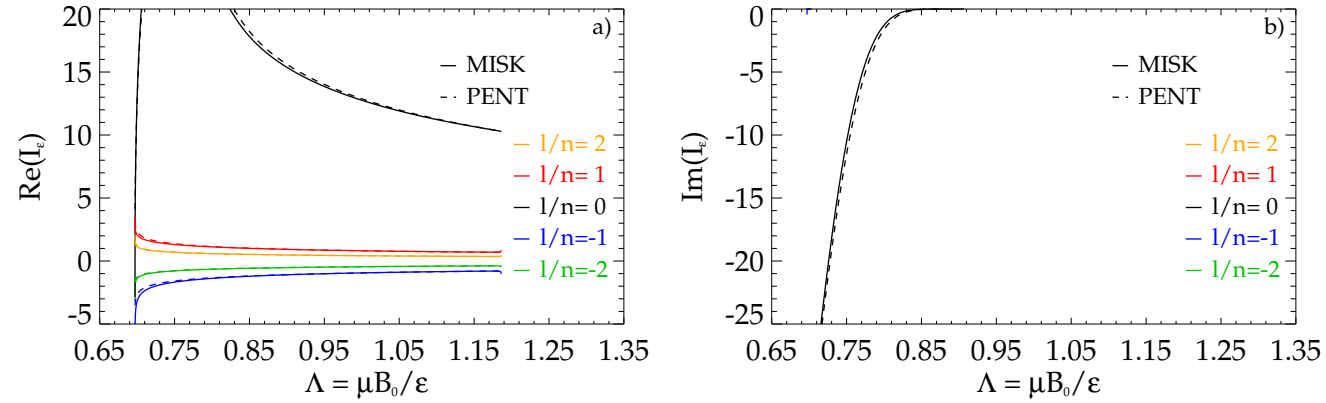

FIG. 17. a) Real and b) imaginary components of I_ε for each l/n from -2 to 2, vs. Λ for trapped thermal ions in the Solov'ev 3 equilibrium at $r/R_0 = 0.252$ ($\Psi_n = 0.585, q = 2.5$), calculated by `MISK` and `PENT`.

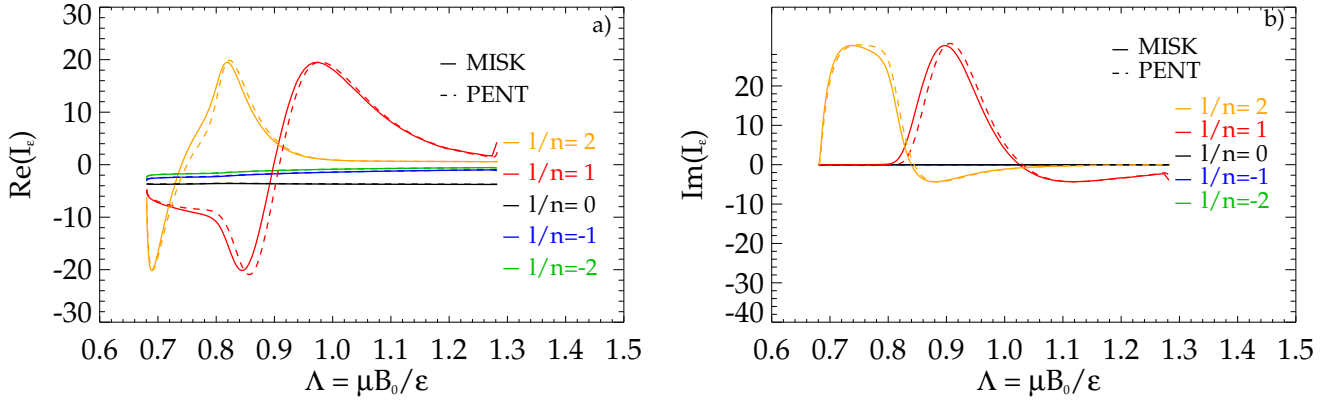

FIG. 18. a) Real and b) imaginary components of I_ε for each l/n from -4 to 4, vs. Λ for trapped thermal ions in the ITER equilibrium at $r/R_0 = 0.322$ ($\Psi_n = 0.982$), calculated by `MISK` and `PENT`.

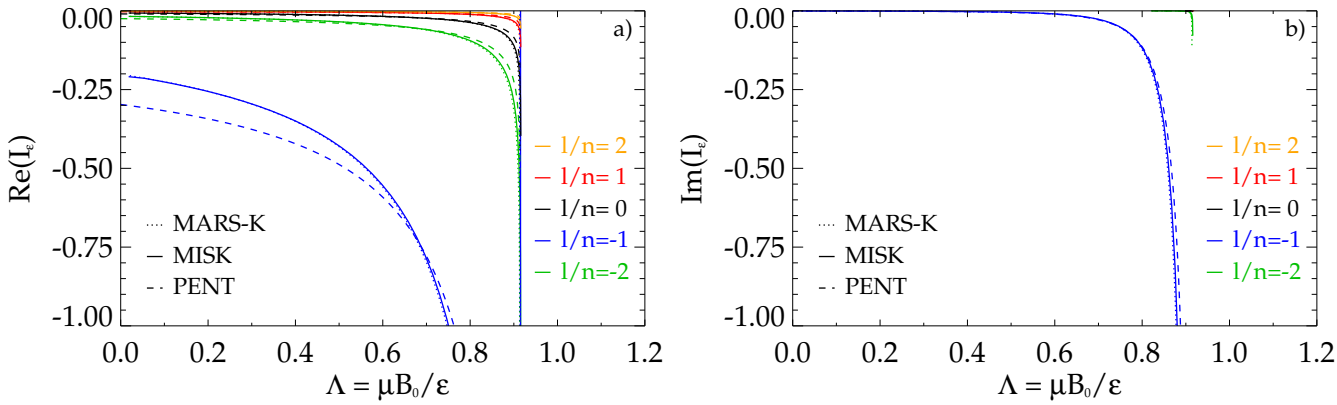

FIG. 19. a) Real and b) imaginary components of I_ε for each l/n from -2 to 2, vs. Λ for circulating thermal ions in the Solov'ev 1 equilibrium at $r/R_0 = 0.08$ ($\Psi_n = 0.16$), calculated by `MARS-K`, `MISK`, and `PENT`.

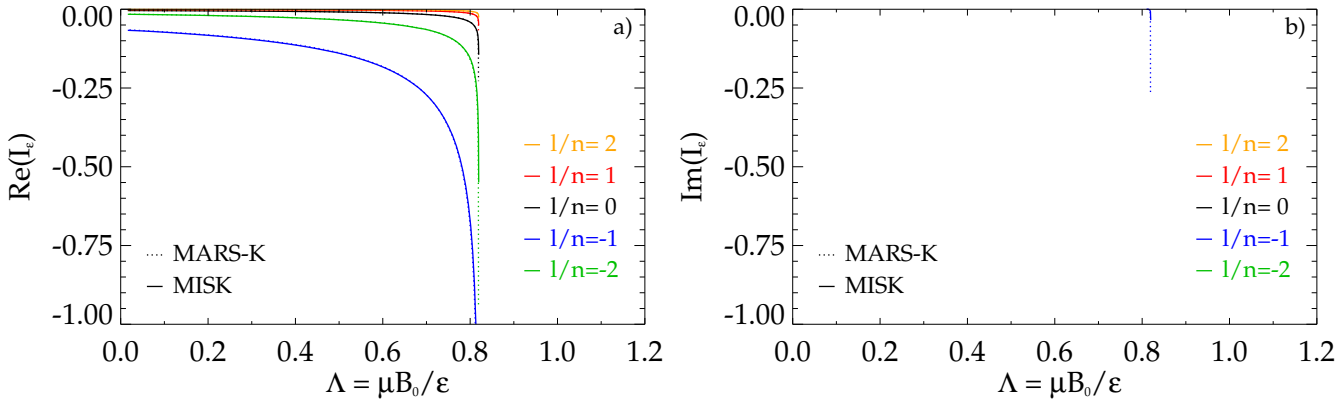

FIG. 20. a) Real and b) imaginary components of I_ε for each l/n from -2 to 2, vs. Λ for circulating thermal ions in the Solov'ev 1 equilibrium at $\Psi_n = 0.64$, calculated by `MARS-K` and `MISK`.

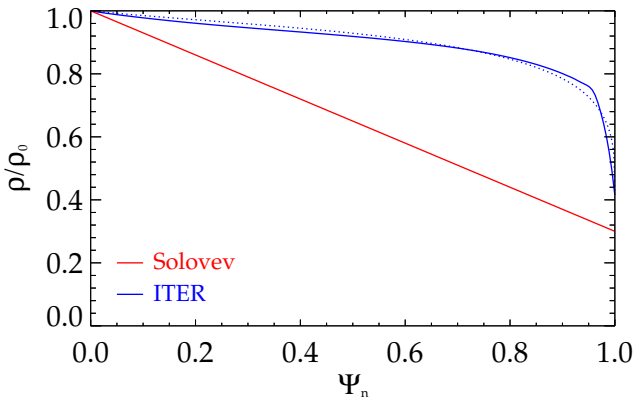

FIG. 21. Normalized mass density profiles for the Solov'ev and ITER cases. The dashed lines are the approximations used in PEST (overlays in the Solov'ev case).

VI. EIGENFUNCTION COMPARISON

The normalized mass density profile, ρ/ρ_0, affects the eigenfunction. For the Solov'ev case, the normalized mass density profile $\rho/\rho_0 = (m_e n_e + m_i n_i + m_\alpha n_\alpha)/(m_e n_{e0} + m_i n_{i0} + m_\alpha n_{\alpha 0})$ reduces to $\rho/\rho_0 = 1 - 0.7\Psi_n$. For the ITER case ρ/ρ_0 is calculated from the individual density profiles and plotted in Fig. 21, along with the linear profile for the Solov'ev cases. PEST is limited in the mass density profiles it can take as an input, so approximations are used, which are shown in dashed lines.

Figures 22a, 24a, and 26a compare the poloidal Fourier harmonics of the normal displacement $\xi \cdot \nabla\sqrt{\Psi_n}$ vs. $\sqrt{\Psi_n}$ for an ideal kink mode without a wall computed by MARS-K, MISHKA, and PEST for the Solov'ev 1, Solov'ev 3, and ITER cases, in PEST coordinates. The Fourier harmonics following this definition have more physical meaning (a better separation between resonant and non-resonant harmonics) than using equal-arc coordinates. The same quantity is plotted for the same equilibria in equal-arc coordinates in Figs. 22b, 24b, and 26b. Figure 24b can be directly compared to Fig. 10(a) of Ref. [14].

As an approximation to the fluid RWM, MISK uses the marginally stable ideal kink with an ideal wall, as calculated by PEST by moving the wall position progressively inward until the marginal point is found[11]. This eigenfunction is a good approximation to the fluid RWM[14]. Figures 23, 25, and 27 compare the poloidal Fourier harmonics of the normal displacement $\boldsymbol{\xi} \cdot \nabla\sqrt{\Psi_n}$ vs. $\sqrt{\Psi_n}$ for a maginally stable ideal kink mode with an ideal wall computed by PEST to the fluid RWM eigenfunctions computed by MARS-K and MISHKA, for the three equilibria in PEST coordinates and equal-arc coordinates. Note that the PEST representation of $\boldsymbol{\xi}$ can be found in Ref. [61]. Since MISHKA does not include a resistive wall, it is not included in this comparison. Figure 25b can be directly compared to the fluid RWM eigenfunction in Fig. 10(b) of Ref. [14].

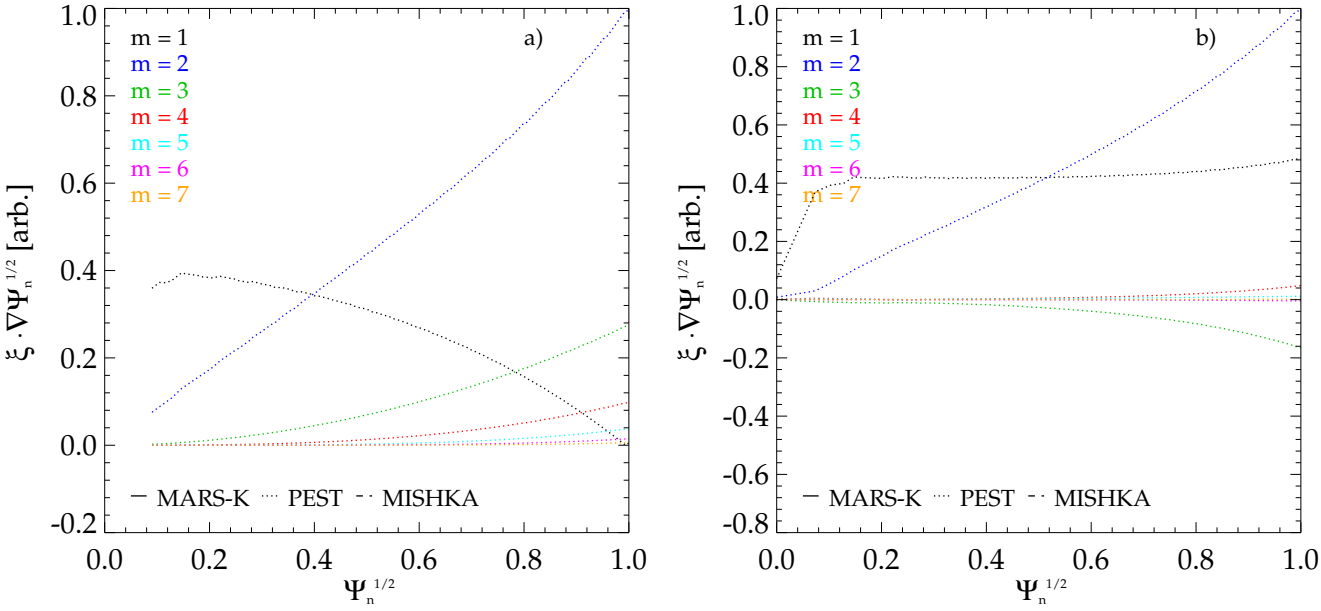

FIG. 22. Poloidal Fourier harmonics of the normal displacement for an ideal kink mode without a wall for the Solov'ev 1 equilibrium, as computed by PEST, in a) PEST and b) equal-arc coordinate systems.

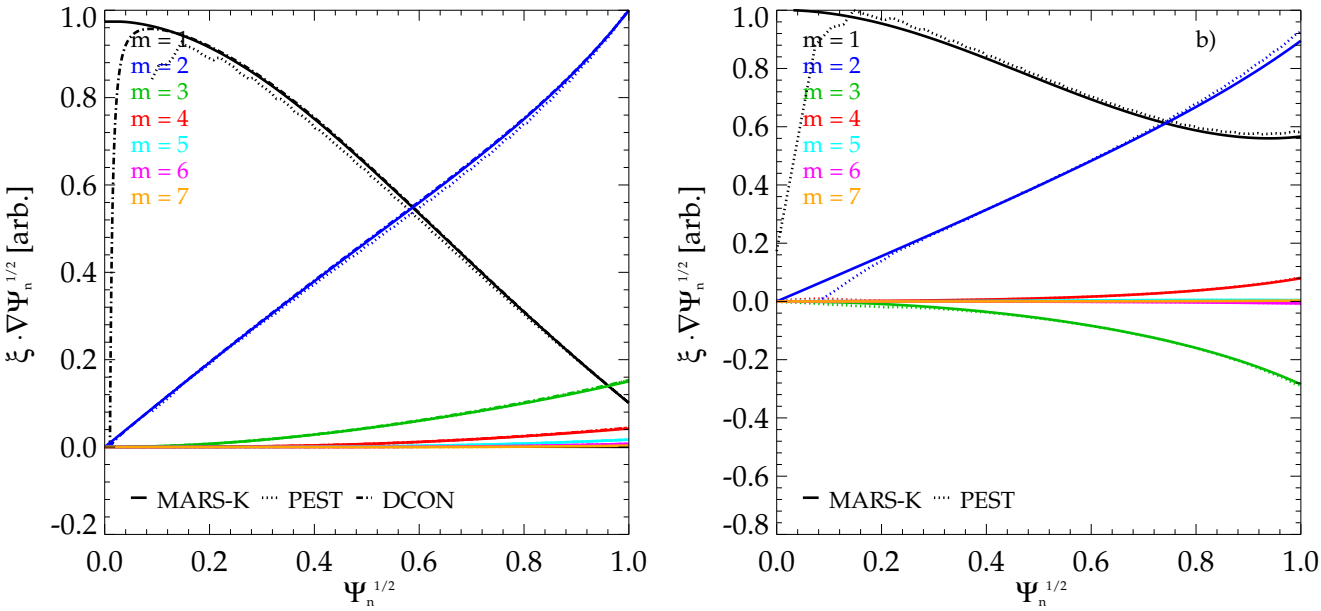

FIG. 23. Poloidal Fourier harmonics of the normal displacement for the marginally stable ideal kink mode with an ideal wall for the Solov'ev 1 equilibrium, as computed by PEST and DCON, and the fluid RWM eigenfunction as computed by MARS-K, in a) PEST and b) equal-arc coordinate systems.

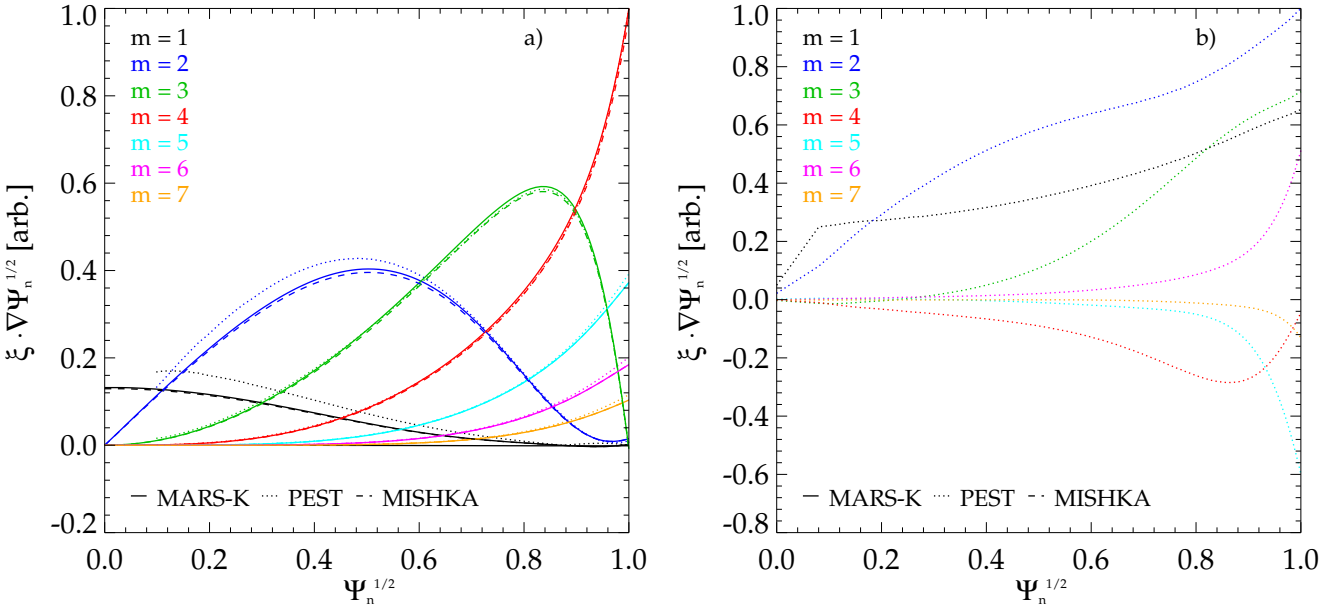

FIG. 24. Poloidal Fourier harmonics of the normal displacement for an ideal kink mode without a wall for the Solov'ev 3 equilibrium, as computed by `MARS-K`, `MISHKA`, and `PEST`, in a) `PEST` coordinates, and by `PEST` in b) equal-arc coordinates.

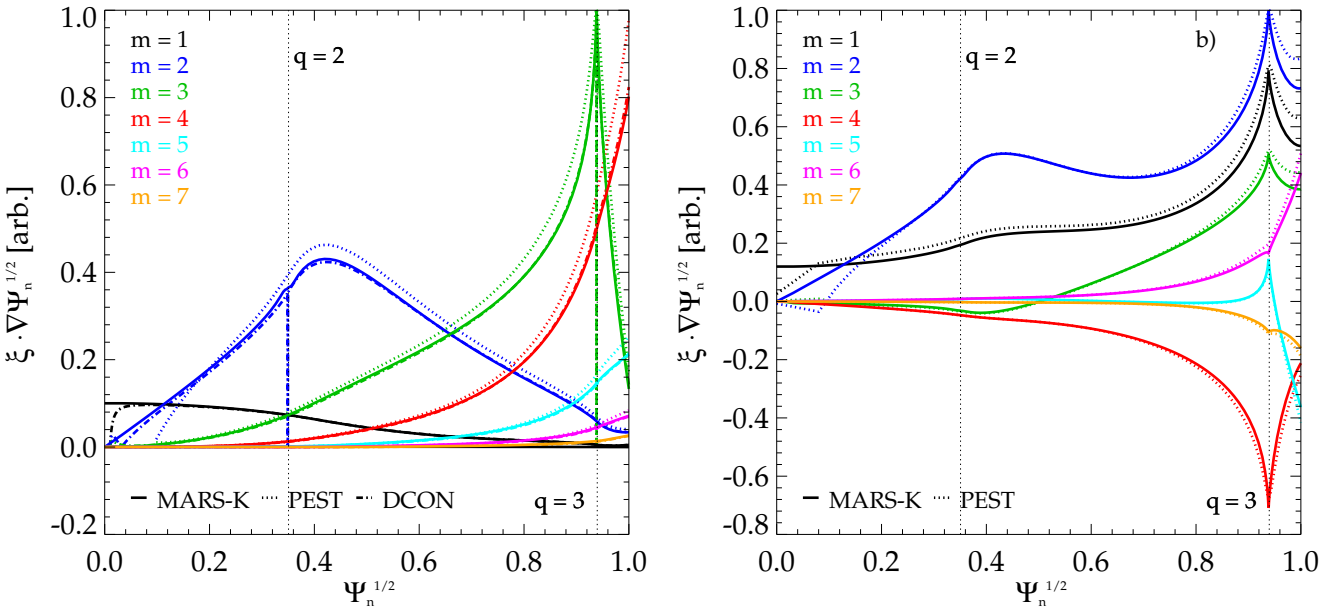

FIG. 25. Poloidal Fourier harmonics of the normal displacement for the marginally stable ideal kink mode with an ideal wall for the Solov'ev 3 equilibrium, as computed by `PEST` and `DCON`, and the fluid RWM eigenfunction as computed by `MARS-K`, in a) `PEST` and b) equal-arc coordinate systems.

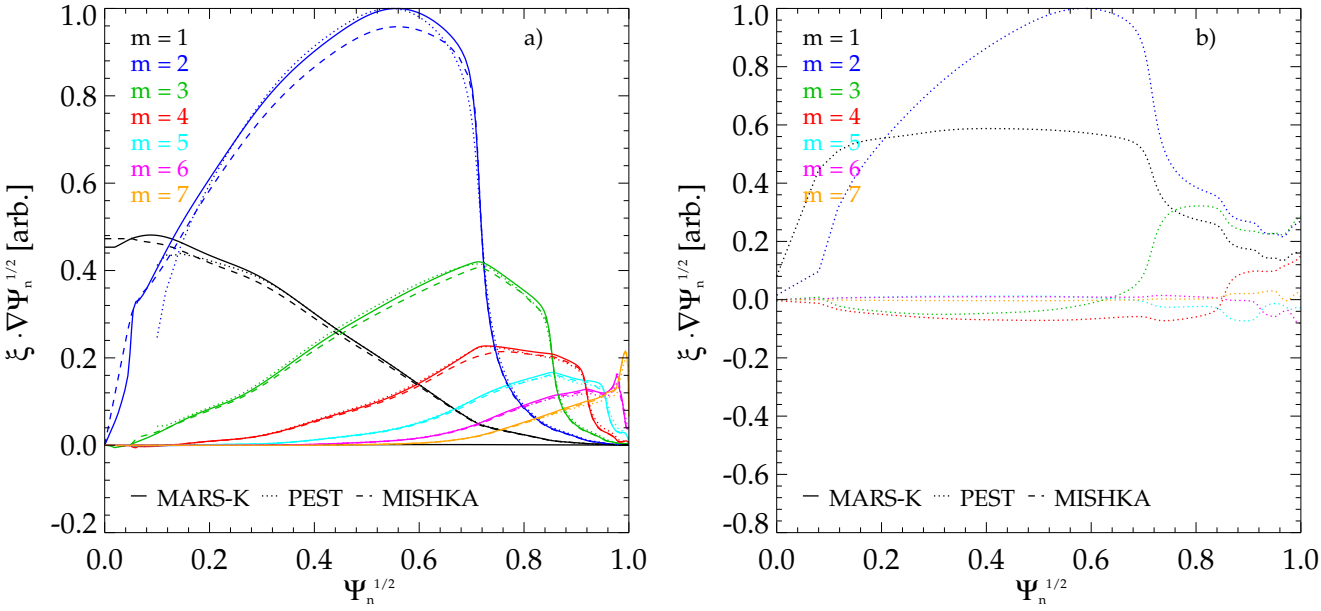

FIG. 26. Poloidal Fourier harmonics of the normal displacement for an ideal kink mode without a wall for the ITER equilibrium, as computed by `MARS-K`, `MISHKA`, and `PEST`, in a) `PEST` coordinates, and by `PEST` in b) equal-arc coordinates.

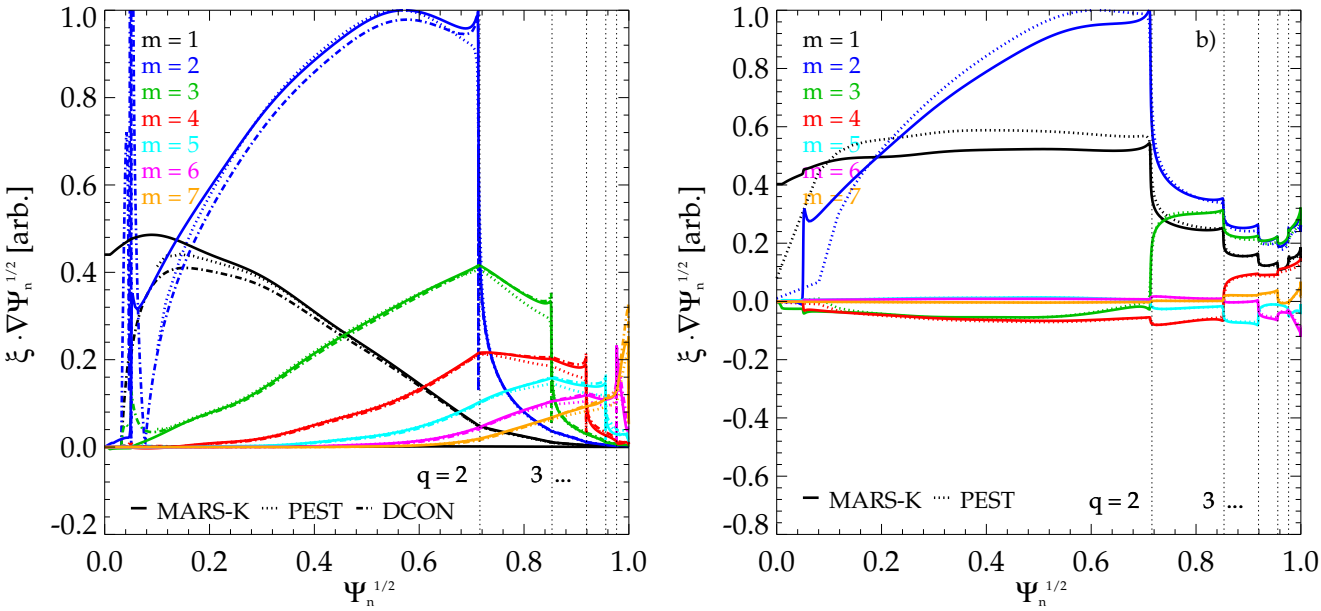

FIG. 27. Poloidal Fourier harmonics of the normal displacement for the marginally stable ideal kink mode with an ideal wall for the ITER equilibrium, as computed by `PEST` and `DCON`, and the fluid RWM eigenfunction as computed by `MARS-K`, in a) `PEST` and b) equal-arc coordinate systems.

VII. THE PERTURBED LAGRANGIAN

Another major part of the kinetic calculation is the perturbed Lagrangian[14]:

$$\langle H/\hat{\varepsilon}\rangle(\Psi,\Lambda,l)=\frac{1}{\hat{\tau}}\oint\frac{1}{\sqrt{1-\frac{\Lambda B}{B_0}}}\left[\left(2-3\frac{\Lambda B}{B_0}\right)(\boldsymbol{\kappa}\cdot\boldsymbol{\xi}_\perp)-\left(\frac{\Lambda B}{B_0}\right)(\boldsymbol{\nabla}\cdot\boldsymbol{\xi}_\perp)\right]e^{in\phi-i(l+\alpha nq)\omega_b t}d\boldsymbol{\ell}. \tag{52}$$

Here $\langle\cdot\rangle$ indicates a bounce average, ϕ is the toroidal angle, and $\boldsymbol{\kappa}=\hat{\mathbf{b}}\cdot\boldsymbol{\nabla}\hat{\mathbf{b}}$ is the magnetic curvature.

Similarly to how the energy integral of the frequency resonance fraction can be calculated solely based on the frequencies and encompasses all the energy dependence of the problem, the perturbed Lagrangian can be calculated based mostly on the eigenfunction (although ω_b also appears in the phase term), and indeed is the only place in the problem where the eigenfunction appears.

Like in Sec. V with $I_{\hat{\varepsilon}}$, we can make plots of $\langle H/\hat{\varepsilon}\rangle$ vs. Λ for particular Ψ surfaces. Figure 28 shows each l component of $\langle H/\hat{\varepsilon}\rangle$ for trapped thermal ions from -2 to 2 in the Solov'ev 1 equilibrium at $r/R_0=0.08$ ($\Psi_n=0.16$), the same surface chosen in Fig. 7. Figure 29 shows each l component of $\langle H/\hat{\varepsilon}\rangle$ for trapped thermal ions from -2 to 2 in the Solov'ev 3 equilibrium at $r/R_0=0.252$ ($\Psi_n=0.585, q=2.5$). Figure 30 shows shows each l component of $\langle H/\hat{\varepsilon}\rangle$ from -2 to 2 in the ITER equilibrium at $r/R_0=0.322$ ($\Psi_n=0.982$).

Note that like the bounce and precession frequencies, this quantity has a singularity when $v_\parallel\to 0$, but it is integrable.

It can be shown that for trapped particles in an up-down symmetric equilibrium, $Im(\langle H/\hat{\varepsilon}\rangle)=0$ (which can be seen in Figs. 28b and 29b), and that $\langle H/\hat{\varepsilon}\rangle(-l)$ should be equal to $\langle H/\hat{\varepsilon}\rangle(+l)$ (which can be seen in Figs. 28a and 29a for `PENT`. Although this isn't the case for `MISK` for the $l/n=\pm1$ cases, it does not affect the answer, as $|\langle H\rangle|^2$ is used).

It is also useful to examine the constituents of $\langle H/\hat{\varepsilon}\rangle$ separately. Figures 31 and 32 show $\boldsymbol{\kappa}\cdot\boldsymbol{\xi}_\perp$ and $\boldsymbol{\nabla}\cdot\boldsymbol{\xi}_\perp$, respectively, as functions of θ for the Solov'ev 1 equilibrium at $r/R_0=0.08$ ($\Psi_n=0.16$). Similarly, Figs. 37 and 38 are for the Solov'ev 3 equilibrium at $\Psi_n=0.585$ and Figs. 39 and 40 are for the Solov'ev 3 equilibrium at $\Psi_n=0.9$. Figures 33-36 show contours of the real and imaginary parts of $\boldsymbol{\kappa}\cdot\boldsymbol{\xi}_\perp$ and $\boldsymbol{\nabla}\cdot\boldsymbol{\xi}_\perp$ for the Solov'ev 3 case. Because the quantities are presented in arbitrary units, in each of these figures (31-42) the quantities have been renormalized between the codes to show their equivalence on the same plots.

Note that $\boldsymbol{\kappa}\cdot\boldsymbol{\xi}_\perp$ and $\boldsymbol{\nabla}\cdot\boldsymbol{\xi}_\perp$ are related by the definition of the perturbed parallel magnetic field $\tilde{\mathbf{B}}_\parallel$:

$$\tilde{\mathbf{B}}_\parallel=-B\left(\boldsymbol{\nabla}\cdot\boldsymbol{\xi}_\perp+2\boldsymbol{\kappa}\cdot\boldsymbol{\xi}_\perp-\boldsymbol{\xi}_\perp\cdot\boldsymbol{\nabla}\left(\frac{\mu_0 p}{B^2}\right)\right). \tag{53}$$

Finally, one must be cautious in evaluating $\boldsymbol{\nabla}\cdot\boldsymbol{\xi}_\perp$, as the $\partial/\partial\phi$ component of $\boldsymbol{\nabla}\cdot$ will change sign whether one uses $n=1$ or -1.

One concern is that at rational surfaces Alfvén resonances can lead to singularities in the calculation of δW_K[11]. Indeed, by plotting $\boldsymbol{\kappa}\cdot\boldsymbol{\xi}_\perp$ and $\boldsymbol{\nabla}\cdot\boldsymbol{\xi}_\perp$, respectively, as functions of Ψ_n for a given θ, as in Figs. 41 and 42 for the Solov'ev 3 case, we can see that the rational surface is a cause of difference between the codes. In this case integration is performed smoothly across these surfaces; no special considerations such as replacing the calculation in the vicinity of the rational surfaces with an analytic calculation[20,62] are taken. Therefore in subsection IX C when we examine δW_K as a function of Ψ_n for the Solov'ev 3 case, we will see that there is a difference in the final answer for δW_K between the codes that arises from the treatment of the rational surfaces. In contrast, in the ITER case, singularities were found at the rational surface. The treatment of this issue will be discussed in subsection IX C.

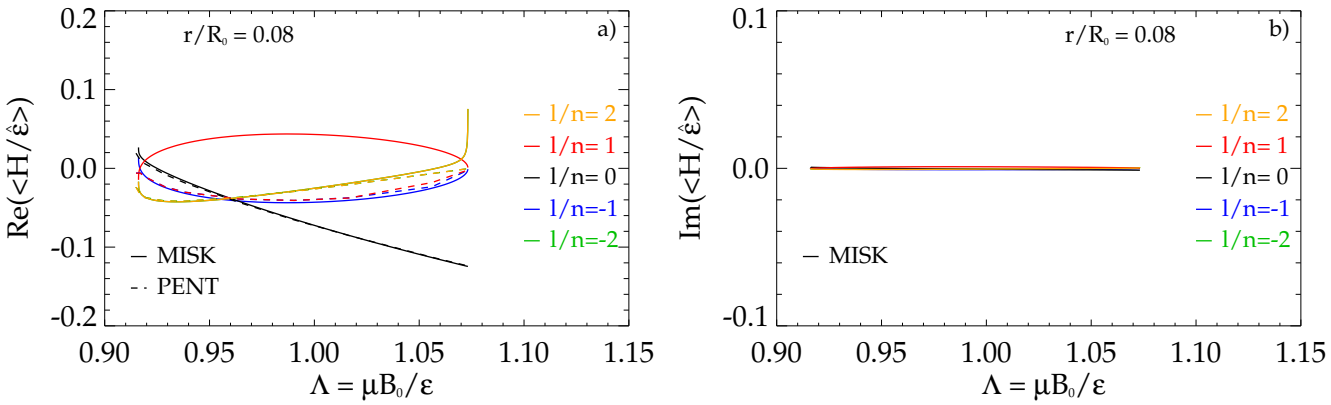

FIG. 28. a) Real and b) imaginary components of $\langle H/\hat{\varepsilon}\rangle$ for trapped thermal ions for each l from -2 to 2, vs. Λ in the Solov'ev 1 equilibrium at $r/R_0 = 0.08$ ($\Psi_n = 0.16$), calculated by `MISK` and `PENT`.

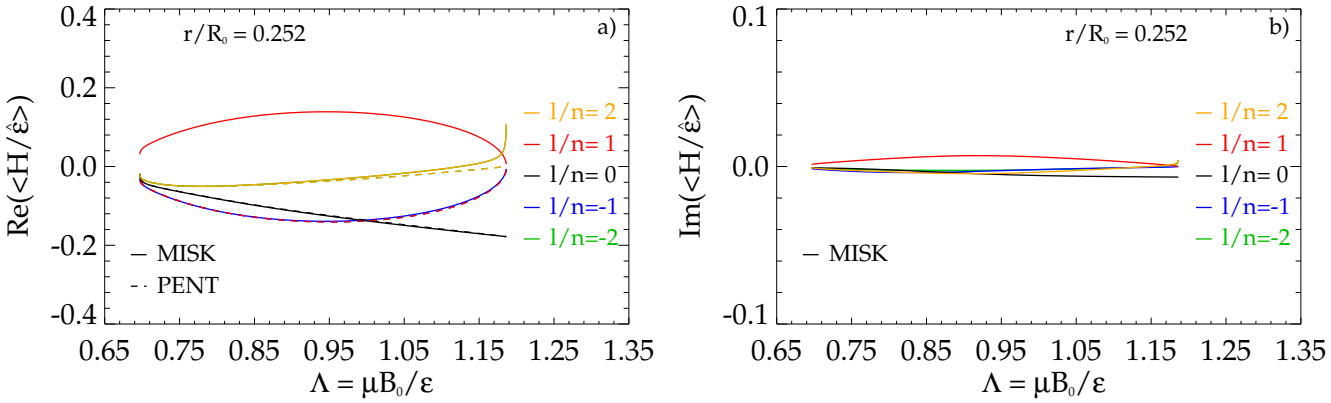

FIG. 29. a) Real and b) imaginary components of $\langle H/\hat{\varepsilon}\rangle$ for trapped thermal ions for each l from -2 to 2, vs. Λ in the Solov'ev 3 equilibrium at $r/R_0 = 0.252$ ($\Psi_n = 0.585, q = 2.5$), calculated by `MISK` and `PENT`.

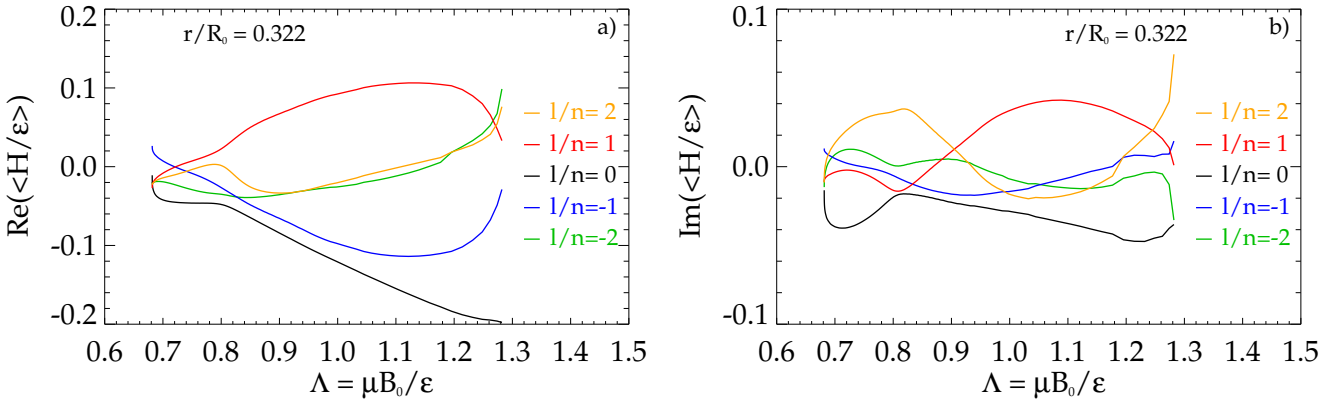

FIG. 30. a) Real and b) imaginary components of $\langle H/\hat{\varepsilon}\rangle$ for trapped thermal ions for each l from -2 to 2, vs. Λ in the ITER equilibrium at $r/R_0 = 0.322$ ($\Psi_n = 0.982$), calculated by `MISK`.

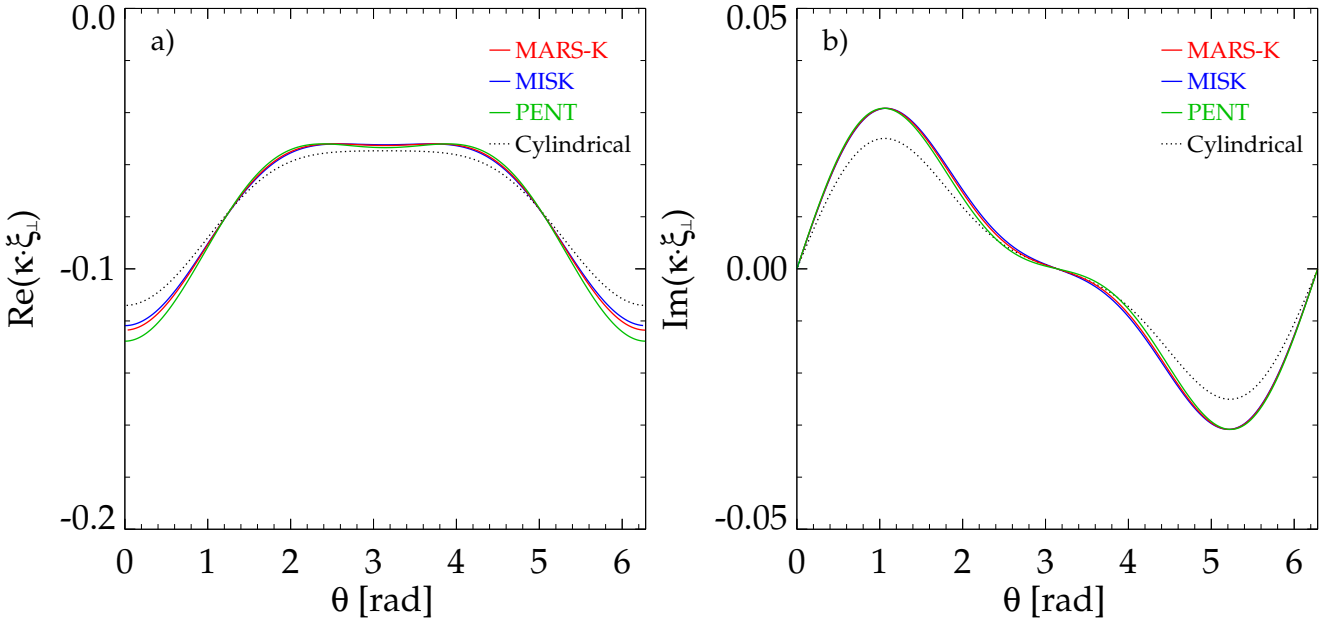

FIG. 31. a) Real and b) imaginary components of $\kappa \cdot \xi_\perp$ vs. θ in the Solov'ev 1 equilibrium at $r/R_0 = 0.08$ ($\Psi_n = 0.16$), calculated by `MISK`, `MARS-K`, and `PENT`. The `MARS-K` and `PENT` results are renormalized by making the maximum value anywhere in the plasma the same as the `MISK` maximum.

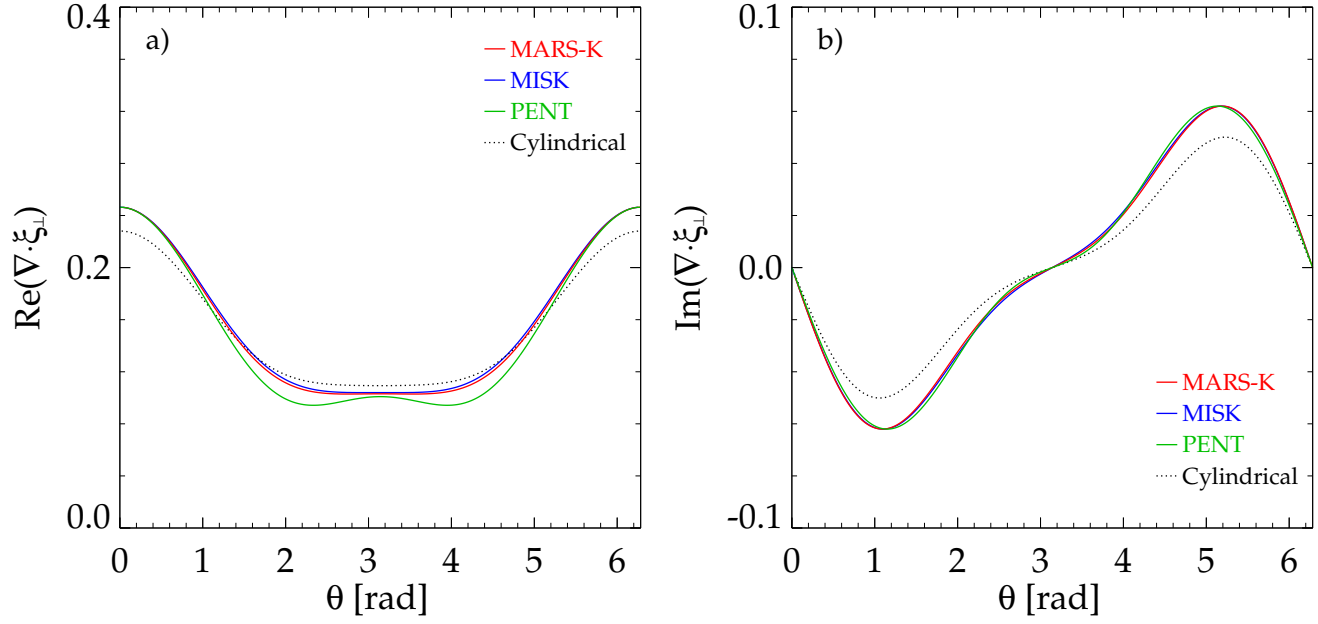

FIG. 32. a) Real and b) imaginary components of $\nabla \cdot \xi_\perp$ vs. θ in the Solov'ev 1 equilibrium at $r/R_0 = 0.08$ ($\Psi_n = 0.16$), calculated by `MISK`, `MARS-K`, and `PENT` . The `MARS-K` and `PENT` results are renormalized by making the maximum value anywhere in the plasma the same as the `MISK` maximum.

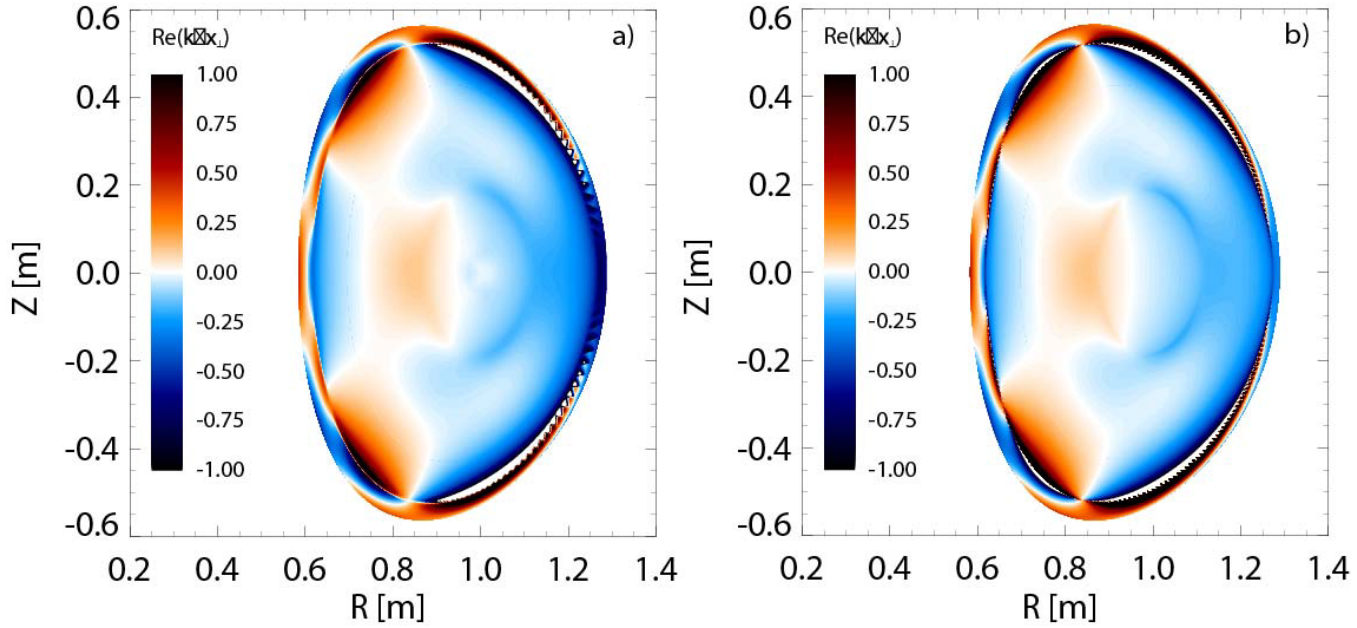

FIG. 33. $Re(\kappa \cdot \xi_\perp)$ in the Solov'ev 3 equilibrium, calculated by a) MISK and b) MARS-K. The MARS-K results are renormalized by making the maximum value at $r/R_0 = 0.252$ ($\Psi_n = 0.585, q = 2.5$) the same as the MISK maximum.

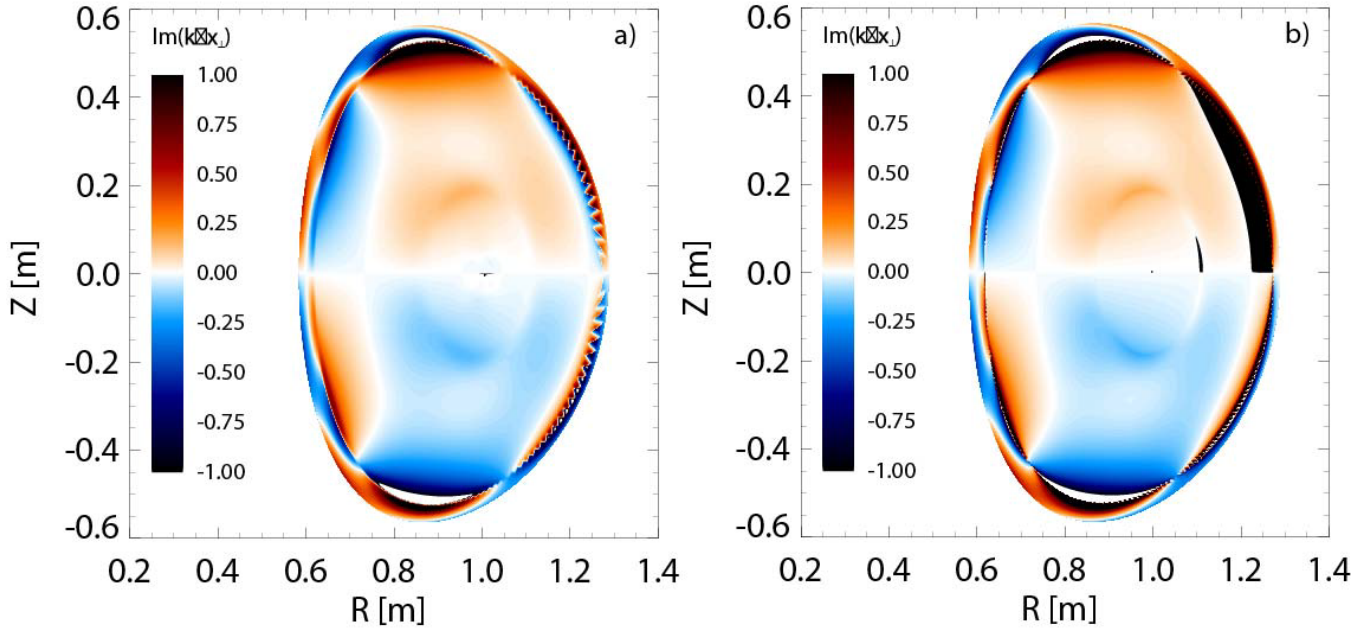

FIG. 34. $Im(\kappa \cdot \xi_\perp)$ in the Solov'ev 3 equilibrium, calculated by a) MISK and b) MARS-K. The MARS-K results are renormalized by making the maximum value at $r/R_0 = 0.252$ ($\Psi_n = 0.585, q = 2.5$) the same as the MISK maximum.

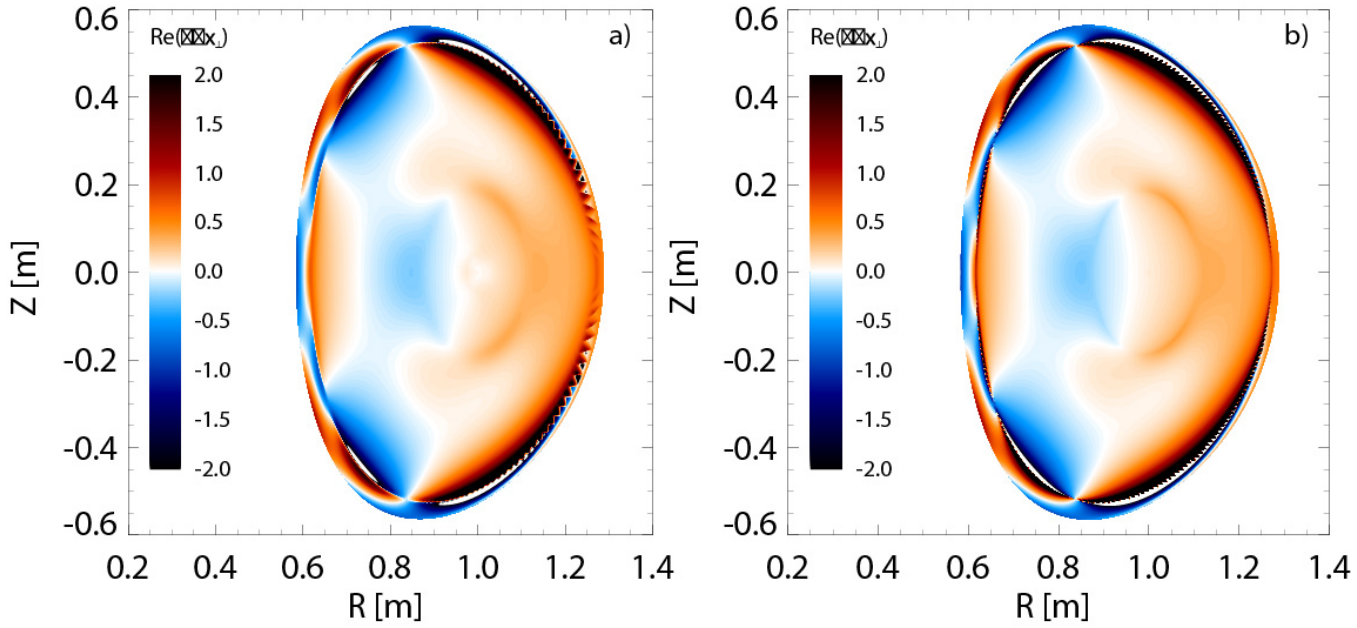

FIG. 35. $Re(\nabla \cdot \xi_\perp)$ in the Solov'ev 3 equilibrium, calculated by a) MISK and b) MARS-K. The MARS-K results are renormalized by making the maximum value at $r/R_0 = 0.252$ ($\Psi_n = 0.585, q = 2.5$) the same as the MISK maximum.

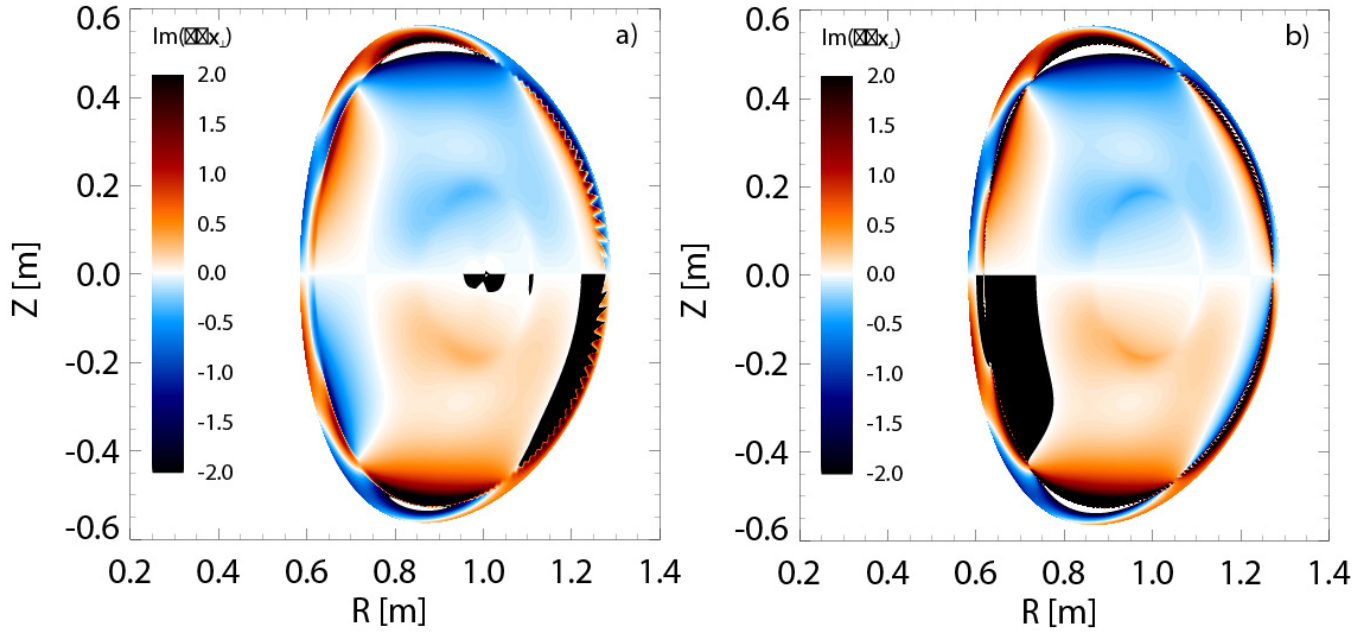

FIG. 36. $Im(\nabla \cdot \xi_\perp)$ in the Solov'ev 3 equilibrium, calculated by a) MISK and b) MARS-K. The MARS-K results are renormalized by making the maximum value at $r/R_0 = 0.252$ ($\Psi_n = 0.585, q = 2.5$) the same as the MISK maximum.

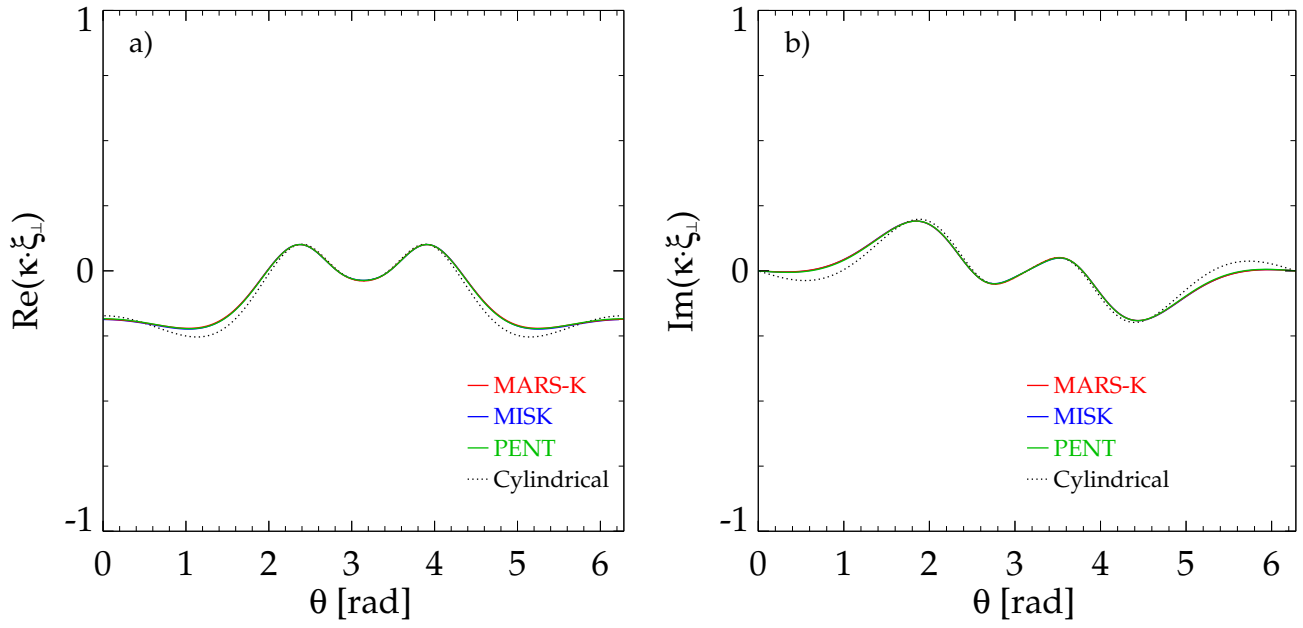

FIG. 37. a) Real and b) imaginary components of $\kappa \cdot \xi_\perp$ vs. θ in the Solov'ev 3 equilibrium at $r/R_0 = 0.252$ ($\Psi_n = 0.585, q = 2.5$), calculated by `MISK`, `MARS-K`, and `PENT`. The `MARS-K` and `PENT` results are renormalized by making the maximum value on this surface the same as the `MISK` maximum.

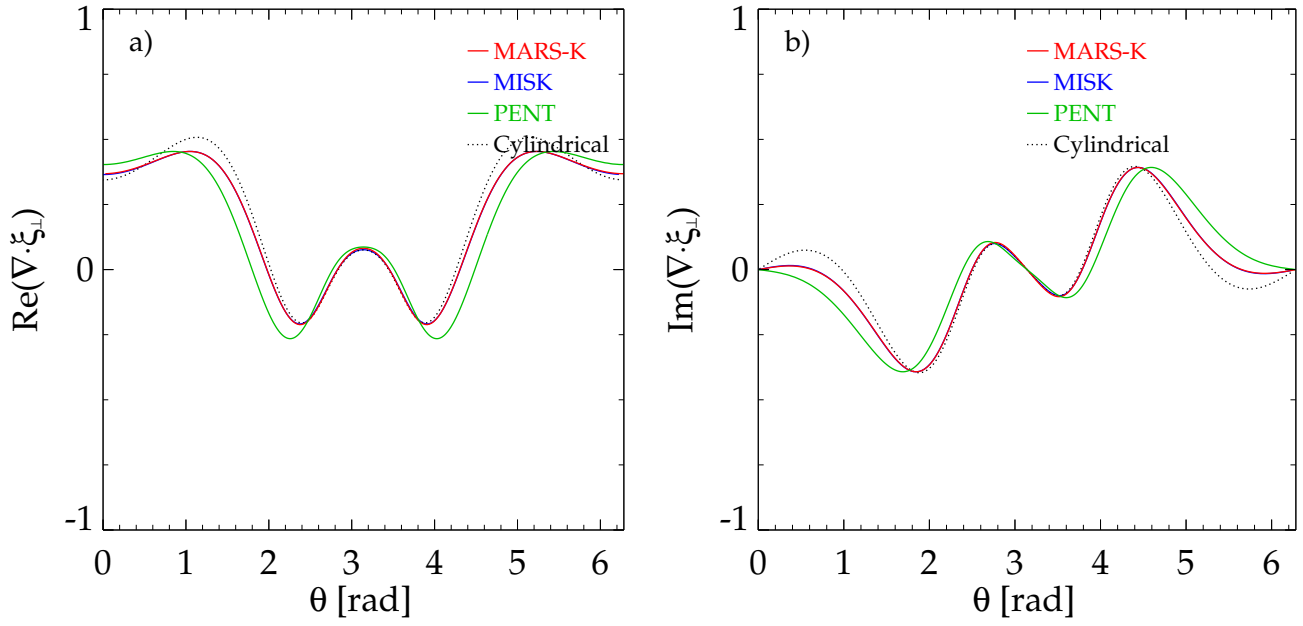

FIG. 38. a) Real and b) imaginary components of $\nabla \cdot \xi_\perp$ vs. θ in the Solov'ev 3 equilibrium at $r/R_0 = 0.252$ ($\Psi_n = 0.585, q = 2.5$), calculated by `MISK`, `MARS-K`, and `PENT`. The `MARS-K` and `PENT` results are renormalized by making the maximum value on this surface the same as the `MISK` maximum.

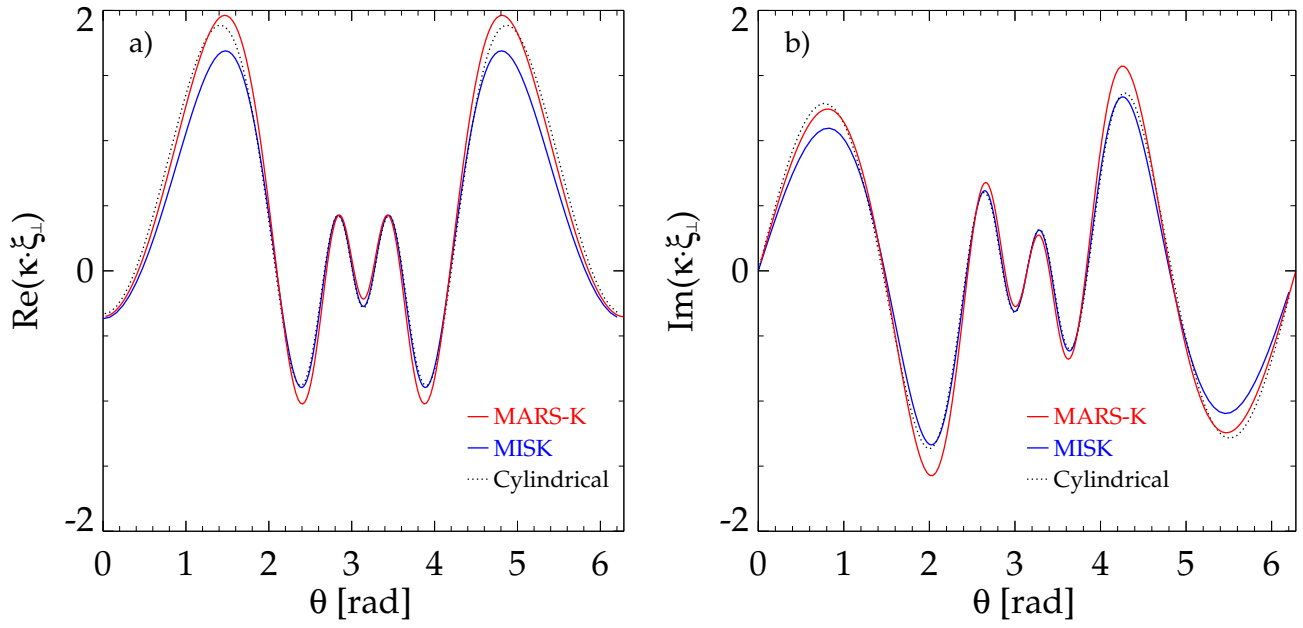

FIG. 39. a) Real and b) imaginary components of $\kappa \cdot \xi_\perp$ vs. θ in the Solov'ev 3 equilibrium at $\Psi_n = 0.9$, calculated by `MISK` and `MARS-K`. The `MARS-K` results are renormalized by making the maximum value on the $\Psi_n = 0.585$ surface the same as the `MISK` maximum.

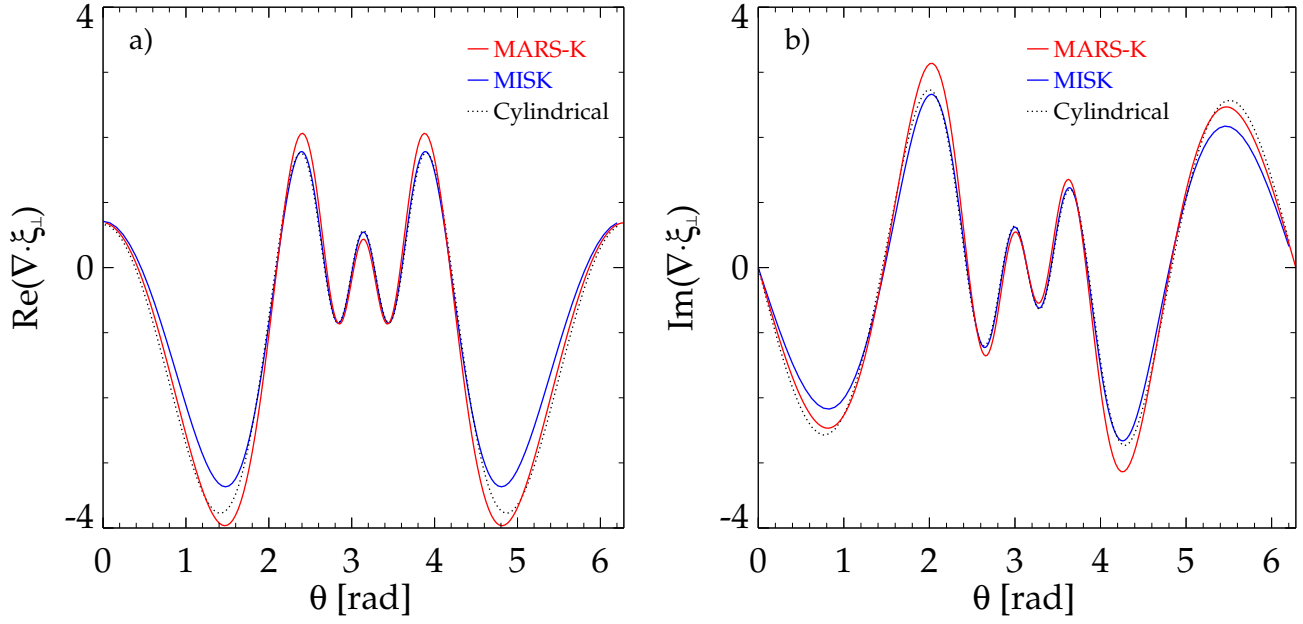

FIG. 40. a) Real and b) imaginary components of $\nabla \cdot \xi_\perp$ vs. θ in the Solov'ev 3 equilibrium at $\Psi_n = 0.9$, calculated by `MISK` and `MARS-K`. The `MARS-K` results are renormalized by making the maximum value on the surface the $\Psi_n = 0.585$ same as the `MISK` maximum.

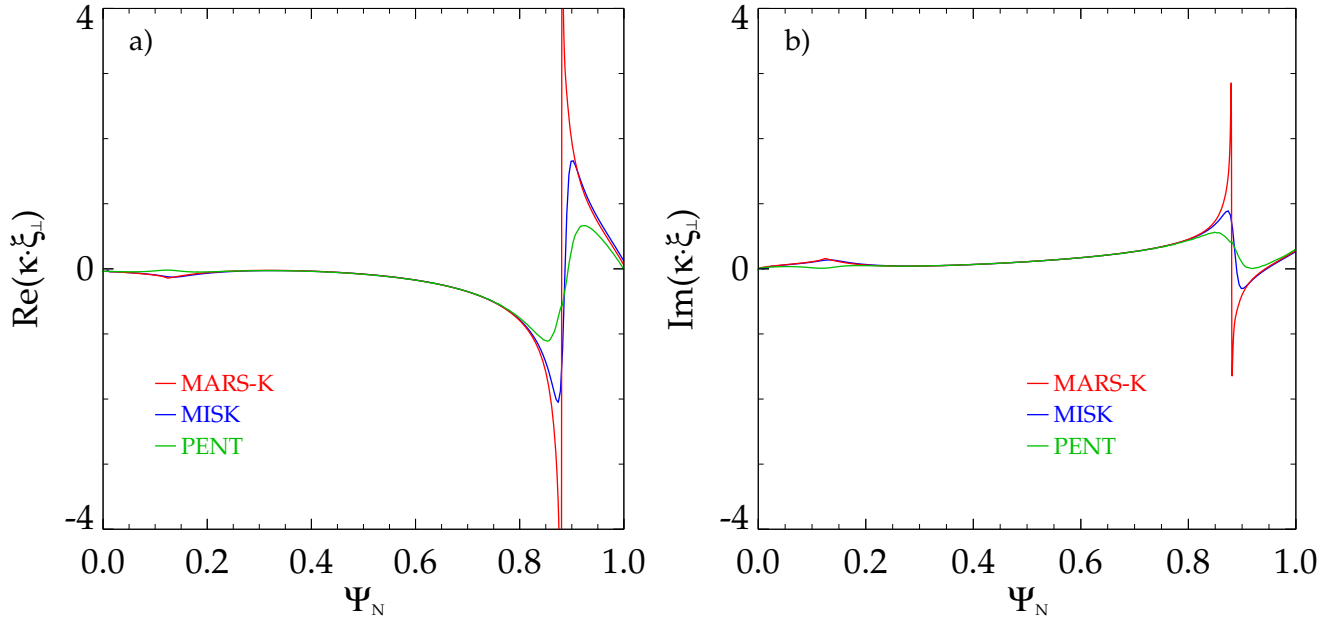

FIG. 41. a) Real and b) imaginary components of $\kappa \cdot \xi_\perp$ vs. Ψ_N in the Solov'ev 3 equilibrium at $\theta = \pi/2$, calculated by `MARS-K`, `MISK`, and `PENT`. The `MARS-K` results are renormalized by making the maximum value on the $\Psi_n = 0.585$ surface the same as the `MISK` maximum. The `PENT` results are renormalized by making the value on the $\Psi_n = 0.585$ surface at this θ $(\pi/2)$ the same as the `MISK` value.

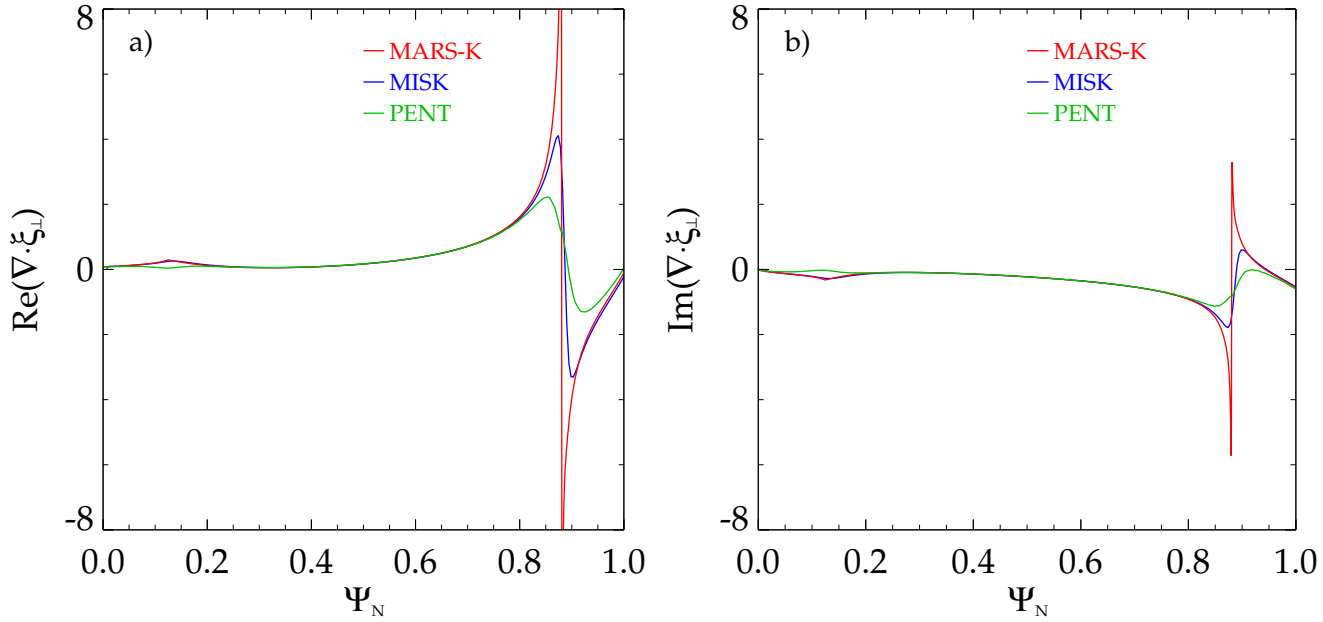

FIG. 42. a) Real and b) imaginary components of $\nabla \cdot \xi_\perp$ vs. Ψ_N in the Solov'ev 3 equilibrium at $\theta = \pi/2$, calculated by `MARS-K`, `MISK`, and `PENT`. The `MARS-K` results are renormalized by making the maximum value on the $\Psi_n = 0.585$ surface the same as the `MISK` maximum. The `PENT` results are renormalized by making the value on the $\Psi_n = 0.585$ surface at this θ $(\pi/2)$ the same as the `MISK` value.

VIII. FLUID δW TERMS

δW_∞ and δW_b are the fluid terms calculated with the wall at infinity or the actual "experimental" location b. In this study we will use a conformal wall, so that b is the distance of the wall away from the plasma boundary, in units of r/a, and the normalized wall position is $r_w/a = 1 + b$. The absolute value of these δW quantities as calculated by different codes is arbitrary; what really matters are the ratios. Therefore in this section we will report the quantity $\hat{\gamma}_f^{-1} = -\delta W_b/\delta W_\infty$, which is the inverse fluid growth rate, normalized by the wall time.

Let us now also define $\delta W_\infty = \delta W_F + \delta W_S + \delta W_V^\infty$, the sum of the plasma fluid, surface, and vacuum perturbed potential energies when the wall is placed at infinity, and $\delta W_b = \delta W_F + \delta W_S + \delta W_V^b$, the sum of the plasma fluid, surface, and vacuum δW terms when the wall is placed at a specific location b. The `PEST` code uses the `VACUUM` code[63] to calculate the δW_V terms. The plasma fluid terms are equal regardless of the wall position. The surface term arises when there is a finite pressure gradient at the plasma boundary. In the Solov'ev cases there is a gradient at the boundary, however the surface term is neglected for the purpose of this benchmarking exercise.

Once δW_∞ is found, δW_b, and therefore $\hat{\gamma}_f^{-1}$, can be examined as a function of r_w/a. This is shown for the three cases in Fig. 43a for the ideal kink mode and can be directly compared to Ref. [14], Fig. 3, for the Solov'ev 1 case. Here we will instead use the eigenfunction for the marginally stable ideal kink mode with an ideal wall in `PEST` and `DCON` (approximating the fluid RWM) and the fluid RWM in `MARS-K`. Figure 43b shows $\hat{\gamma}_f^{-1}$ vs. r_w/a for these cases.

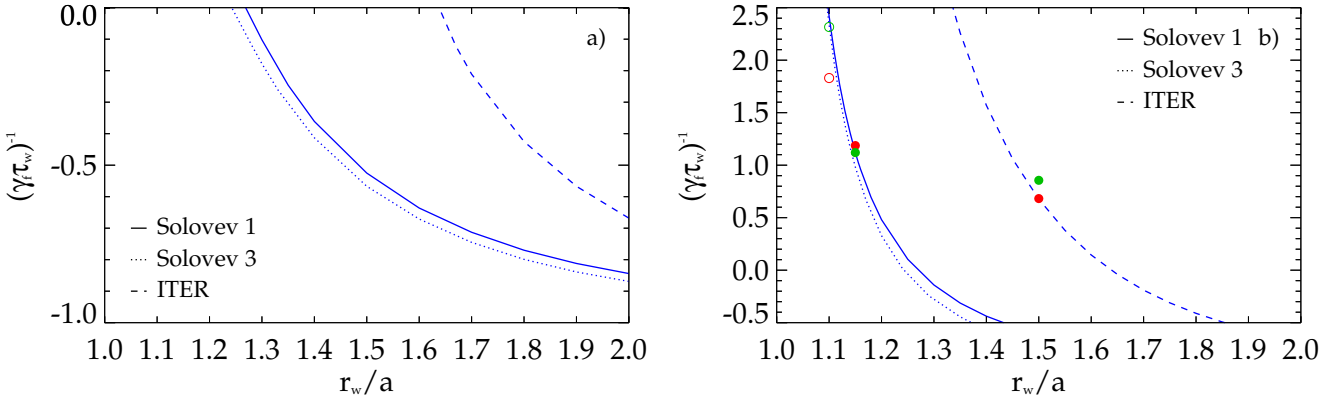

FIG. 43. The inverse fluid growth rate, normalized by the wall time, vs. normalized conformal wall position for the three cases for: a) the ideal kink, and b) the marginally stable ideal kink mode with an ideal wall (`PEST`, `DCON`) or the fluid RWM (`MARS-K`). `PEST` results are shown in blue, `MARS-K` results in red, and `DCON` results in green. The circle markers shown in b) indicate the values at the wall positions chosen for comparison.

For the Solov'ev 1 case we choose conformal walls with $r_w/a = 1.15$, and for Solov'ev 3 $r_w/a = 1.10$ (see Fig. 2), to be consistent with Ref. [14]. For the ITER case, we choose a conformal wall with $r_w/a = 1.5$, which approximates the actual ITER wall. See Fig. 4 for illustrations of these walls. In `PEST` the fluid δW quantities have a dependency on the selection of $\Psi_{\rm lim}$. For the Solov'ev cases $\Psi_{\rm lim} = 1$ can be used, but for the ITER case here we have used $\Psi_{\rm lim} = 0.9976$, which results in $q_{\rm edge} = 6.96168$. The results are given in Table III.

Note that $\hat{\gamma}_f$ is slightly lower for `MARS-K` than `PEST` or `DCON` in the Solov'ev 1 case, and slightly higher in the Solov'ev 3 case. This will impact the kinetic growth rate, as will be seen in section X. For the ITER case `DCON` finds a lower $\hat{\gamma}_f$, due to a lower δW_∞. However, this difference also impacts the normalization of the kinetic effects in `PENT` so that in the end the ITER kinetic $\gamma\tau_w$ for `PENT` will be close to that of `MARS-K` and `MISK`.

	r_w/a	$\delta W_F/(-\delta W_\infty)$	$\delta W_V^b/(-\delta W_\infty)$	$\hat{\gamma}_f^{-1} = \delta W_b/(-\delta W_\infty)$
Solov'ev 1	1.15	-1.814	3.001	1.187
		-1.793	2.915	1.122
		-1.792	2.912	1.120
Solov'ev 3	1.10	-2.257	4.087	1.830
		-2.210	4.547	2.337
		-2.202	4.519	2.316
ITER	1.50	-6.284	6.966	0.682
				0.677
		-8.844	9.700	0.856

TABLE III. `MARS-K` results are red, `PEST` results are blue, and `DCON` results are green. $\delta W_V^\infty/(-\delta W_\infty)$ can be inferred from $1 + \delta W_F/(-\delta W_\infty)$.

IX. KINETIC δW_K

For trapped Maxwellian particles, the kinetic δW is given by

$$\delta W_K = -\frac{\sqrt{\pi}}{2}\int_0^{\Psi_a}\frac{nT}{B_0}\int_{B_0/B_{\max}}^{B_0/B_{\min}}\tau\sum_l|\langle H/\hat{\varepsilon}\rangle|^2 I_{\hat{\varepsilon}}d\Lambda d\Psi, \tag{54}$$

where one can see that δW_K involves the previously defined quantities $I_{\hat{\varepsilon}}$ and $\langle H/\hat{\varepsilon}\rangle$ in a straightforward way.

Once again, the absolute value of δW_K is meaningless, so we will report the values found as $-\delta W_K/\delta W_\infty$, broken into its various contributions in Table IV and Figs. 44 and 45 for Solov'ev 1 and Figs. 47 and 48 for Solov'ev 3. Figures 46 and 49 show the $l = 0$ ions and electrons added together for the Solov'ev 1 and 3 cases, respectively. There is a large cancelation between the two, so notice that the scales are smaller than in Figs. 44 and 47, respectively. Finally, Figs. 50, 51, and 52 are the same plots, for the ITER case.

Generally, and as expected, one can see that the kinetic resonance between the mode and the precession motion of particles is strongest when the plasma rotation is small ($\omega_{E0}/\omega_{A0} \lesssim 0.1$), while the resonance with the bounce motion of trapped particles or circulating motion of passing particles is strongest at higher rotation ($\omega_{E0}/\omega_{A0} \gtrsim 0.1$). The codes agree well in the calculation of each term, especially for the precession resonance and especially for the Solov'ev 1 case, which has no rational surfaces. The rational surfaces are integrated over in the Solov'ev 3 case for each code. This is historically how `PENT` (with smoothed rational contribution) and `MARS-K` (unsmoothed) have been operated; `MISK` was operated like `MARS-K` in this case. This leads to the discrepancy between the codes in the bounce and circulating terms seen in Fig. 48, as we will discuss in Sec. IX C. Finally, in the ITER case singular Alfvén resonances at the rationals have been removed for both `MARS-K` and `MISK`, and this leads to good agreement between each code in each term. This is how `MISK` has historically been operated (although the analytical replacement of the rational surface contribution normally calculated by `MISK`[20] was not included here); `MARS-K` was operated like `MISK` in this case. The `PENT` results are somewhat higher in magnitude in Figs. 50-51, due the lower δW_∞ normalization factor. We have seen that this difference also affects the fluid growth rate, however, making γ_f^{-1} higher as well. Therefore the growth rate from `PENT` will be consistent with that of `MISK` and `MARS-K` in the end.

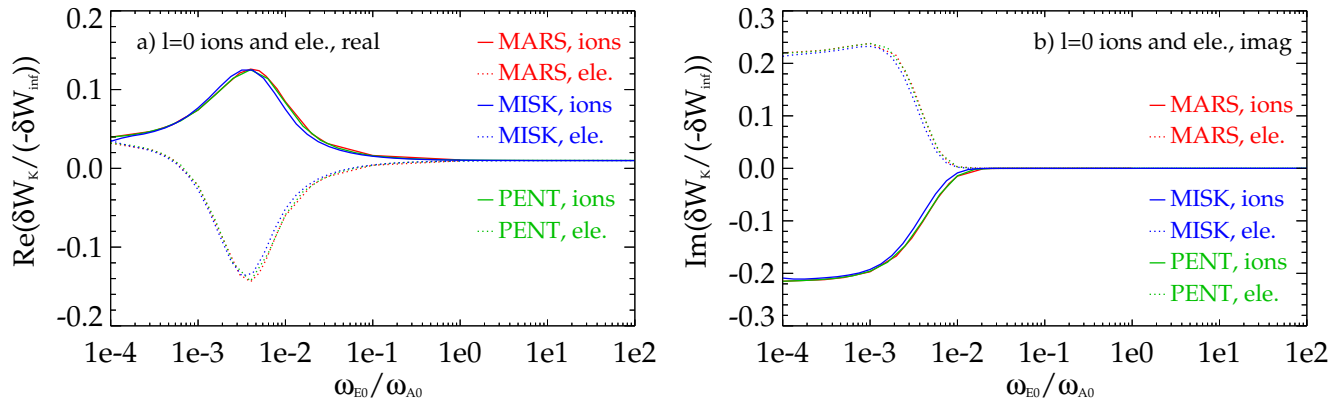

FIG. 44. a) Real and b) imaginary δW_K for $l = 0$ trapped thermal ions and electrons for the Solov'ev 1 case.

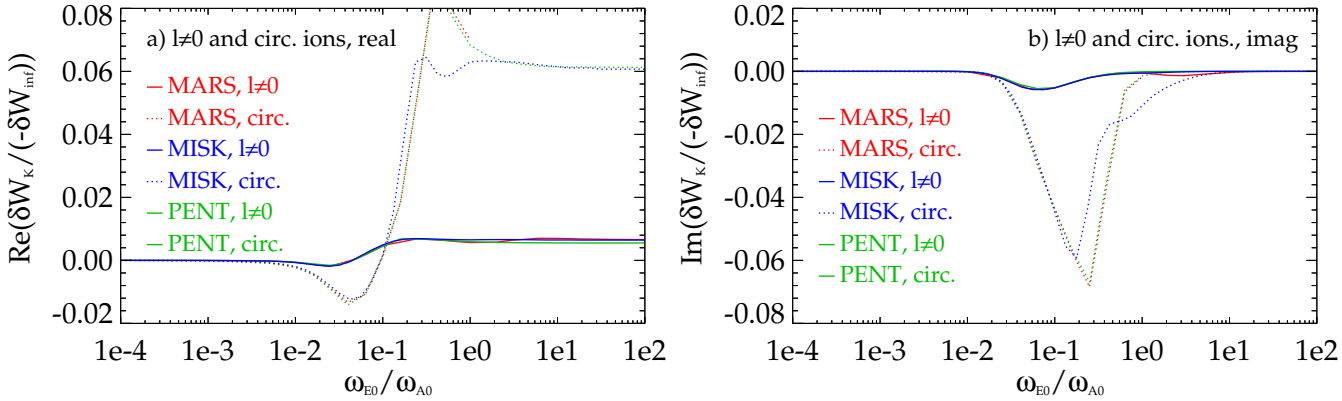

FIG. 45. a) Real and b) imaginary δW_K for $l \neq 0$ trapped thermal ions and for circulating ions for the Solov'ev 1 case.

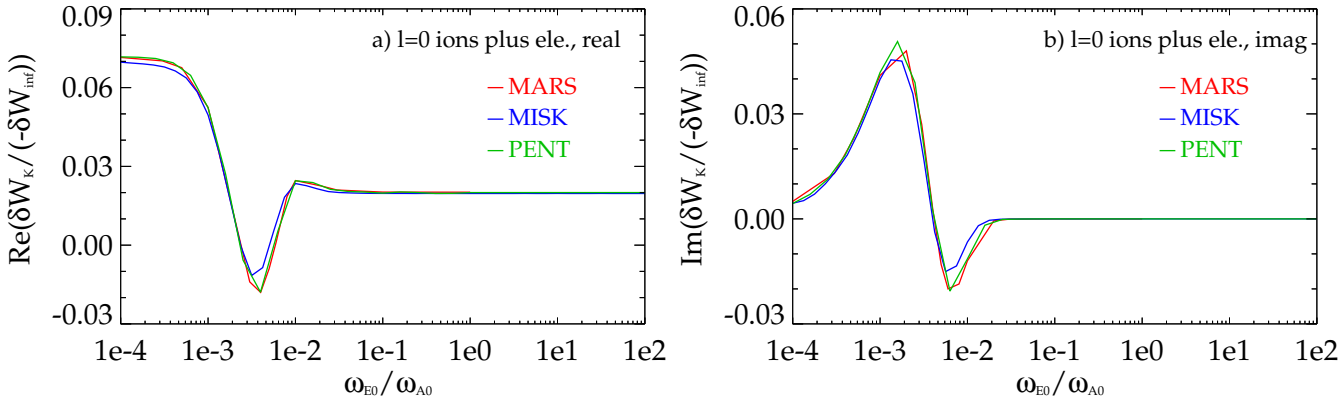

FIG. 46. a) Real and b) imaginary δW_K for $l = 0$ trapped thermal ions and electrons *together* for the Solov'ev 1 case.

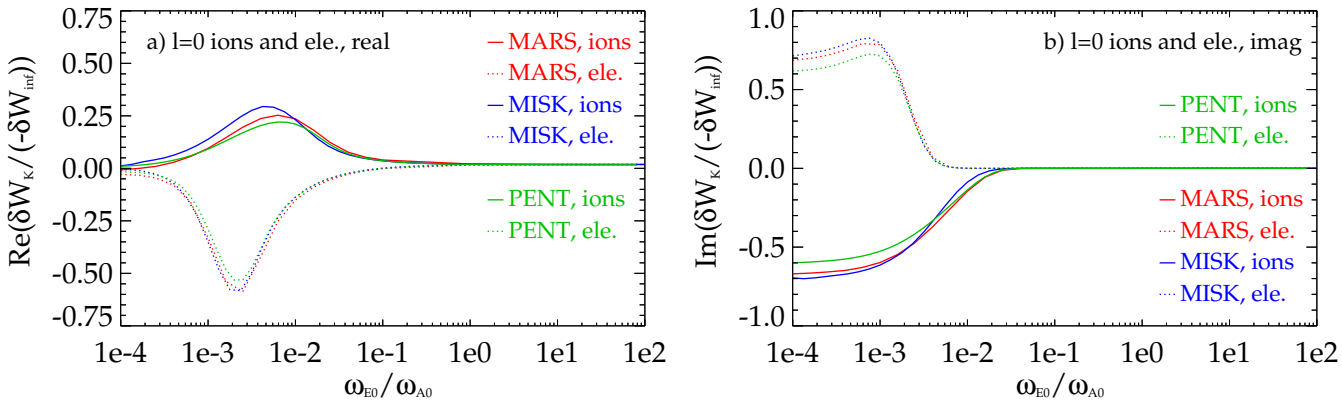

FIG. 47. a) Real and b) imaginary δW_K for $l = 0$ trapped thermal ions and electrons for the Solov'ev 3 case.

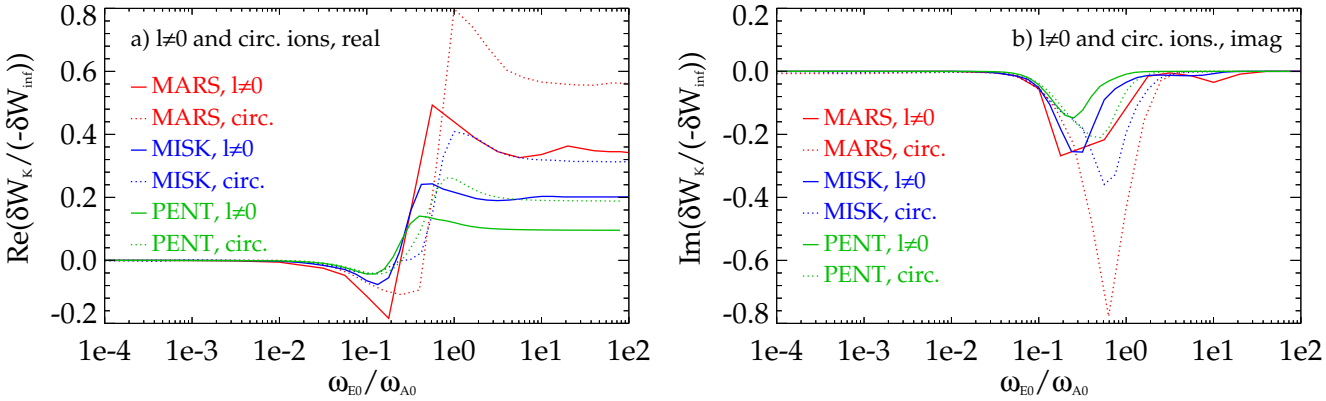

FIG. 48. a) Real and b) imaginary δW_K for $l \neq 0$ trapped thermal ions and for circulating ions for the Solov'ev 3 case.

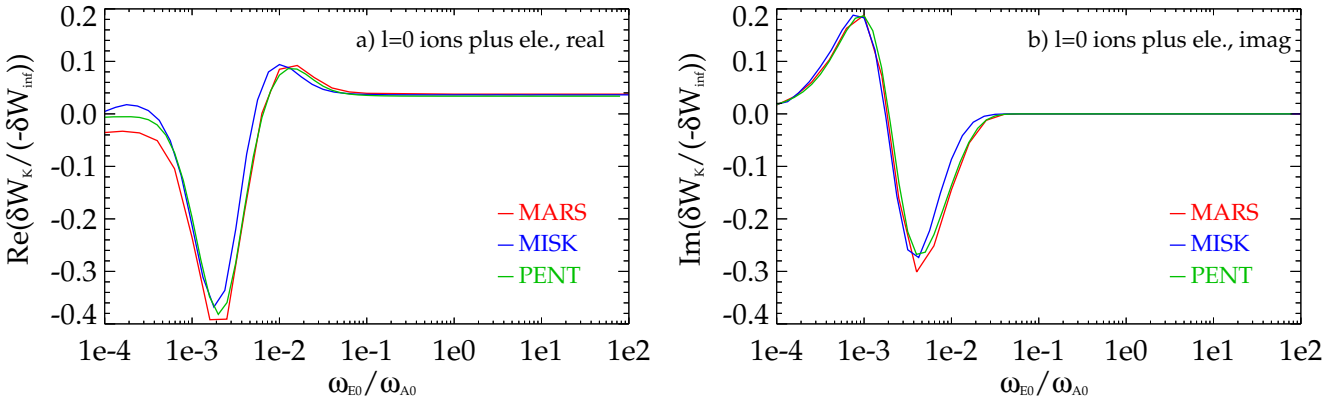

FIG. 49. a) Real and b) imaginary δW_K for $l = 0$ trapped thermal ions and electrons *together* for the Solov'ev 3 case.

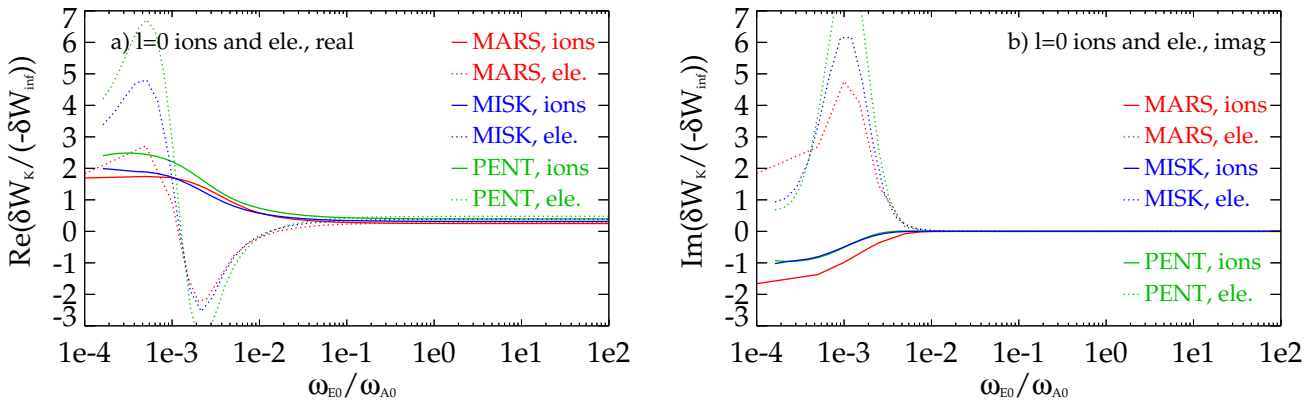

FIG. 50. a) Real and b) imaginary δW_K for $l = 0$ trapped thermal ions and electrons for the ITER case.

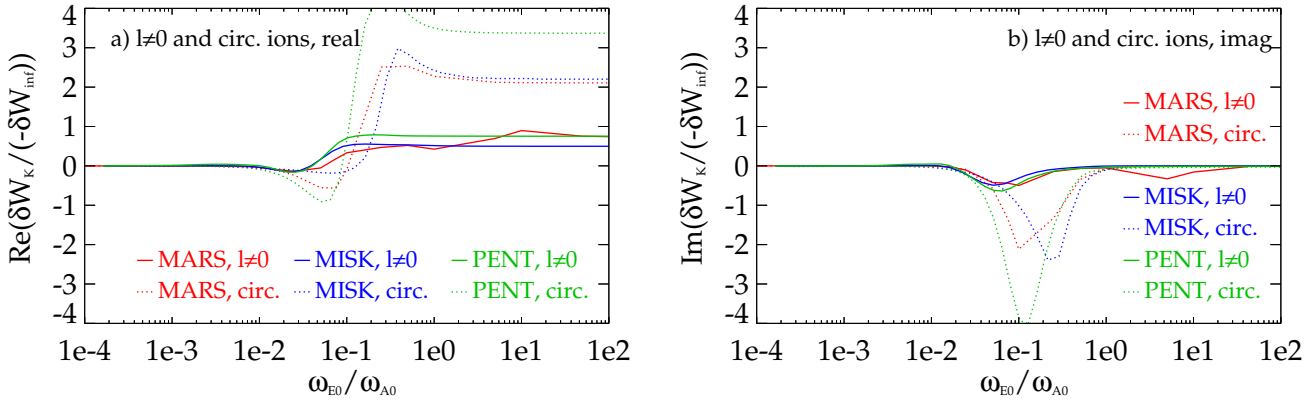

FIG. 51. a) Real and b) imaginary δW_K for $l \neq 0$ trapped thermal ions and for circulating ions for the ITER case.

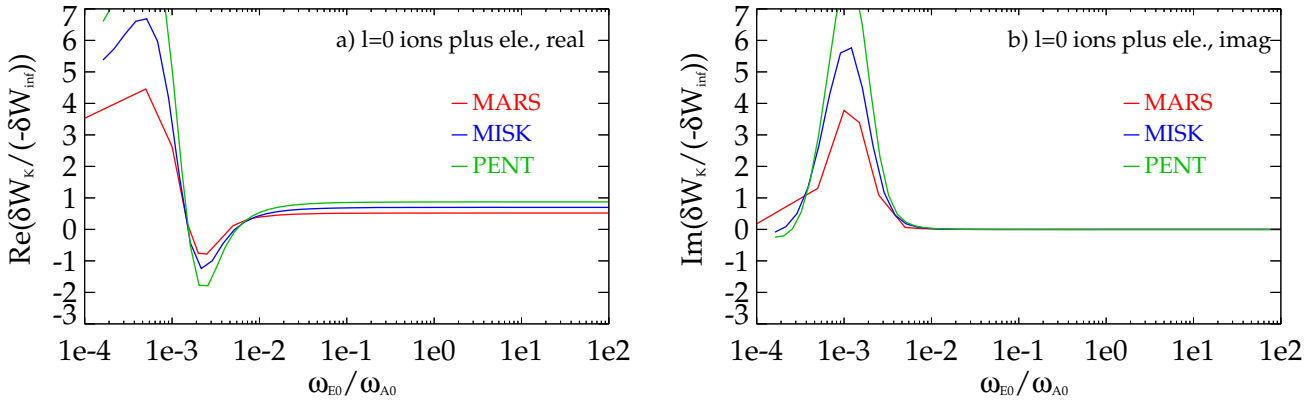

FIG. 52. a) Real and b) imaginary δW_K for $l = 0$ trapped thermal ions and electrons *together* for the ITER case.

	thermal ions						thermal electrons		Total	
	trapped				circulating		trapped ($l = 0$ only)			
	$l = 0$		$l \neq 0$							
	real	imag	real	imag	real	imag	real	imag	real	imag
Solov'ev 1	8.46×10^{-2}	-1.49×10^{-2}	-6.53×10^{-4}	-9.13×10^{-5}	-2.10×10^{-3}	-1.33×10^{-4}	-6.00×10^{-2}	2.94×10^{-3}	2.18×10^{-2}	-1.21×10^{-2}
	7.49×10^{-2}	-8.68×10^{-3}	-6.89×10^{-4}	-1.17×10^{-4}	-1.94×10^{-3}	-1.09×10^{-4}	-5.14×10^{-2}	2.09×10^{-3}	2.08×10^{-2}	-6.82×10^{-3}
	8.23×10^{-2}	-1.40×10^{-2}	-5.54×10^{-4}	-6.09×10^{-5}	-2.21×10^{-3}	-9.12×10^{-5}	-5.81×10^{-2}	2.72×10^{-3}	2.14×10^{-2}	-1.14×10^{-2}
Solov'ev 3	2.36×10^{-1}	-1.45×10^{-1}	-5.73×10^{-3}	-1.78×10^{-5}	1.00×10^{-4}	-2.97×10^{-3}	-1.51×10^{-1}	5.50×10^{-4}	7.94×10^{-2}	-1.47×10^{-1}
	2.31×10^{-1}	-8.72×10^{-2}	-3.13×10^{-3}	-1.90×10^{-5}	-1.70×10^{-3}	-2.98×10^{-3}	-1.37×10^{-1}	6.12×10^{-4}	8.92×10^{-2}	-8.96×10^{-2}
	2.11×10^{-1}	-1.37×10^{-1}	-1.84×10^{-3}	-1.47×10^{-5}	-8.81×10^{-4}	-2.21×10^{-3}	-1.37×10^{-1}	4.47×10^{-4}	7.13×10^{-2}	-1.39×10^{-1}
ITER	4.54×10^{-1}	-1.08×10^{-3}	-9.37×10^{-2}	-2.32×10^{-2}	-1.20×10^{-1}	-2.57×10^{-2}	-1.04×10^{-3}	4.37×10^{-3}	2.41×10^{-1}	-4.56×10^{-2}
	4.82×10^{-1}	-3.97×10^{-4}	-1.13×10^{-1}	-4.34×10^{-2}	-8.46×10^{-2}	-9.62×10^{-2}	8.28×10^{-2}	6.96×10^{-3}	3.67×10^{-1}	-1.33×10^{-1}
	6.15×10^{-1}	2.70×10^{-3}	-1.02×10^{-1}	7.36×10^{-3}	-2.12×10^{-1}	-8.86×10^{-2}	8.57×10^{-2}	6.25×10^{-3}	3.87×10^{-1}	-7.23×10^{-2}

TABLE IV. $\delta W_K/(-\delta W_\infty)$. `MARS-K` results are red, `MISK` results are blue, and `PENT` results are green. For the Solov'ev 1 and 2 cases the nominal value of $\omega_{e0}/\omega_{A0} = 1 \times 10^{-2}$ is used. For the ITER case, the nominal value of $\omega_{e0}/\omega_{A0} = 1.62 \times 10^{-2}$ is used, and surfaces within $\Delta q = \pm 0.1$ of all rational surfaces are excluded.

A. The CGL Limit

There are three separate possible ways to calculate δW in the CGL, or high-frequency limit ($|\omega_E - \omega| \to \infty$). The first is to just increase ω_E to a large value in the codes, as is effectively accomplished in Figs. 44, 45, 47, and 48 on the right hand side when $\omega_{E0}/w_{A0} = 100$. The total fluid δW_{CGL} is found by adding the various components in this limit. In this case circulating electrons and trapped electrons with a bounce ($l \neq 0$) resonance become important, so they are included as well. The second method is to add the various components while taking the analytical limit $I_\varepsilon = 15\sqrt{\pi}/8$ described in subsection V A 1. The third method is to solve for δW_{CGL} directly using the CGL perturbed pressures[36]:

$$\delta W_{CGL} = \frac{1}{2}\int \frac{5}{3} p \left|\boldsymbol{\nabla}\cdot\boldsymbol{\xi}_\perp\right|^2 dV + \frac{1}{2}\int \frac{1}{3} p \left|\boldsymbol{\nabla}\cdot\boldsymbol{\xi}_\perp + 3\boldsymbol{\kappa}\cdot\boldsymbol{\xi}_\perp\right|^2 dV, \tag{55}$$

and then use the pressure and the quantities $\boldsymbol{\nabla}\cdot\boldsymbol{\xi}_\perp$ and $\boldsymbol{\kappa}\cdot\boldsymbol{\xi}_\perp$ from section VII to calculate the fluid δW_{CGL} directly. The relevant terms from the above equation are shown for the Solov'ev 3 case in Figs. 53 and 54. The results of these three methods are given in Table V for each case. Again, the differences between codes in the Solov'ev 3 case are due to integration over the rational surfaces.

	$\omega_{E0}/\omega_{A0} = 100$	$I_\varepsilon = 15\sqrt{\pi}/8$	Fluid δW_{CGL}
Solov'ev 1	1.57×10^{-1} 1.54×10^{-1} 1.55×10^{-1}	1.54×10^{-1}	1.57×10^{-1} 1.56×10^{-1}
Solov'ev 3	1.98×10^{0} 1.09×10^{0} 6.31×10^{-1}	1.07×10^{0}	1.84×10^{0} 1.01×10^{0}
ITER	6.11×10^{0} 6.72×10^{0} 9.89×10^{0}	6.67×10^{0}	6.55×10^{0} 6.53×10^{0}

TABLE V. $\delta W_K/(-\delta W_\infty)$ in the CGL limit ($|\omega_E - \omega| \to \infty$). `MARS-K` results are red, `MISK` results are blue, and `PENT` results are green. All values are real. For the ITER case surfaces within $\Delta q = \pm 0.1$ of all rational surfaces are excluded for `MARS-K` and `MISK`.

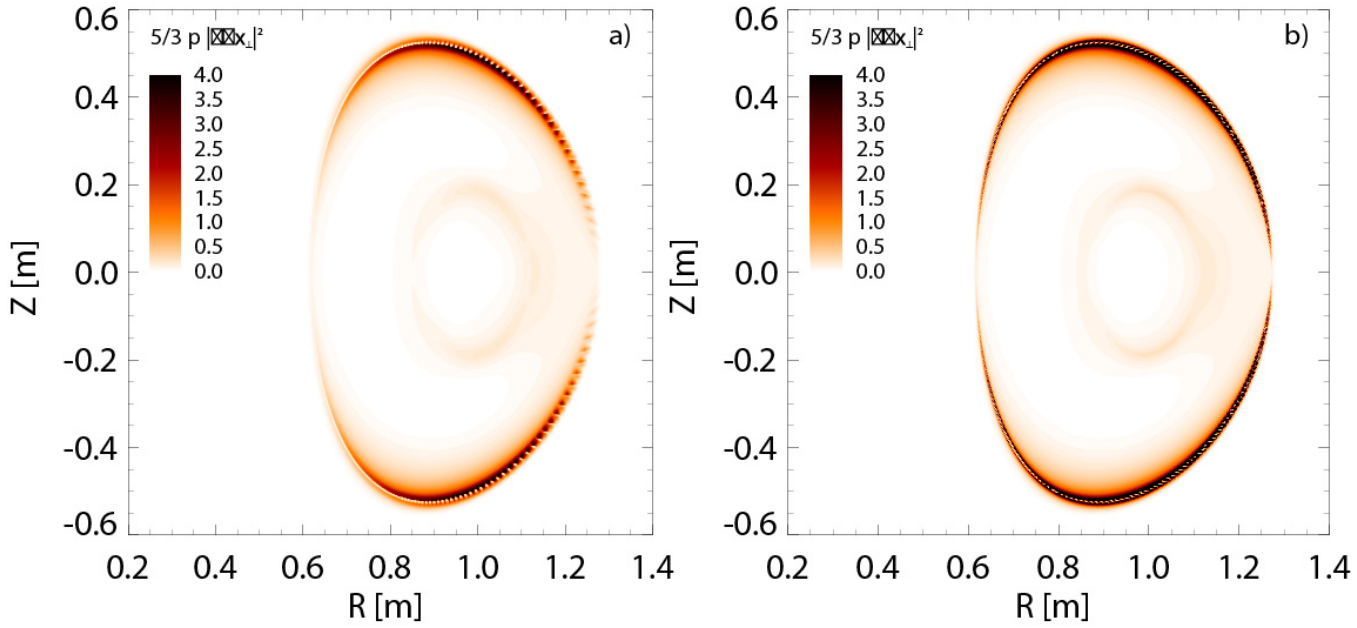

FIG. 53. $\frac{5}{3}p|\nabla\cdot\xi_\perp|^2$ (arbitrary units) in the Solov'ev 3 equilibrium (for use in δW_{CGL}), calculated by a) `MISK` and b) `MARS-K`. The `MARS-K` results are renormalized by making the maximum value at $r/R_0 = 0.252$ ($\Psi_n = 0.585, q = 2.5$) the same as the `MISK` maximum.

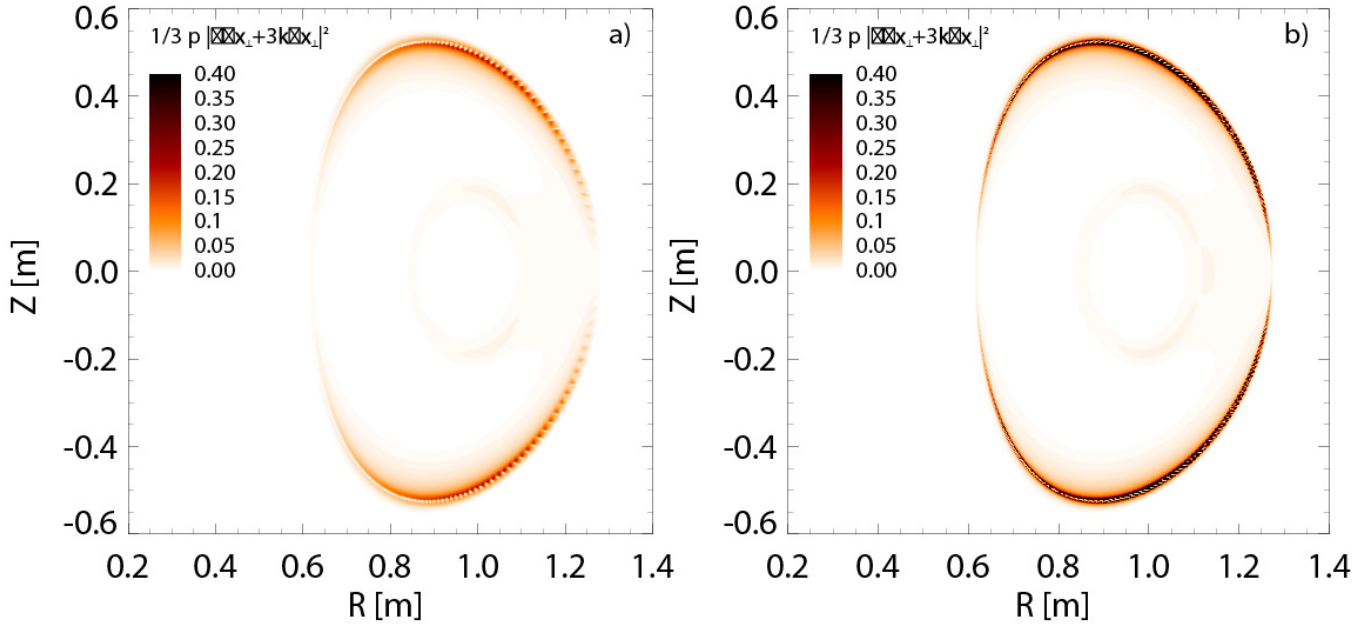

FIG. 54. $\frac{1}{3}p|\nabla\cdot\xi_\perp + 3\kappa\cdot\xi_\perp|^2$ (arbitrary units) in the Solov'ev 3 equilibrium (for use in δW_{CGL}), calculated by a) `MISK` and b) `MARS-K`. The `MARS-K` results are renormalized by making the maximum value at $r/R_0 = 0.252$ ($\Psi_n = 0.585, q = 2.5$) the same as the `MISK` maximum.

B. Convergence vs. Damping Parameter

A damping parameter in the denominator of the resonance operator can come either from the finite growth rate of the RWM (γ), or from collisonality (ν_{eff}). δW_K should converge to the same value as that of the "ideal" case without any damping, when these damping terms approach zero. Figures 55-58 show the results of such a convergence study for the Solov'ev 1 case for the $l = 0$ trapped ion and electron terms, the $l \neq 0$ trapped ion term, and the circulating ion term. These cases show how both `MARS-K` and `MISK` converge as damping goes to zero (as is the case throughout the rest of this document) and also that the codes give similar results with increased damping.

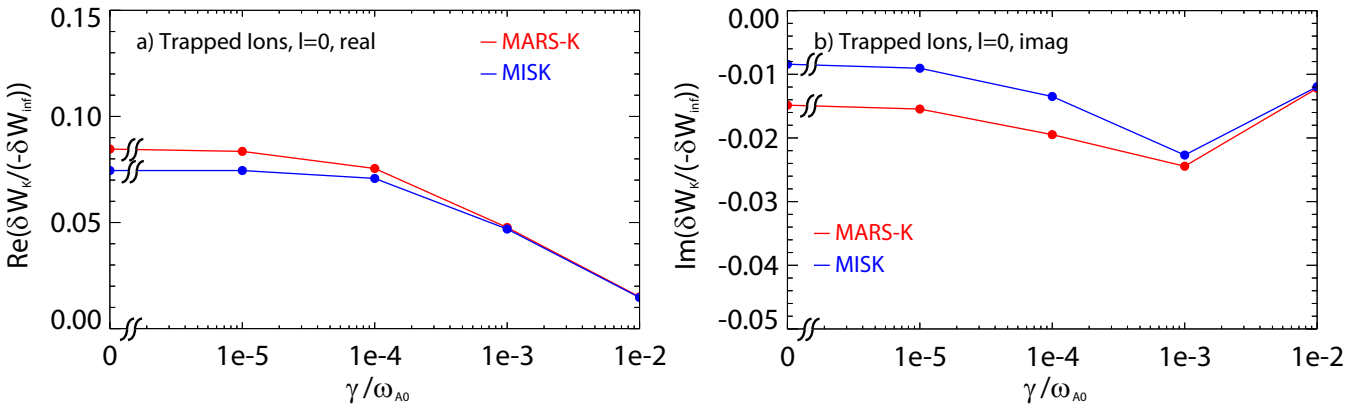

FIG. 55. Convergence of a) $Re(\delta W_K)$ and b) $Im(\delta W_K)$ for trapped thermal ions with $l = 0$ versus damping for the Solov'ev 1 case, as calculated by `MARS-K` and `MISK`.

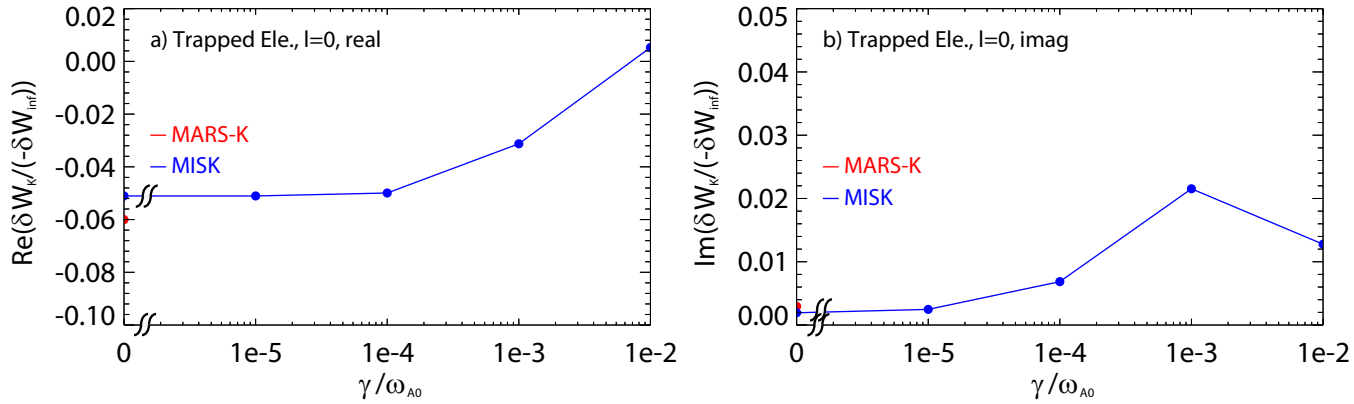

FIG. 56. Convergence of a) $Re(\delta W_K)$ and b) $Im(\delta W_K)$ for trapped thermal electrons with $l = 0$ versus damping for the Solov'ev 1 case, as calculated by `MARS-K` and `MISK`.

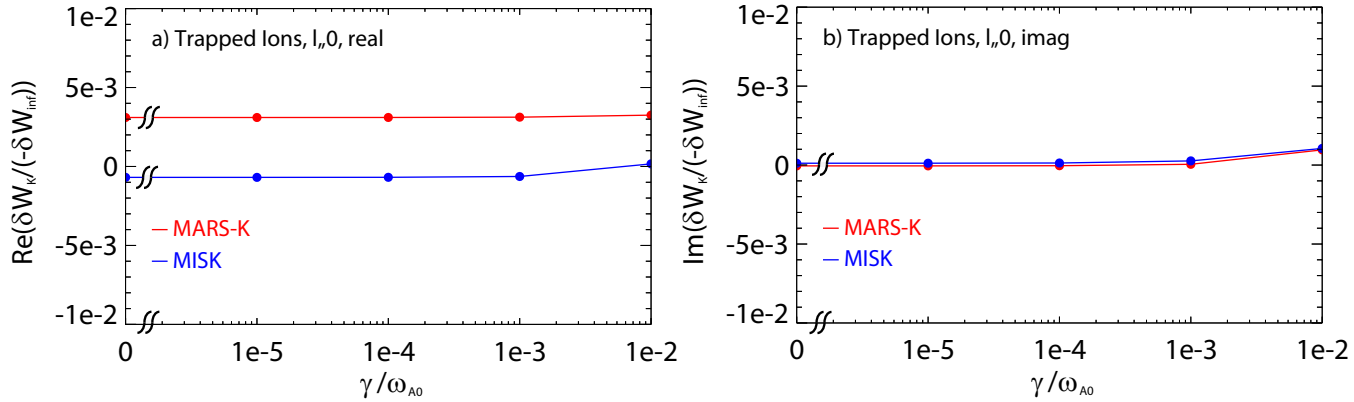

FIG. 57. Convergence of a) $Re(\delta W_K)$ and b) $Im(\delta W_K)$ for trapped thermal ions with $l \neq 0$ versus damping for the Solov'ev 1 case, as calculated by `MARS-K` and `MISK`.

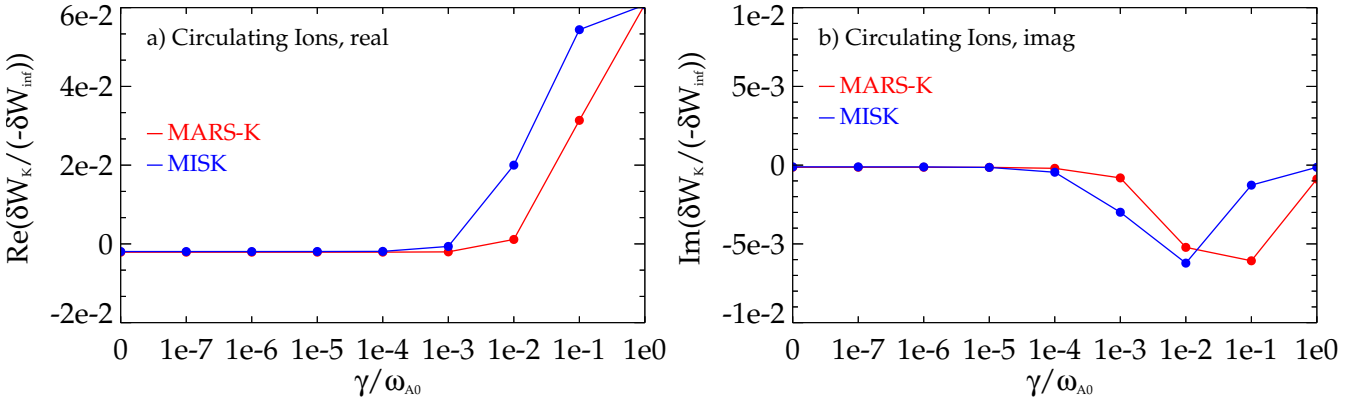

FIG. 58. Convergence of a) $Re(\delta W_K)$ and b) $Im(\delta W_K)$ for circulating ions versus damping for the Solov'ev 1 case, as calculated by `MARS-K` and `MISK`.

C. Contribution to δW_K as a Function of Ψ

One can gain understanding of the importance of the core and edge regions, as well as rational surfaces, by examining the contribution to δW_K as a function of Ψ. Figures 59, 60, and 61 show $Re(d(\delta W_K/(-\delta W_\infty))/d\Psi)$ vs. Ψ in the Solov'ev 1 case for $l = 0$ trapped thermal ions, $l \neq 0$ trapped thermal ions, and circulating ions, respectively. Figures 62, 63, and 64 show the same quantities for the Solov'ev 3 case and Figs. 65, 66, and 67 for ITER. In each case, part a) is for the nominal rotation level, while part b) is at the CGL limit. The integrals of these curves represent the values $Re(\delta W_K/(-\delta W_\infty))$ (which are given in Table IV).

One can see that there is generally very good agreement between the codes for the Solov'ev 1 case, as expected because the results in Figs. 44-46 agreed very well as well. For the Solov'ev 3 case, it becomes clear that the differences that were seen in the results in Fig. 48 are arising almost exclusively from the difference in the codes' calculations at the $q = 3$ rational surface. No special treatment of the rational surfaces was performed for the Solov'ev 3 case (they were simply integrated through), and in spite of this disagreement, the final calculated δW_K values (and $\gamma\tau_w$, as will be seen in the next section) are not so unreasonably different. Finally, however, in Figs. 66 and 67 for the ITER case, it is clear that the rational surface contributions are not only very different between the codes, but unreasonably large for `MISK` and `MARS-K`. This is a well-known issue where singularities arise at the rational surfaces due to Alfvén resonances, and it was pointed out years ago[11]. Generally, the treatment of this issue in `MISK` has been to remove the singular rational surface contributions calculated in this way by imposing a layer with width Δq around each rational surface, and then adding a separately calculated analytical Alfvén layer contribution[20]. Note that this separate, analytical calculation was not added here, but $\Delta q = 0.1$ was used for both `MISK` and `MARS-K` in this ITER case. Historically `MARS-K` has included the rational surface singularities in its calculations, which may account for some historical differences between the codes' results, particularly when `MARS-K` was operated in its perturbative mode.

`PENT`, meanwhile, does not have the same kind of singularities at rational surfaces as `MARS-K` and `MISK` (for example in Figs. 66 and 67). However, this is because the underlying `IPEC` calculations of the eigenfunctions are "regularized" in all cases at the rational surfaces with a characteristic width parameter σ such that $\xi \rightarrow \xi(m-nq)^2/((m-nq)^2+\sigma)$, where m and n are the poloidal and toroidal mode numbers, respectively[64]. Essentially this approach smoothes the contribution to δW_K in a given width near the rational surfaces rather than simply removing it when necessary as in the `MISK` approach. One can see the effect of the `IPEC` approach for example in the Solov'ev 3 case (where the σ regularization was employed in `IPEC` but the Δq cut-off was *not* yet employed in `MISK` and `MARS-K`) in Figs. 41 and 42, which leads to the lower values in Figs. 48, 63 and 64. Another kind of singularity *does* appear in `PENT`, however, with the restrictions applied in this benchmarking exercise (zero collisionality and $\omega_D = 0$ when $l \neq 0$). These occur when the denominator of the energy integral goes to zero in the circulating particle case. Here, these type of spikes have been removed from both the ITER and Solov'ev 3 cases in `PENT` by multiplying the profiles by $\delta q^4/(\delta q^4 + 0.01^4)$, where in this case δq is the difference between $q(\Psi)$ and integer values. This type of suppression is typically not applied in `PENT` as it is not necessary when collisionality and ω_D are non-zero.

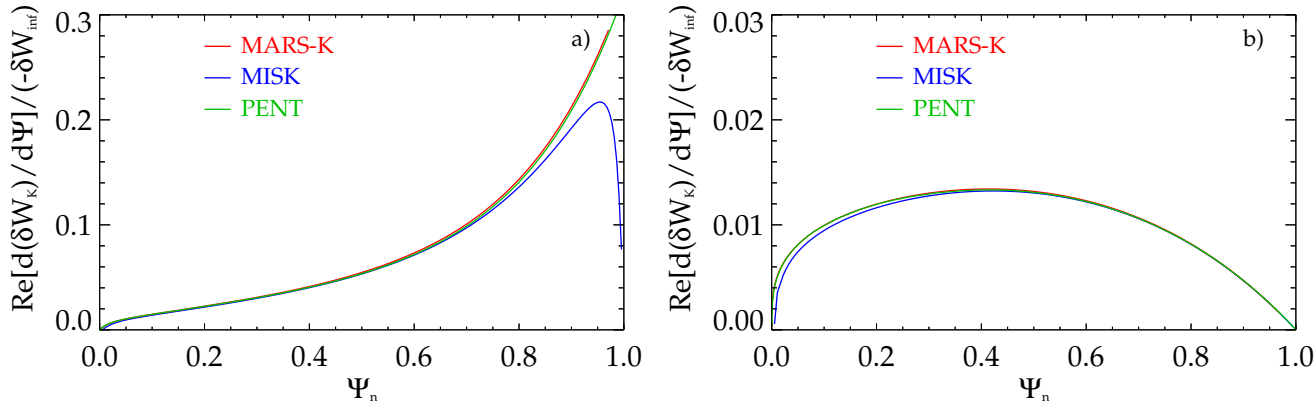

FIG. 59. $Re(d(\delta W_K/(-\delta W_\infty))/d\Psi)$ vs. Ψ for $l = 0$ trapped thermal ions in the Solov'ev 1 case at a) $\omega_{E0}/\omega_{A0} = 1 \times 10^{-2}$, and b) the CGL limit, as calculated by `MARS-K`, `MISK`, and `PENT`.

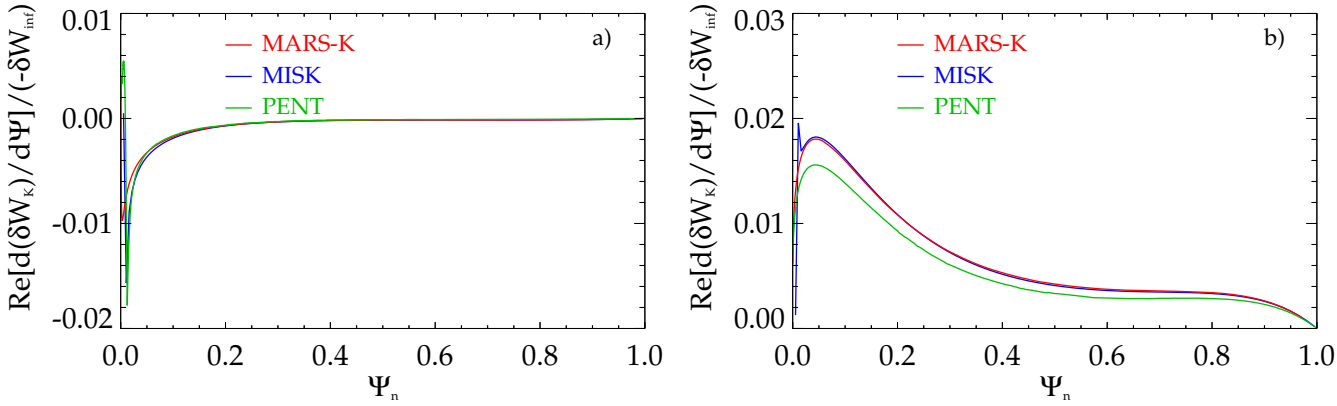

FIG. 60. $Re(d(\delta W_K/(-\delta W_\infty))/d\Psi)$ vs. Ψ for $l \neq 0$ trapped thermal ions in the Solov'ev 1 case at a) $\omega_{E0}/\omega_{A0} = 1 \times 10^{-2}$, and b) the CGL limit, as calculated by `MARS-K`, `MISK`, and `PENT`.

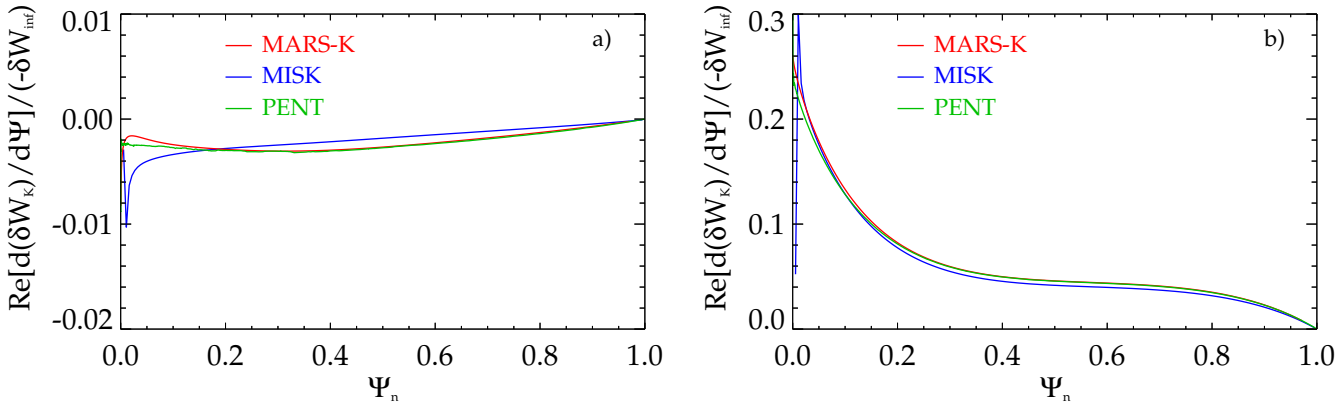

FIG. 61. $Re(d(\delta W_K/(-\delta W_\infty))/d\Psi)$ vs. Ψ for circulating thermal ions in the Solov'ev 1 case at a) $\omega_{E0}/\omega_{A0} = 1 \times 10^{-2}$, and b) the CGL limit, as calculated by `MARS-K`, `MISK`, and `PENT`.

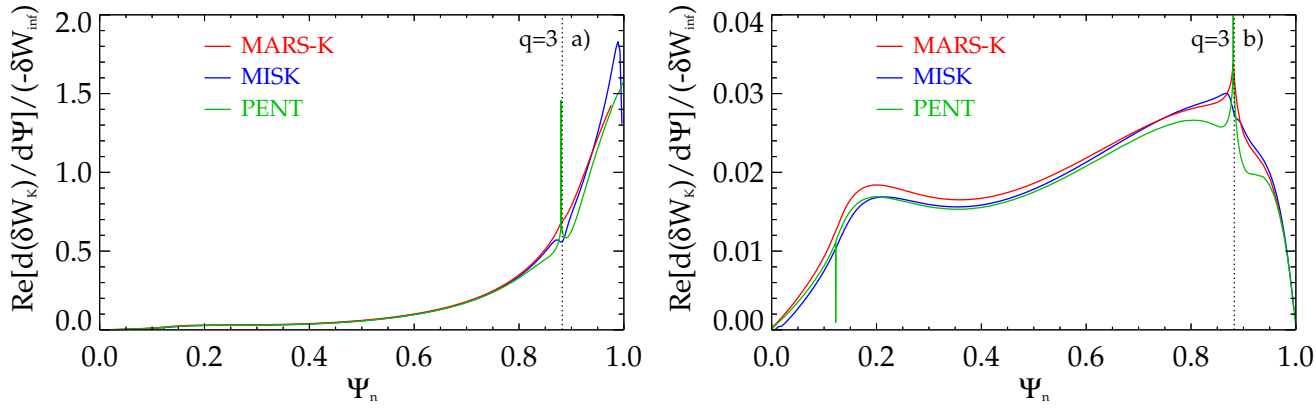

FIG. 62. $Re(d(\delta W_K/(-\delta W_\infty))/d\Psi)$ vs. Ψ for $l = 0$ trapped thermal ions in the Solov'ev 3 case at a) $\omega_{E0}/\omega_{A0} = 1 \times 10^{-2}$, and b) the CGL limit, as calculated by `MARS-K`, `MISK`, and `PENT`.

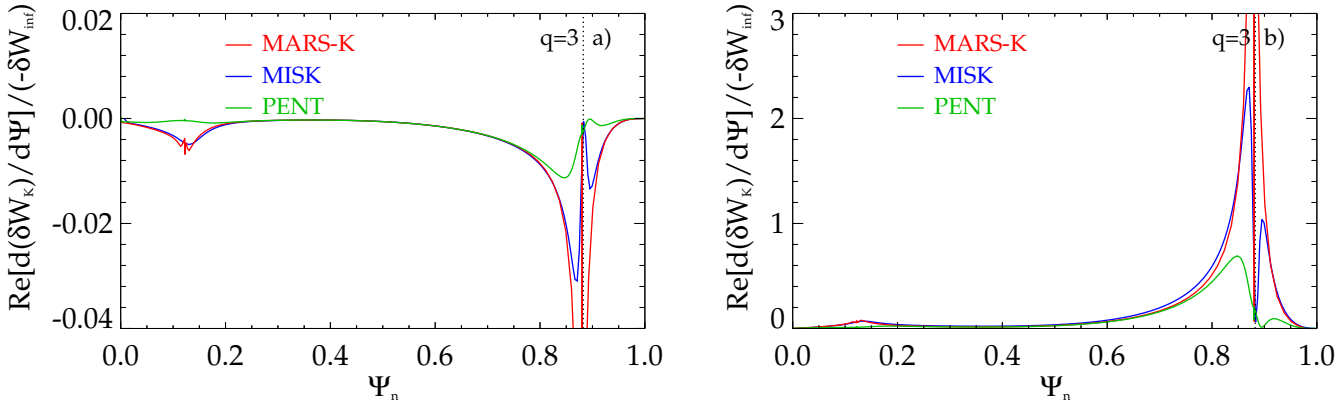

FIG. 63. $Re(d(\delta W_K/(-\delta W_\infty))/d\Psi)$ vs. Ψ for $l \neq 0$ trapped thermal ions in the Solov'ev 3 case at a) $\omega_{E0}/\omega_{A0} = 1 \times 10^{-2}$, and b) the CGL limit, as calculated by `MARS-K`, `MISK`, and `PENT`.

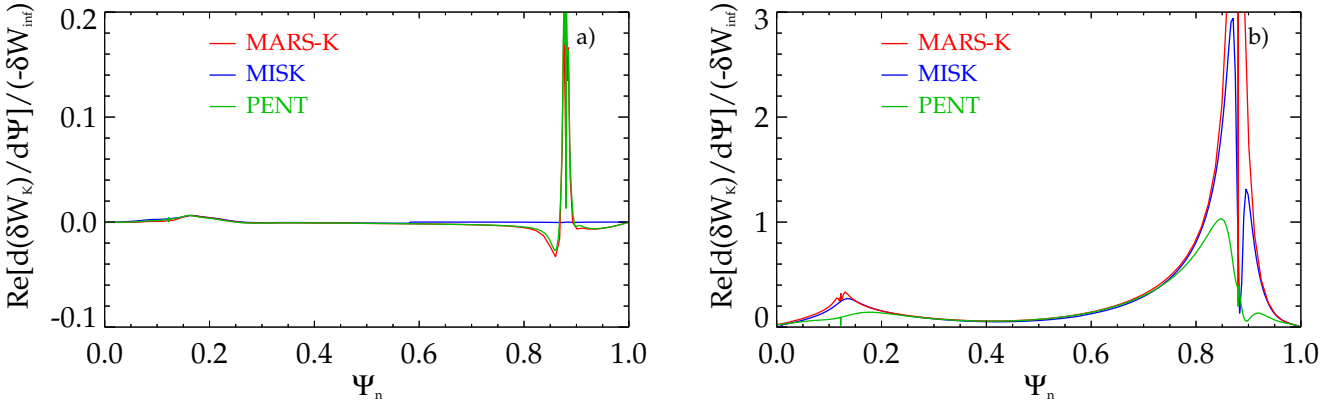

FIG. 64. $Re(d(\delta W_K/(-\delta W_\infty))/d\Psi)$ vs. Ψ for circulating thermal ions in the Solov'ev 3 case at a) $\omega_{E0}/\omega_{A0} = 1 \times 10^{-2}$, and b) the CGL limit, as calculated by `MARS-K`, `MISK`, and `PENT`.

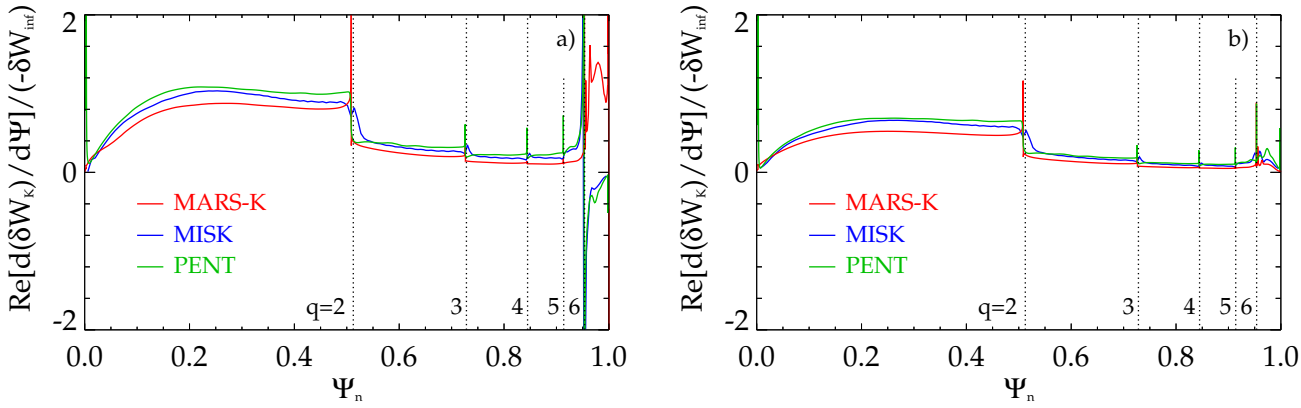

FIG. 65. $Re(d(\delta W_K/(-\delta W_\infty))/d\Psi)$ vs. Ψ for $l = 0$ trapped thermal ions in the ITER case at a) $\omega_{E0}/\omega_{A0} = 1.62 \times 10^{-2}$, and b) the CGL limit, as calculated by `MARS-K`, `MISK`, and `PENT`. The profiles shown are from *before* the Δq corrections are applied at the rational surfaces.

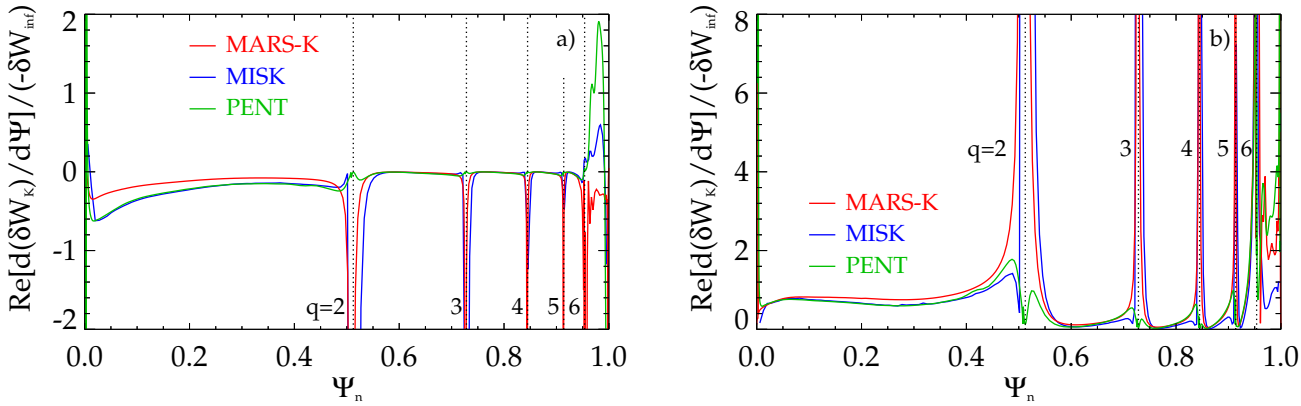

FIG. 66. $Re(d(\delta W_K/(-\delta W_\infty))/d\Psi)$ vs. Ψ for $l \neq 0$ trapped thermal ions in the ITER case at a) $\omega_{E0}/\omega_{A0} = 1.62 \times 10^{-2}$, and b) the CGL limit, as calculated by `MARS-K`, `MISK`, and `PENT`. The profiles shown are from *before* the Δq corrections are applied at the rational surfaces.

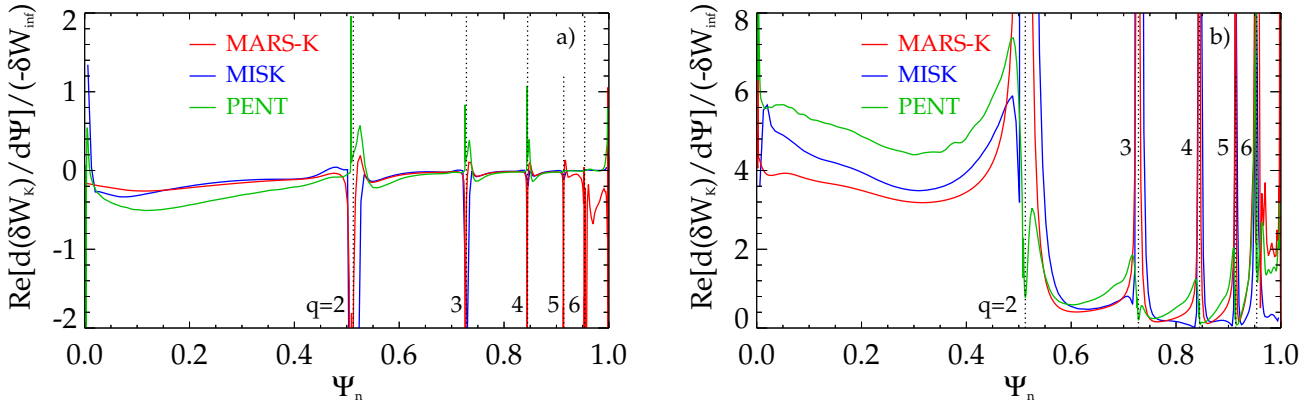

FIG. 67. $Re(d(\delta W_K/(-\delta W_\infty))/d\Psi)$ vs. Ψ for circulating thermal ions in the ITER case at a) $\omega_{E0}/\omega_{A0} = 1.62 \times 10^{-2}$, and b) the CGL limit, as calculated by `MARS-K`, `MISK`, and `PENT`. The profiles shown are from *before* the Δq corrections are applied at the rational surfaces.

X. GROWTH RATE AND MODE ROTATION FREQUENCY

In the dispersion relation (Eq. 1), the change in potential energy due to kinetic effects, δW_K, in general has both real and imaginary parts. The real part of ω is the mode rotation frequency, and is given by:

$$\omega_r \tau_w = - \frac{Im(\delta W_K)(\delta W_b - \delta W_\infty)}{(\delta W_b + Re(\delta W_K))^2 + (Im(\delta W_K))^2} \tag{56}$$

$$= - \frac{Im(\delta W_K/(-\delta W_\infty))(\gamma_f^{-1} + 1)}{(\gamma_f^{-1} + Re(\delta W_K/(-\delta W_\infty)))^2 + (Im(\delta W_K/(-\delta W_\infty)))^2}, \tag{57}$$

and solving for the imaginary part, we find the normalized growth rate:

$$\gamma \tau_w = - \frac{\delta W_\infty \delta W_b + (Im(\delta W_K))^2 + (Re(\delta W_K))(\delta W_\infty + \delta W_b + Re(\delta W_K))}{(\delta W_b + Re(\delta W_K))^2 + (Im(\delta W_K))^2} \tag{58}$$

$$= - \frac{-\gamma_f^{-1} + (Im(\delta W_K/(-\delta W_\infty)))^2 + (Re(\delta W_K/(-\delta W_\infty)))(\gamma_f^{-1} - 1 + Re(\delta W_K/(-\delta W_\infty)))}{(\gamma_f^{-1} + Re(\delta W_K/(-\delta W_\infty)))^2 + (Im(\delta W_K/(-\delta W_\infty)))^2}. \tag{59}$$

The results are given in Table VI and Figs. 68, 69, and 70. They are in generally good agreement. Note that in Fig. 68a and in Fig. 69a at lower rotation the MARS-K $\gamma\tau_w$ differs from MISK and PENT due to difference in the fluid, not kinetic, δW terms, as can be seen by the dashed lines. For the Solov'ev 1 case, over a large range of rotation the growth rate is not substantially changed from the fluid case. This is consistent with the previous analysis in Ref. [14], although, again, the cases are different because of the different eigenfunction used, as well as the different ω_E profile. The Solov'ev 3 case (Fig. 69) shows a larger influence of the kinetic effects. In particular, at high rotation the growth rate is reduced to different levels in each code's calculation due to the different levels of circulating and bounce resonant kinetic effects calculated. Intermediate plasma rotation is the least stable. The ITER case (Fig. 70) takes this trend even farther, as the kinetic resonances at high rotation with bounce and circulating particles is enough in each code to stabilize the plasma, while the precession resonance at low rotation is as well. The intermediate rotation between these resonances remains vulnerable to instability. One must recall that this is an incomplete calculation for ITER, however, as various simplifications have been made in the benchmarking process, including, most notably, the lack of collisions and energetic or alpha particles. Nevertheless, the codes agree in the basic underlying calculation of kinetic effects and all support the present understanding that both high and low rotation kinetic resonances are stabilizing to the RWM, but intermediate plasma rotation is potentially susceptible to instability.

	r_w/a	$\gamma\tau_w$	$\omega\tau_w$
Solov'ev 1	1.15	8.09×10^{-1}	1.82×10^{-2}
		8.58×10^{-1}	1.11×10^{-2}
		8.57×10^{-1}	1.86×10^{-2}
Solov'ev 3	1.10	4.73×10^{-1}	1.14×10^{-1}
		3.73×10^{-1}	5.07×10^{-2}
		3.84×10^{-1}	8.02×10^{-2}
ITER	1.50	8.19×10^{-1}	8.99×10^{-2}
		4.64×10^{-1}	4.51×10^{-1}
		4.89×10^{-1}	8.66×10^{-2}

TABLE VI. MARS-K results are red, MISK results are blue, PENT results are green. For the Solov'ev 1 and 2 cases the nominal value of $\omega_{e0}/\omega_{A0} = 1 \times 10^{-2}$ is used. For the ITER case, the nominal value of $\omega_{e0}/\omega_{A0} = 1.62 \times 10^{-2}$ is used, and surfaces within $\Delta q = \pm 0.1$ of all rational surfaces are excluded for MARS-K and MISK.

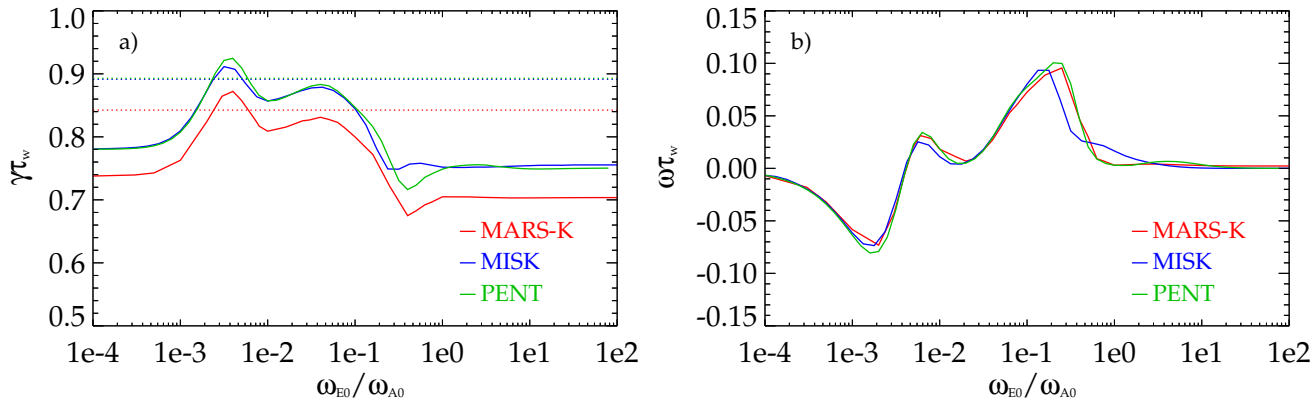

FIG. 68. a) $\gamma\tau_w$ (with $\gamma_f\tau_w$ shown in dashed lines) and b) $\omega\tau_w$ for the Solov'ev 1 case, as calculated by `MARS-K`, `MISK`, and `PENT`.

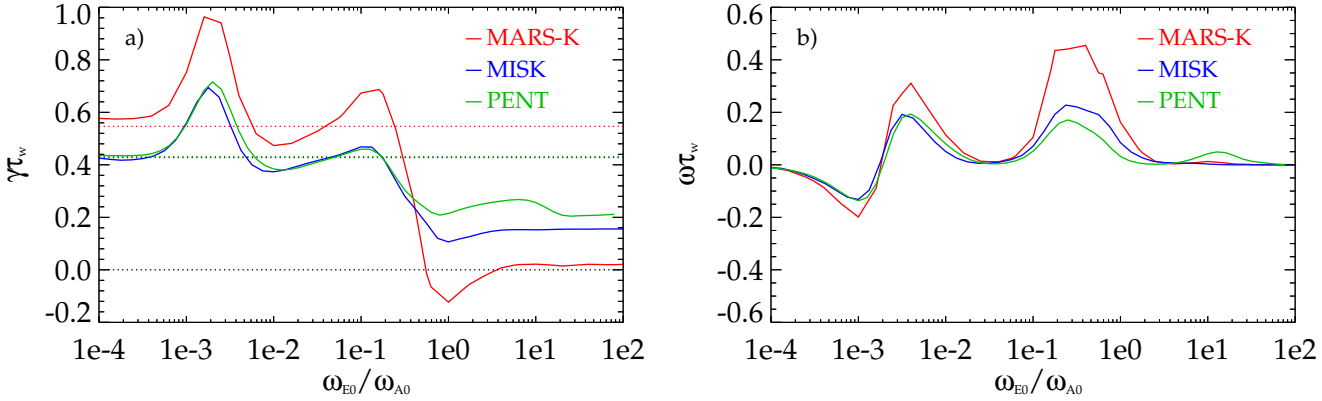

FIG. 69. a) $\gamma\tau_w$ (with $\gamma_f\tau_w$ shown in dashed lines) and b) $\omega\tau_w$ for the Solov'ev 3 case, as calculated by `MARS-K`, `MISK`, and `PENT`.

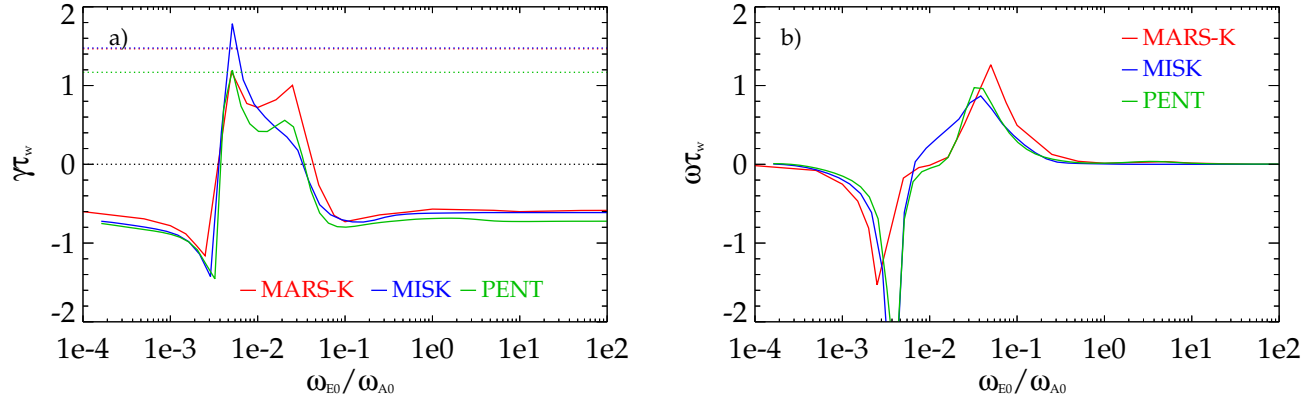

FIG. 70. a) $\gamma\tau_w$ (with $\gamma_f\tau_w$ shown in dashed lines) and b) $\omega\tau_w$ for the ITER case, as calculated by `MARS-K`, `MISK`, and `PENT`.

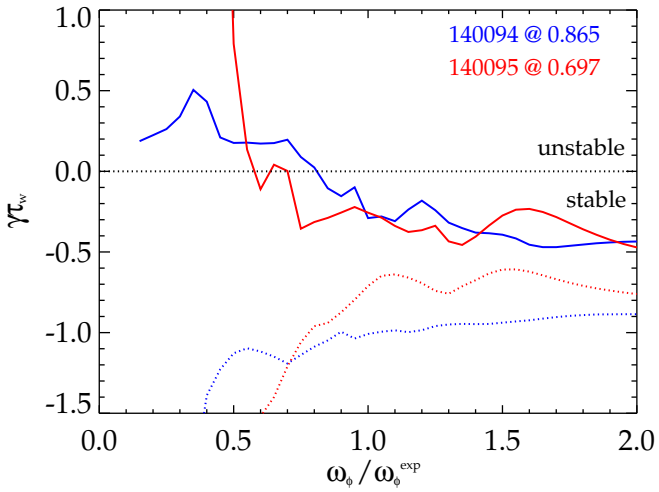

FIG. 71. $\gamma\tau_w$ vs. scaled experimental rotation profile as calculated by MISK for two NSTX equilibria near marginal RWM stability with the effect of the $n = 1$ rational surface singularities integrated numerically (dashed) or removed and replaced by an analytical calculation at the surfaces (solid).

XI. COMPARISON OF MISK CALCULATIONS TO NSTX EXPERIMENTS

NSTX experiments have demonstrated unstable RWMs and MISK calculations have been used to understand those experimental results[19–22,24,43,44]. Here we demonstrate that the benchmarked MISK calculations of thermal particle kinetic effects (now including collisions) can come close to predicting the marginal stability point. Figure 71 shows the calculated growth rate vs. scaled experimental rotation for two discharges from time points just before an unstable RWM caused a disruption (from Ref. [44]). In both cases MISK predicts that these discharges are close to marginal stability with the experimental rotation profile ($\omega_\phi/\omega_\phi^{\rm exp} = 1$), and that both will go unstable with a slightly lower rotation, which is what actually happens in the experiment since the rotation is decreasing in time in these discharges and there is some further decrease from the equilibrium time points analyzed to the unstable time. We also can demonstrate, by the dashed lines in Fig. 71, that by integrating over the rational surfaces, rather than performing the calculation analytically, the code predicts greater stability, which is inconsistent with the experimental evidence. Note that when the singularities are large enough and δW_K is larger than the fluid terms in Eq. 1, $\gamma\tau_w$ tends towards a highly stable value of unity.

XII. CONCLUSIONS

Calculations of the kinetic effects on resistive wall mode stability with the MARS-K, MISK, and PENT codes have been benchmarked. During the course of this process, changes and improvements have been made to each of the codes. The successful development of the PENT code was concurrent with, and highly dependent upon this process. An error in the precession frequency calculation was successfully corrected in the MISK code. This change has been tested and found to have a moderate impact on previously published results because the precession frequency is much less than the rotation frequency in NSTX. Finally, an error in computing a particle phase factor in the bounce resonance of thermal ions in the MARS-K code was found and corrected.

The benchmarking exercise considered three cases: two analytical Solov'ev equilibria and a projected ITER equilibrium. The various important frequencies of the problem, including bounce and precession drift freqencies, have been compared and show good agreement between the codes and also with analytical limits. These frequencies are used in the energy integral of the frequency resonance fraction, which forms the heart of the problem of kinetic effects on RWM stability. Analytical solutions of the energy integral are possible under certain constraints, and comparisons show that there is good agreement between the numerical and analytical approaches, as well as between the codes. The marginally stable ideal kink (fluid RWM) eigenfunctions, which are not affected by kinetic effects in the perturbative calculations performed here, are compared and show good agreement for the three equilibria. The terms in the perturbed Lagrangian using the eigenfunction, $\boldsymbol{\kappa}\cdot\boldsymbol{\xi}_\perp$ and $\boldsymbol{\nabla}\cdot\boldsymbol{\xi}_\perp$, also generally agree between the codes, although differences exist at the rational surfaces. Ideal stability calculations of the fluid δW terms and fluid growth rates of the mode are consistent.

Finally, the kinetic δW terms, growth rates, and mode rotation frequencies have been compared between the codes for the two analytical Solov'ev equilibria and the projected ITER equilibrium. Both MARS-K and MISK show convergence as damping is reduced to zero. The codes all show good agreement in the most important kinetic terms: the $l = 0$ precession drift resonant (at $\omega_E \ll \omega_A$) trapped thermal ions and electrons. For bounce-resonant trapped particles and circulating ions, with resonance for $\omega_E \gtrsim 0.1\omega_A$, the codes show some disagreement at the rational surfaces of the Solov'ev 3 case when the surfaces are integrated over. This is also reflected in a disagreement of the real part of δW_K as $\omega_E \to \infty$ in the CGL limit. In the ITER case, once the singularities at the rational surfaces have been removed all three codes show good agreement in δW_K.

The calculations shown here support the present understanding that RWM stability can be increased by kinetic effects at low rotation through precession drift resonance and at high rotation by bounce and transit resonances, while intermediate rotation can remain susceptible to instability. This can be most easily seen when the kinetic effects are used to calculate a growth rate and mode rotation frequency of the RWM. For example in Fig. 68a, for the Solov'ev 1 case, the growth rate is reduced at high and low ω_E. The results are in good agreement in this case, with the difference for $\gamma\tau_w$ coming mostly from the difference in the fluid growth rate (dashed lines). For the Solov'ev 3 case, the codes also show fairly good agreement in $\gamma\tau_w$ and $\omega\tau_w$, with the difference in $\gamma\tau_w$ at low ω_E again mostly due to the fluid growth rate, and the difference at high ω_E from the differences in the magnitude of the circulating and bounce resonances (Fig. 48), which comes from the rational surfaces. For MARS-K the rational surface contribution is large enough to provide marginal stability in this case. In the ITER case (Fig. 70) once the rational surface singularities are removed, the codes all agree quite well. The kinetic resonances at high rotation with bounce and circulating particles is enough in each code to stabilize the plasma, while the precession resonance at low rotation is as well. The intermediate rotation between these resonances remains vulnerable to instability.

Comparisons between the benchmarked calculations of the MISK code and experimental marginal stability points from NSTX demonstrate that the kinetic stability code calculations are useful for predicting the stability of experimental devices. Additionally, it is conclusively shown that the numerically computed inclusion of the effect of rational surface singularities can lead to an unrealistically large predicted kinetic stabilization effect and incorrect prediction of very stable plasmas.

The successful benchmarking between MARS-K, MISK, and PENT gives great confidence that these codes are correctly calculating the theoretically important expected kinetic effects of resistive wall mode stability. To the extent that this model is then validated against present experimental evidence of RWM stability, as has been done, for example, between MISK calculations and NSTX experiments, one can then project the stability of future devices with confidence. This is important because reliable, validated resistive wall mode stability calculations are critical for ITER, which can not tolerate disruptions.

ACKNOWLEDGMENTS

The authors would like to thank Allen Boozer, Jonathan Graves, Jeremy Hanson, Kimin Kim, Jon Menard, and Holger Reimerdes for many fruitful discussions.

This research was supported by the U.S. Department of Energy under contracts: DE-FG02-99ER54524 (Columbia University), DE-AC02-09CH11466 (Princeton Plasma Physics Laboratory), and DE-FG02-93ER54215 (University of Rochester). It was also supported in part by the Department of Energy Office of Science Graduate Fellowship Program (DOE SCGF), made possible in part by the American Recovery and Reinvestment Act of 2009, administered by ORISE-ORAU under Contract DE-AC05-06OR23100.

Additionally, this work was part-funded by the RCUK Energy Programme under grant EP/I501045 and the European Communities under the contract of Association between EURATOM and CCFE. To obtain further information on the data and models underlying this paper please contact PublicationsManager@ccfe.ac.uk. The views and opinions expressed herein do not necessarily reflect those of the European Commission.

[1] M. S. Chu and M. Okabayashi, Plasma Physics and Controlled Fusion **52**, 123001 (2010).
[2] E. Strait, T. Taylor, A. Turnbull, J. Ferron, L. Lao, B. Rice, O. Sauter, S. Thompson, and D. Wroblewski, Physical Review Letters **74**, 2483 (1995).
[3] S. A. Sabbagh, A. C. Sontag, J. M. Bialek, D. A. Gates, A. H. Glasser, J. E. Menard, W. Zhu, M. G. Bell, R. E. Bell, A. Bondeson, C. E. Bush, J. D. Callen, M. S. Chu, C. C. Hegna, S. M. Kaye, L. L. Lao, B. P. LeBlanc, Y. Q. Liu, R. Maingi, D. Mueller, K. C. Shaing, D. Stutman, K. Tritz, and C. Zhang, Nuclear Fusion **46**, 635 (2006).
[4] A. Bondeson and D. Ward, Physical Review Letters **72**, 2709 (1994).
[5] R. Betti and J. P. Freidberg, Physical Review Letters **74**, 2949 (1995).
[6] R. Fitzpatrick and A. Y. Aydemir, Nuclear Fusion **36**, 11 (1996).
[7] A. C. Sontag, S. A. Sabbagh, W. Zhu, J. E. Menard, R. E. Bell, J. M. Bialek, M. G. Bell, D. A. Gates, A. H. Glasser, B. P. LeBlanc, K. C. Shaing, D. Stutman, and K. Tritz, Nuclear Fusion **47**, 1005 (2007).
[8] H. Reimerdes, A. M. Garafalo, G. L. Jackson, M. Okabayashi, E. J. Strait, M. S. Chu, Y. In, R. J. La Haye, M. Lanctot, Y. Liu, G. Navratil, W. Solomon, H. Takahashi, and R. Groebner, Physical Review Letters **98**, 055001 (2007).

[9]H. Reimerdes, A. M. Garafalo, M. Okabayashi, E. J. Strait, R. Betti, M. S. Chu, B. Hu, Y. In, G. L. Jackson, R. La Haye, M. Lanctot, Y. Liu, G. Navratil, W. Solomon, H. Takahashi, R. Groebner, and the DIII-D team, Plasma Physics and Controlled Fusion **49**, B349 (2007).
[10]B. Hu and R. Betti, Physical Review Letters **93**, 105002 (2004).
[11]B. Hu, R. Betti, and J. Manickam, Physics of Plasmas **12**, 057301 (2005).
[12]B. Hu, R. Betti, and J. Manickam, Physics of Plasmas **13**, 112505 (2006).
[13]Y. Liu, M. S. Chu, C. G. Gimblett, and R. J. Hastie, Physics of Plasmas **15**, 092505 (2008).
[14]Y. Liu, M. S. Chu, I. T. Chapman, and T. C. Hender, Physics of Plasmas **15**, 112503 (2008).
[15]Y. Liu, M. S. Chu, I. T. Chapman, and T. C. Hender, Nuclear Fusion **49**, 035004 (2009).
[16]I. T. Chapman, V. G. Igochine, J. P. Graves, S. D. Pinches, A. Gude, I. Jenkins, M. Maraschek, and G. Tardini, Nuclear Fusion **49**, 035006 (2009).
[17]I. T. Chapman, C. G. Gimblett, M. P. Gryaznevich, T. C. Hender, D. F. Howell, Y. Q. Liu, and S. D. Pinches, Plasma Physics and Controlled Fusion **51**, 055015 (2009).
[18]Y. Liu, I. T. Chapman, M. S. Chu, H. Reimerdes, F. Villone, R. Albanese, G. Ambrosino, A. M. Garofalo, C. G. Gimblett, R. J. Hastie, T. C. Hender, G. L. Jackson, R. J. La Haye, M. Okabayashi, A. Pironti, A. Portone, G. Rubinacci, and E. J. Strait, Physics of Plasmas **16**, 056113 (2009).
[19]S. A. Sabbagh, J. W. Berkery, R. E. Bell, J. M. Bialek, S. P. Gerhardt, J. E. Menard, R. Betti, D. A. Gates, B. Hu, O. N. Katsuro-Hopkins, B. P. LeBlanc, F. M. Levinton, J. Manickam, K. Tritz, and H. Yuh, Nuclear Fusion **50**, 025020 (2010).
[20]J. W. Berkery, S. A. Sabbagh, R. Betti, B. Hu, R. E. Bell, S. P. Gerhardt, J. Manickam, and K. Tritz, Physical Review Letters **104**, 035003 (2010).
[21]J. W. Berkery, S. A. Sabbagh, H. Reimerdes, R. Betti, B. Hu, R. E. Bell, S. P. Gerhardt, J. Manickam, and M. Podesta, Physics of Plasmas **17**, 082504 (2010).
[22]J. W. Berkery, S. A. Sabbagh, R. Betti, R. E. Bell, S. P. Gerhardt, B. P. LeBlanc, and H. Yuh, Physical Review Letters **106**, 075004 (2011).
[23]Y. S. Park, S. A. Sabbagh, J. W. Berkery, J. M. Bialek, Y. M. Jeon, S. H. Hahn, N. Eidietis, T. E. Evans, S. W. Yoon, J. Ahn, J. Kim, H. L. Yang, K. I. You, Y. S. Bae, J. Chung, M. Kwon, Y. K. Oh, W. Kim, J. Y. Kim, S. G. Lee, H. K. Park, H. Reimerdes, J. Leuer, and M. Walker, Nuclear Fusion **51**, 053001 (2011).
[24]J. W. Berkery, R. Betti, and S. A. Sabbagh, Physics of Plasmas **18**, 072501 (2011).
[25]G. Z. Hao, Y. Q. Liu, A. K. Wang, H. B. Jiang, G. Lu, H. D. He, and X. M. Qiu, Physics of Plasmas **18**, 032513 (2011).
[26]H. Reimerdes, J. W. Berkery, M. J. Lanctot, A. M. Garofalo, J. M. Hanson, Y. In, M. Okabayashi, S. A. Sabbagh, and E. J. Strait, Physical Review Letters **106**, 215002 (2011).
[27]D. Yadykin, Y. Q. Liu, and R. Paccagnella, Plasma Physics and Controlled Nuclear Fusion **53**, 085024 (2011).
[28]I. T. Chapman, C. G. Gimblett, M. P. Gryaznevich, T. C. Hender, D. F. Howell, Y. Q. Liu, and S. D. Pinches, Plasma Physics and Controlled Fusion **53**, 065022 (2011).
[29]I. T. Chapman, W. A. Cooper, J. P. Graves, M. P. Gryaznevich, R. J. Hastie, T. C. Hender, D. F. Howell, M. D. Hua, G. T. A. Huysmans, D. L. Keeling, Y. Q. Liu, H. F. Meyer, C. A. Michael, S. D. Pinches, S. Saarelma, and S. Sabbagh, Nuclear Fusion **51**, 073040 (2011).
[30]G. Z. Hao, A. K. Wang, Y. Q. Liu, and X. M. Qiu, Physical Review Letters **107**, 015001 (2011).
[31]Z. R. Wang, S. C. Guo, and Y. Q. Liu, Physics of Plasmas **19**, 072518 (2012).
[32]I. T. Chapman, Y. Q. Liu, O. Asunta, J. P. Graves, T. Johnson, and M. Jucker, Physics of Plasmas **19**, 052502 (2012).
[33]J. W. Van Dam, M. N. Rosenbluth, and Y. C. Lee, Physics of Fluids **25**, 1349 (1982).
[34]T. Antonsen, "Theory of fusion plasmas," (Editrice Compositori, Bologna, 1987) Chap. Kinetic Energy Principles, pp. 161–183.
[35]I. B. Bernstein, E. A. Frieman, M. D. Kruskal, and R. M. Kulsrud, Proceedings of the Royal Society of London. Series A, Mathematical and Physical Sciences **244**, 17 (1958).
[36]T. Antonsen, B. Lane, and J. Ramos, Physics of Fluids **24**, 1465 (1981).
[37]T. Antonsen and Y. Lee, Physics of Fluids **25**, 132 (1982).
[38]J. W. Van Dam, Journal of the Korean Physical Society **31**, S93 (1997).
[39]S. Haney and J. Freidberg, Physics of Fluids B **1**, 1637 (1989).
[40]R. Grimm, J. Greene, and J. Johnson, "Methods in Computational Physics, Vol. 16," (Academic Press, New York, 1976) Chap. Computation of the Magnetohydrodynamic Spectrum in Axisymmetric Toroidal Confinement Systems, pp. 253–280.
[41]A. Glasser and M. Chance, Bulletin of the American Physical Society **42**, 1848 (1997).
[42]M. Ono, S. M. Kaye, Y. K. Peng, G. Barnes, W. Blanchard, M. D. Carter, J. Chrzanowski, L. Dudek, R. Ewig, D. Gates, R. E. Hatcher, T. Jarboe, S. C. Jardin, D. Johnson, R. Kaita, M. Kalish, C. E. Kessel, H. W. Kugel, R. Maingi, R. Majeski, J. Manickam, B. McCormack, J. Menard, D. Mueller, B. A. Nelson, B. E. Nelson, C. Neumeyer, G. Oliaro, F. Paoletti, R. Parsells, E. Perry, N. Pomphrey, S. Ramakrishnan, R. Raman, G. Rewoldt, J. Robinson, A. L. Roquemore, P. Ryan, S. Sabbagh, D. Swain, E. J. Synakowski, M. Viola, M. Williams, and J. R. Wilson, Nuclear Fusion **40**, 557 (2000).
[43]S. A. Sabbagh and The NSTX Team, Nuclear Fusion **53**, 104007 (2013).
[44]J. W. Berkery, S. A. Sabbagh, A. Balbaky, R. E. Bell, R. Betti, A. Diallo, S. P. Gerhardt, B. P. LeBlanc, J. Manickam, J. E. Menard, and M. Podesta, submitted to Physical Review Letters (2013).
[45]I. T. Chapman, S. E. Sharapov, G. T. A. Huysmans, and A. B. Mikhailovskii, Physics of Plasmas **13**, 062511 (2006).
[46]S. D. Pinches, L. C. Appel, J. Candy, S. E. Sharapov, H. L. Berk, D. Borba, B. N. Briezman, T. C. Hender, K. I. Hopcraft, G. T. A. Huysmans, and W. Kerner, Computer Physics Communications **111**, 133 (1998).
[47]Y. Liu, M. S. Chu, W. F. Guo, F. Villone, R. Albanese, G. Ambrosino, M. Baruzzo, T. Bolzonella, I. T. Chapman, A. M. Garofalo, C. G. Gimblett, R. J. Hastie, T. C. Hender, G. L. Jackson, R. J. La Haye, M. J. Lanctot, Y. In, G. Marchiori, M. Okabayashi, R. Paccagnella, M. Furno Palumbo, A. Pironti, H. Reimerdes, G. Rubinacci, A. Soppelsa, E. J. Strait, S. Ventre, and D. Yadykin, Plasma Physics and Controlled Fusion **52**, 104002 (2010).
[48]J. Park, A. Boozer, and A. Glasser, Physics of Plasmas **14**, 052110 (2007).
[49]N. C. Logan, J. K. Park, K. Kim, Z. Wang, and J. W. Berkery, Physics of Plasmas **20**, 122507 (2013).
[50]J. Park, Physics of Plasmas **18**, 110702 (2011).
[51]Z. R. Wang, J. K. Park, Y. Q. Liu, N. Logan, K. Kim, and J. E. Menard, submitted to Physics of Plasmas (2013).

[52]L. Solov'ev, Zh. Eksp. Teor. Fiz. **53**, 626 (1967).
[53]M. S. Chance, J. M. Greene, R. C. Grimm, J. L. Johnson, J. Manickam, W. Kerner, D. Berger, L. C. Bernard, R. Gruber, and F. Troyon, Journal of Computational Physics **28**, 1 (1978).
[54]Y. Liu, R. J. Hastie, and T. C. Hender, Physics of Plasmas **19**, 092510 (2012).
[55]F. Villone, Y. Liu, G. Rubinacci, and S. Ventre, Nuclear Fusion **50**, 125011 (2010).
[56]A. Bondeson and M. S. Chu, Physics of Plasmas **3**, 3013 (1996).
[57]J. Graves, "Private communication," (2011).
[58]M. Rosenbluth and M. L. Sloan, Physics of Fluids **14**, 1725 (1971).
[59]B. D. Fried and S. D. Conte, *The Plasma Dispersion Function; the Hilbert Transform of the Gaussian* (Academic Press, 1961).
[60]K. Miyamoto, *Plasma Physics for Controlled Fusion* (Science and Culture Publishing, 2012).
[61]S. Preische, J. Manickam, and J. Johnson, Computer Physics Communications **76**, 318 (1993).
[62]L. J. Zheng, M. Kotschenreuther, and M. S. Chu, Physical Review Letters **95**, 255003 (2005).
[63]M. Chance, Physics of Plasmas **4**, 2161 (1997).
[64]J. K. Park, *Ideal Perturbed Equilibria in Tokamaks*, Ph.D. thesis, Princeton University (2009).